

This item was submitted to [Loughborough's Research Repository](#) by the author.
Items in Figshare are protected by copyright, with all rights reserved, unless otherwise indicated.

Radiation-induced grain boundary segregation in dilute alloys

PLEASE CITE THE PUBLISHED VERSION

PUBLISHER

© S Song

LICENCE

CC BY-NC-ND 4.0

REPOSITORY RECORD

Song, Shenhua. 2012. "Radiation-induced Grain Boundary Segregation in Dilute Alloys". figshare.
<https://hdl.handle.net/2134/10475>.

This item was submitted to Loughborough University as a PhD thesis by the author and is made available in the Institutional Repository (<https://dspace.lboro.ac.uk/>) under the following Creative Commons Licence conditions.



For the full text of this licence, please go to:
<http://creativecommons.org/licenses/by-nc-nd/2.5/>

LOUGHBOROUGH
UNIVERSITY OF TECHNOLOGY
LIBRARY

AUTHOR/FILING TITLE

SONG, S.

ACCESSION/COPY NO.

040116983

VOL. NO.

CLASS MARK

27 JUN 1997 *Loan copy*

26 JUN 1998

~~26 JUN 1998~~

25 JUN 1999

0401169839



RADIATION-INDUCED GRAIN BOUNDARY SEGREGATION IN DILUTE ALLOYS

by

SHENHUA SONG, MSc

A Doctoral Thesis

Submitted in partial fulfilment of the requirements for the award of Doctor of
Philosophy
of the
Loughborough University of Technology

August 1995

Loughborough University of Technology Library	
Date	Jan .96
Class	
Acc. No.	040116983

- 9/309066x

Acknowledgements

The work described in this thesis could not have been carried out without the help of others, whose support I gratefully acknowledge.

Sincere thanks must go to my two supervisors, Professor R.G. Faulkner of the Loughborough University of Technology and Professor P.E.J. Flewitt of the Nuclear Electric Berkeley Technology Centre, for their help, advice and encouragement throughout the duration of this work.

For financial support I am indebted to the Nuclear Electric Berkeley Technology Centre, thus allowing me to study in the Loughborough University of Technology, to take part in the International Summer School on the Fundamentals of Radiation Damage in the USA and to visit the Paul Scherrer Institute (PSI) of Switzerland for the irradiation experiment.

At the Nuclear Electric Berkeley Technology Centre, in addition to recognising the help of the authority as a whole, are two other individuals to whom I owe particular thanks: Dr S. Fisher for general instruction guidance in the techniques for radioactive material handling and specimen preparation; and Mr R. Scowen for detailed instruction and guidance in the techniques for radioactive material handling and specimen preparation, and for tuition on the operation of the VG HB501 FEGSTEM.

Particular thanks must also go to Dr P. Marmy of the PSI for the help given in the irradiation experiment. Finally, I am grateful to Dr H. Jiang for comments concerning the theoretical and experimental results.

Abstract

Modelling of irradiation-induced segregation or thermal non-equilibrium segregation needs data on the impurity-point defect binding energy. These values are generally unavailable. In this work, an initial approach to determining impurity-interstitial binding energies in metals is established with some success on the basis of strain field arguments and the earlier work is slightly modified for more accurate calculations of oversized impurity-vacancy binding energies. The method is applied to predictions of various impurity-point defect binding energies in several transition metal matrices. With the aid of the predictions, some experimental results on radiation-induced segregation are reasonably satisfactorily interpreted.

A radiation-induced grain boundary segregation (RIS) model is established for dilute alloys based on the complex mechanism and combined with McLean's equilibrium segregation model. In the model, radiation-enhanced solute diffusion is taken into consideration. Theoretical predictions are made for segregation of phosphorus in the neutron-irradiated α -Fe matrix. There exists a segregation transition temperature below which combined radiation-induced non-equilibrium and radiation-enhanced equilibrium segregation is dominant, and above which thermal equilibrium segregation is dominant; peaks in the temperature dependence of segregation shift to lower temperatures with decreasing neutron dose rate and/or increasing neutron dose; the combined radiation-induced non-equilibrium and radiation-enhanced equilibrium peak segregation temperature and the thermal equilibrium peak segregation temperature are about 150 and 550 °C, respectively, for phosphorus grain boundary segregation in the α -Fe matrix at neutron dose rate = 10^{-6} dpa/s and neutron dose = 1 dpa .

Grain boundary segregation of solutes in the neutron-irradiated and unirradiated (thermally aged) 2.25Cr1Mo steels doped with P and Sn is examined by means of field emission gun scanning transmission electron microscopy (FEGSTEM) which has very high spatial resolution (~ 1 nm). The material is irradiated to a dose of 0.042 dpa at a dose rate of 1.05×10^{-8} dpa/s in a swimming pool-type light-water research reactor in the Paul Scherrer Institute (PSI) of Switzerland. Grain boundary microanalysis is performed in the Nuclear Electric Berkeley Technology Centre of the UK. Comparison of the experimental and predicted results shows that the predictions are generally consistent with the observations.

Contents

Chapter One	Introduction	1
Chapter Two	Existing Segregation Theories	5
2.1	Equilibrium segregation	5
2.1.1	Equilibrium segregation thermodynamics	5
2.1.1.1	McLean`s thermodynamic theory	5
2.1.1.2	Equilibrium segregation in a ternary solution	6
2.1.1.3	Maximum segregation level	6
2.1.2	Equilibrium segregation kinetics	7
2.2	Non-equilibrium segregation	8
2.2.1	Thermal non-equilibrium segregation	8
2.2.1.1	Faulkner`s non-equilibrium segregation model	9
2.2.1.2	Doig and Flewitt`s non-equilibrium segregation model	11
2.2.1.3	Xu and Song`s non-equilibrium segregation model	12
2.2.2	Radiation-induced segregation	15
2.2.2.1	Segregation mechanisms	15
2.2.2.1.1	Inverse Kirkendall effects	15
2.2.2.1.2	Solute-defect complexes	17
2.2.2.2	Modelling	17
2.2.2.2.1	Rate theory model	18
2.2.2.2.2	Analytical approach	19
Appendix 2.1	Figures for Chapter Two	23
Chapter Three	Previous Experimental Studies on Radiation-Induced Segregation	33
3.1	Experimental techniques	33
3.2	Experimental results	35
3.2.1	Segregation in austenitic alloys	36
3.2.2	Segregation in ferritic alloys	38
Appendix 3.1	Figures for Chapter Three	40
Chapter Four	Effects of Radiation-Induced Segregation on Properties of Alloys	48
4.1	Effect on phase stability	48
4.2	Effect on void swelling	48

4.3 Effect on ductility of ferritic steels	49
4.4 Effect on stress corrosion cracking of austenitic stainless steels	50
Appendix 4.1 Figures for Chapter Four	54
 Chapter Five Production of Point Defects and Their Interactions with Solutes	
5.1 Primary recoil spectra	57
5.2 Defect production	59
5.3 Displacement cascade characteristics	62
5.4 Point defect-solute interaction	63
5.4.1 Vacancy-solute complexes	63
5.4.2 Interstitial-solute complexes	64
5.4.2.1 Self-interstitial	65
5.4.2.2 Interstitial-solute interaction	66
5.4.2.3 Interstitial-solute complex migration	66
Appendix 5.1 Figures for Chapter Five	69
 Chapter Six Determination of Impurity-Point Defect Binding Energies in Alloys	
6.1 Impurity-vacancy binding energy	81
6.2 Impurity-interstitial binding energy	83
6.3 Results	85
6.4 Discussion	86
6.5 Summary	89
Appendix 6.1 Tables for Chapter Six	91
Appendix 6.2 Figures for Chapter Six	93
 Chapter Seven Modelling of Radiation-Induced Grain Boundary segregation	
7.1 Radiation-induced segregation (RIS)	104
7.2 Thermal equilibrium segregation	108
7.3 Results	110
7.4 Discussion	113
Appendix 7.1 Tables for Chapter Seven	118
Appendix 7.2 Figures for Chapter Seven	120
 Chapter Eight Experimental Studies	132

8.1 Experimental alloys	132
8.2 Specimen preparation	132
8.3 Irradiation	132
8.4 Thermal ageing	133
8.5 Thin foil preparation	133
8.6 Transmission electron microscopy	133
8.7 Microchemical analysis	133
8.7.1 VG HB501 FEGSTEM	134
8.7.2 Procedure	136
8.7.3 Specimen analysis considerations	137
8.7.3.1 Drift	137
8.7.3.2 Contamination	137
8.7.3.3 Specimen thickness	138
8.7.3.4 Boundary tilt	139
8.7.4 Spectrum quantification	139
8.7.5 Error estimation of the analysed results	140
8.8 Results and discussion	141
8.8.1 Microstructure	141
8.8.2 Measured results	141
8.8.3 Correction of the measured results	143
8.8.4 Comparison of the theoretical and experimental results	146
8.9 Summary	147
Appendix 8.1 Tables for Chapter Eight	149
Appendix 8.2 Figures for Chapter Eight	154
Appendix 8.3 Description of the Reactor SAPHIR	185
 Chapter Nine Conclusions	 191
9.1 Impurity-point defect binding energies	191
9.2 Modelling of radiation-induced grain boundary segregation	191
9.3 Experimental studies	192
 Chapter Ten Future Work	 194
10.1 Irradiation and testing	194
10.2 Electron microscopy	194
10.3 Grain and lath boundary segregation modelling during neutron irradiation	 195
10.4 Relation of IG fracture processes in ferritic steels to segregation	 195

10.5 Summary 195

References 197

Chapter One

Introduction

Over the past twenty years, a great deal of experimental [1-27] and theoretical [28-39] research has been directed to a basic understanding of radiation-induced segregation (RIS) in alloys. The segregation of impurities and alloying elements to or away from external surfaces, grain boundaries, dislocations and voids has become a common effect in a wide variety of alloys during irradiation with neutrons or charged particles. Since the alloy composition in the vicinity of internal sinks and external surfaces is changed, this radiation-induced segregation will affect a number of bulk and surface properties which are sensitive to the alloy composition, for example, mechanical properties, void swelling, phase stability and corrosion resistance. Therefore, a good understanding of radiation-induced segregation is of considerable importance to nuclear power stations.

Mechanisms for radiation-induced segregation now seem to be classified into either inverse Kirkendall effects or solute-defect complex effects [40]. As well known from Kirkendall experiments, when components of an alloy diffuse via vacancies at different rates, a composition gradient may induce a net flux of vacancies across a lattice plane even if the vacancy distribution is initially uniform. During irradiation, the inverse situation occurs near sinks where gradients in the vacancy and interstitial concentrations may cause a net flux of solute and solvent atoms across the lattice plane. In multicomponent systems, relative diffusion rates of various components determine their enrichment or depletion. For solutes which have strong interactions with point defects, for example, phosphorus and silicon in steels and nickel alloys [6,41], solute-point defect complexes play an important part in the segregation [40]. Usually, in this scenario the solutes are undersized and the complexes are solute-interstitial pairs. This is because (a) the migration of solute-vacancy complexes is much more difficult than that of solute-interstitial complexes [28,42]; (b) the interaction between the undersized solute and the interstitial is much stronger than that between it and the vacancy while there is no or very weak interaction between the oversized solute and the interstitial [6,41]. As a consequence, it is certain that for undersized solutes that have strong interactions with interstitials, such as phosphorus and silicon in steels and nickel alloys, the diffusion of solute-interstitial complexes should be dominant during radiation-induced segregation.

Radiation-induced segregation is generally a non-equilibrium process, because, in the absence of continued irradiation, the solute build-up may be eliminated by

annealing [43]. Such non-equilibrium processes rely on steady-state point defect fluxes established as a result of spatial variations in point defect concentration. these variations also arise during quenching (for the case of vacancies). In both cases above, regions adjacent to the sinks become depleted in point defects, compared with those remote from the sinks. Thus the point defect concentration gradient is created between the sink and the regions beyond it, and point defects, along or complexed with solute atoms, then diffuse down the concentration gradient towards the sink. For dilute alloys, the concept of the solute-point defect complex is useful in describing the radiation-induced segregation mechanism. The situation is more complicated as the solute concentration increases above ~2 at%, because the individual nature of the complex is lost.

Radiation-induced segregation theory has received detailed attentions from Johnson and Lam [28] and Lam et al. [31]. These researchers have qualitatively supported their theory model with observations of radiation-induced segregation to free surfaces in Al-Zn and Al-Be alloys as well as austenitic stainless steels, respectively. Johnson and Lam [28] employed geometrical arguments to obtain equations for the fluxes of solutes, vacancies and interstitials. Allnatt et al. [44], however, have shown that their results are not consistent with the kinetic theory of diffusion. A new model has recently been established by Murphy [36], which is based on the kinetic theory of diffusion for a dilute alloy [45].

Murphy [36] took into account isolated vacancies, interstitials, solute atoms, and solute-defect complexes which consist of a solute atom and a point defect, and attained equations for the fluxes of vacancies, interstitials and solute atoms across a plane by considering in detail the jumps of vacancies and interstitials in sites adjacent to solute atoms. Druce et al. [46] have applied Murphy's model to predictions of radiation-induced grain boundary of phosphorus in ferritic steels.

One disadvantage with these rate theory models for dilute alloys is a large number of different jump frequencies that require to be determined. In general, these are unknown parameters, although thermal diffusion studies may provide some information about the jump frequencies of vacancies in alloys. The only practical method of gaining detailed information on the jump frequencies, especially for interstitials is atomic simulation, but up to now little work has been done in this field.

Faulkner et al. [38] more recently developed a innovative model of radiation-induced grain boundary segregation for dilute alloys. This model circumvents the requirement of complicated mathematical procedures inherent in the rate theory analyses of radiation-induced segregation and originally predicts the maximum magnitude of segregation, based on a thermodynamic approach using the equilibrium concentrations of point defects expected at the grain boundary ratioed to the quasi-equilibrium concentrations expected in the grain interior. Diffusion of point defect-solute complexes takes place down the complex concentration gradient created around the grain boundary at rates determined by solving Fick's Second Law for the appropriate boundary conditions. However, in the model of Faulkner et al. the effective dose rate is not taken into account and moreover the isothermal kinetic relation seems to have some problems because although it may well predict the concentration profile around the grain boundary, the grain boundary concentration of segregants is always equal to the maximum segregation magnitude, which appears to require modifying.

For ferritic steels there is a well-known ductile-brittle transition. Above the ductile-brittle transition temperature (DBTT) the material fails in a ductile mode, and the fracture toughness, a measure of the energy required to cause fracture, is high; below the DBTT the material fails in a brittle mode, and the energy required to cause fracture is low. Irradiation of ferritic steels causes the DBTT to increase and also reduces the energy for fracture in the ductile region. This is a problem of current concern in light-water reactor pressure vessel (RPV) steels. Of most concern is the possibility with which the brittle behaviour with large DBTT shifts may be encountered in the temperature regime of normal reactor operation or of reactor shutdown.

Metallurgical research has led to substantial improvements in this area. The poor behaviour of some steels has been correlated with the level of alloying, especially of copper, phosphorus, and nickel [47-49]. It is clear [49] that embrittlement of reactor pressure vessel steels is classified into hardening embrittlement and non-hardening one. The hardening embrittlement results from the production of hardening centres, both precipitates and matrix defects. The precipitation of copper to provide effective dislocation pinning sites with resultant increase in hardness and shift in DBTT to higher temperatures plays a dominant part in the hardening embrittlement. The non-hardening embrittlement is generally associated with intergranular failure arising from grain boundary segregation of impurities such as P, S, As, Sn and Sb. However, during irradiation, grain boundary segregation of

phosphorus plays a dominant role in the non-hardening embrittlement. For the role of nickel in RPV steels containing copper it is now well established that irradiation-induced hardening embrittlement is due to irradiation-enhanced precipitation of copper due to the increased vacancy concentration. In high nickel variants, the nickel actually alloys with the copper causing a change in precipitation kinetics and thus a change in precipitate number density; also the nickel in the copper changes the modulus of the copper precipitate which thereby changes its strength by the modulus hardening reaction with dislocations. In either way the nickel can thus change radiation-induced embrittlement. In fact, the most recent studies show [50] that the nickel is concentrated in an outer shell on the copper precipitates - hence the nickel effect is even more complicated.

For the above reasons, radiation-induced grain boundary segregation in low-alloy steels was theoretically and experimentally studied in the present work. An innovative and simple model of radiation-induced grain boundary segregation was established for dilute alloys. In the model, the effective dose rate and the temperature dependence of dislocation density have been considered. In view of thermal equilibrium segregation during irradiation, especially during intermediate temperature irradiation, this radiation-induced segregation model has been combined with McLean's thermal equilibrium segregation model [51]. In the treatment of equilibrium segregation, radiation-enhanced solute diffusion was taken into consideration. The theoretical predictions have been made for segregation of phosphorus and silicon in α -Fe and compared with the observed results for 2.25Cr-1Mo steel by using field emission gun scanning transmission electron microscopy (FEG-STEM).

Modelling of radiation-induced segregation or thermal non-equilibrium segregation requires data on the impurity-point defect binding energy. Generally these values are not available. Faulkner and Chapman [52,53] have been in a good position to calculate these values for some transition metal matrices. It is only the case, however, for impurity-vacancy binding energies. We have developed, with some success, an initial approach to determining impurity-interstitial binding energies on the basis of strain field arguments. This approach was reported in detail and the earlier work of Faulkner and Chapman [52,53] was briefly summarised and slightly modified for the calculation of oversized impurity-vacancy binding energies. All important impurity-vacancy and impurity-interstitial binding energies were calculated for several transition metal matrices.

Chapter Two

Existing Segregation Theories

Segregation of impurity or solute atoms is a highly localised change in concentration attained during the redistribution of the species between the matrix and interfaces or free surfaces. Segregation of impurity or solute atoms to defect sinks such as grain boundaries and free surfaces may be classified into equilibrium segregation and non-equilibrium one. Non-equilibrium segregation may be subdivided into thermal non-equilibrium segregation and radiation-induced segregation. Existing segregation theories will be briefly described in this chapter.

2.1. Equilibrium segregation

2.1.1. Equilibrium segregation thermodynamics

2.1.1.1. McLean's thermodynamic theory

McLean and Northcott proposed in 1948 [54] that embrittlement was due to segregation of dilute elements to grain boundaries and the driving force was to be the difference in distortion energy caused by a solute atom in the grain interior and at the grain boundary. In other words, the solubility of impurities in the boundaries is higher than in the matrix. Thermodynamically, this is due to the lowering of grain-boundary energy by the impurity. Gibbs [55] explained that elements which lower the surface energy are enriched at the surface. The solubility, in both the interior and at the surface, is temperature-dependent. Prolonged annealing in the embrittlement temperature range gives rise to a diffusion-controlled migration of solute or impurity atoms to the grain boundaries until an equilibrium state is reached. The enrichment of impurities at the grain boundaries lowers the grain boundary cohesion, resulting in grain boundary failure. The model has been termed the equilibrium segregation model.

Statistical mechanics gives the following expression for the equilibrium grain boundary concentration (C_{be}^m) of a solute [51]:

$$C_{be}^m = \frac{C_g A_e \exp(Q/kT)}{1 + C_g A_e \exp(Q/kT)} \quad (2.1)$$

where C_g is the concentration of the solute in the matrix,

A_e is the vibrational entropy factor in the grain boundary region,

Q is the difference in distortion energy caused by a solute atom between

the matrix and the grain boundary, known as the segregation energy,
 k is Boltzmann constant, and
 T is the absolute temperature.

2.1.1.2 Equilibrium segregation in a ternary solution

The simultaneous segregation of impurities I (P, Sb, As, Sn, etc.) and alloying elements M (Ni, Mn, Cr, etc.) has been considered by Guttman [56]. The interaction between M and I atoms is evaluated from the enthalpy of formation of the intermetallic compounds (NiSb , Mn_2Sb , Cr_3P , etc.) and is inserted into an expression for the equilibrium concentration C_{gb} at the grain boundaries similar to that of McLean. The contribution from the chemical interaction leads to an additional term ΔG^{chem} in the exponent of Equation (2.1). The concentrations of the impurity and alloy components are denoted as C_{gb}^I and C_{gb}^M , respectively, and they are calculated as

$$\Delta G_i^{\text{chem}} = \alpha_{MI} C_{gb}^M \quad (2.2)$$

and

$$\Delta G_M^{\text{chem}} = \alpha_{MI} C_{gb}^I \quad (2.3)$$

where α_{MI} is an interaction coefficient, using data from studies of a 0.2C-2Mn steel doped with 0.12%Sb, Guttman obtained $\alpha_{MI} = 80.4$ KJ/mol. He has shown that for most of the alloys which are susceptible to temper embrittlement, the interaction between impurities and alloying elements is moderate (e.g. Ni_3P , $\alpha_{\text{NiP}} = 292.9$ KJ/mol). If the interaction is too strong, stable compounds will precipitate in the matrix (e.g. MnS , $\alpha_{\text{MnS}} = 410.1$ KJ/mol); if the interaction is too weak, there will be insufficient driving force for segregation. A slightly modified version of Guttman's equilibrium segregation theory for ternary systems can be seen in Ref. [57].

2.1.1.3. Maximum segregation level

Cahn and Hilliard [58] have derived an expression for the maximum excess amount of impurities $\Gamma_{2(1)}^\circ$ at the grain boundary. These authors started from Gibbs adsorption theorem at constant temperature and pressure

$$-d\sigma = \Gamma_1 du_1 + \Gamma_2 du_2 \quad (2.4)$$

and Gibbs-Duhem equation

$$X_1 d\mu_1 + X_2 d\mu_2 = 0 \quad (2.5)$$

where σ is the surface energy, Γ is the total excess amount of impurities per unit area, μ_1 and μ_2 are the chemical potential of components 1 and 2, respectively, and X_1 is X_2 are the atomic fraction of components 1 and 2, respectively. By differentiating Equations (2.4) and (2.5) with respect to X_2 and eliminating $d\mu_1 / dX$, one may obtain with $X_2 = (1 - X_1) = X$

$$-\frac{d\sigma}{dX} = \Gamma_{2(1)} \frac{d\mu_2}{dX} \quad (2.6)$$

where $\Gamma_{2(1)}$ is defined by

$$\Gamma_{2(1)} = \Gamma_2 - \frac{X}{1-X} \Gamma_1 \quad (2.7)$$

$\Gamma_{2(1)}$ may be estimated. The measured quantity at an atomic fraction of solute atoms X_o is denoted as $\Gamma_{2(1)}^o$. the upper limit of $\Gamma_{2(1)}^o$ is estimated to be

$$\Gamma_{2(1)}^o < \frac{\sigma_1}{kT[1 + \ln(\frac{X_o}{X_e})]} \quad (2.8)$$

where σ_1 is the surface energy of pure component 1 and X_e is the solubility limit of component 2 in solution 1.

For P in α -Fe, Cahn and Hilliard found that $\Gamma_{P(Fe)}^o = 0.19 \times 10^{16}$ atoms/cm², using $X_o = 0.002$, $X_e = 0.02$, $T = 1273$ K, and $\sigma_{Fe(\gamma)} = 850$ mJ/m² (σ for ferrite was not known). This value is roughly equivalent to a layer of 0.3 nm thickness of pure P at the boundary. The model gives no limitation to the concentration profile in the direction perpendicular to the grain boundary. Therefore, the atoms may be spread out in the neighbourhood of the boundary. The model appears to give results of the correct order of magnitude for the segregation of single element.

The upper limit in Equation (2.8) is calculated for the case that the surface energy of the impure metal would approach zero. However, it has been reported [59-61] that the surface energy cannot decrease below 400 mJ/m². Cahn and Hilliard's model dose not take account of the interaction between impurities and alloying elements and thus is only suitable for binary solutions.

2.1.2. Equilibrium segregation kinetics

When a sample is so quickly cooled from a quenching temperature (or solution treatment temperature) T_i to a lower temperature T_j that no mass transfer occurs in the sample during cooling, and then held at the lower temperature T_j , the equilibrium segregation kinetics, $C_{be}(t)$, derived by means of Equation (2.1), is [51]

$$\frac{C_{be}(t) - C_{be}^m(T_i)}{C_{be}^m(T_j) - C_{be}^m(T_i)} = 1 - \exp\left(\frac{4D_i t}{\alpha_e^2 d_e^2}\right) \operatorname{erfc}\left(\frac{2\sqrt{D_i t}}{\alpha_e d_e}\right) \quad (2.9)$$

where $C_{be}(t)$ is the grain boundary concentration at time t at the lower temperature T_j ;

$C_{be}^m(T_i)$ is the equilibrium grain boundary concentration attained after infinite time at temperature T_i , determined by Equation (2.1);

$C_{be}^m(T_j)$ is the equilibrium grain boundary concentration attained after infinite time at temperature T_j , determined by Equation (2.1);

α_e is the ratio $C_{be}(T_j) / C_g$, where C_g is the concentration of solute atoms in the matrix;

D_i is the diffusion coefficient of solute atoms in the matrix at temperature T_j ;

t is the time; and

d_e is the thickness of the grain boundary.

2.2. Non-equilibrium segregation

2.2.1. Thermal non-equilibrium segregation

The non-equilibrium segregation mechanism was established by Aust et al. [62] and Anthony [63]. The mechanism of non-equilibrium segregation relies on the formation of sufficient quantities of vacancy-impurity complexes. Impurities, vacancies, and their recombined complexes are in equilibrium with each other at a given temperature. When material properly maintained at a solution-treatment (or quenching) temperature is quickly cooled to a lower temperature, it will exhibit a loss of vacancies along grain boundaries, i.e. at point-defect sinks, whereby it attains the equilibrium vacancy concentration at the lower temperature. The decrease in the vacancy concentration gives rise to a decrease in the complex concentration near the grain boundary. Meanwhile, in regions beyond the grain boundary, where no other defect sinks are present, the concentrations of the vacancy and the complex are generally invariant. Consequently, a complex concentration gradient appears between the grain boundary and the grain interiors. The gradient of complex concentration drives the complexes to diffuse to the grain boundary from the grain interiors. This diffusion leads excess impurity atoms to

concentrate in the vicinity of grain boundaries and results in non-equilibrium grain boundary segregation. It is evident that the larger the supersaturation level of vacancies in the grain interiors is, the larger is the segregation level of impurities.

The experimental results on non-equilibrium grain boundary segregation have shown [64-66] that non-equilibrium segregation can be classified into segregation and desegregation. When a sample is very quickly cooled from a high quenching temperature to a lower one and then held at the lower temperature, there exists a critical holding time for which the non-equilibrium segregation will be maximum. If the holding time of the sample is shorter than the critical time, the segregation of the complexes from the grain centres to the grain boundary will be dominant and the process is termed a segregation process; if the holding time is longer than the critical time, the process in which the diffusion of the impurity atoms from the boundary to the centres is dominant will also occur, termed a desegregation process.

2.2.1.1. Faulkner's non-equilibrium segregation model

Faulkner's model [67] originally predicted the maximum magnitude of non-equilibrium segregation in a sample quickly cooled to room temperature from a high quenching temperature, based on a thermodynamic argument using the equilibrium concentrations expected at the grain boundaries ratioed to the quasi-equilibrium concentrations expected within the grains. Diffusion of vacancy-impurity complexes takes place down the concentration gradient created around the grain boundaries at rates determined by solving Fick's Second Law for the appropriate boundary conditions. The maximum concentration of non-equilibrium grain boundary segregation in a dilute solution during cooling from quenching temperature T_0 to room temperature, C_{bn}^m , is given by

$$C_{bn}^m = C_s \left(\frac{E_b^{iv}}{E_f^v} \right) \exp \left(\frac{E_b^{iv} - E_f^v}{kT_0} - \frac{E_b^{iv} - E_f^v}{kT_{0.5T_m}} \right) \quad (2.10)$$

where E_b^{iv} is the vacancy-impurity binding energy, i.e. the sum of the vacancy and impurity formation energies minus the formation energy of the vacancy-impurity complex;

E_f^v is the vacancy formation energy;

$T_{0.5T_m}$ is the temperature at which sufficient diffusion to allow the non-equilibrium segregation process to occur becomes insignificant and it is usually taken as half of the absolute melting point of the matrix; and

C_g is the concentration of impurity atoms in the matrix.

The concentration (C_x) of impurity atoms at a given distance x , from the boundary after an effective time t_θ , is given by

$$\frac{C_x - C_g}{C_{bn}^m - C_g} = \text{erfc}\left[\frac{x}{2\sqrt{D_c t_\theta}}\right] \quad (2.11)$$

where D_c is the diffusion coefficient for impurity-vacancy complexes in the matrix. The lack of experimental data for this parameter is overcome using a theoretically analytical method described in Ref. [53]. The magnitude and extent of segregation predicted by Equation (2.11) is illustrated in Fig. 2.1.

The effective time, i.e. the effective diffusion time during cooling may be calculated using information about the quenching rate, θ , and the starting temperature, T_o . The effective time at temperature T_o , t_θ is approximately given by

$$t_\theta = \frac{\beta k T_o^2}{\theta E_A} \quad (2.12)$$

where E_A is the activation energy for diffusion of vacancy-impurity complexes in the matrix;

k is Boltzmann's constant; and

β is a constant, determined by empirical means as 0.01.

To allow for ageing after cooling an additional time (t_A) has to be added to t_θ , given by

$$t_A = t_{Ao} \exp\left[\frac{-E_A(T_o - T_A)}{k T_o T_A}\right] \quad (2.13)$$

where T_A is the ageing temperature, and t_{Ao} is the ageing time.

Impurity atoms in the enriched zone created by the non-equilibrium segregation process are not in their relaxed states as the atoms on the boundaries during equilibrium segregation and thus they will diffuse back down their own concentration gradients. As mentioned above, this desegregation process in which the back diffusion of impurity atoms from the boundaries to the centres is dominant may be envisaged to begin after a critical time, t_c (see Fig. 2.2), given by [65-67]

$$t_c = \frac{\delta R^2 \ln(D_c/D_i)}{4(D_c - D_i)} \quad (2.14)$$

where δ is a numerical factor(quoted by Faulkner [67] as 0.05);

R is the grain size; and

D_c and D_i are the diffusion coefficients of complexes and impurity atoms in the matrix, respectively.

The desegregation equation, when time t is greater than t_c , is given by (see Fig. 2.3)

$$\frac{C_x - C_g}{C_{bn}^m - C_g} = \left(\frac{D_c t_c}{D_s t}\right)^{\frac{1}{2}} \exp\left(\frac{-x^2}{4D_s t}\right) \quad (2.15)$$

C_x obtained from Equations (2.11) and (2.15), depending on whether t is greater than or less than t_c , is then assigned the non-equilibrium segregation concentration, $C_{x(NES)}$.

2.2.1.2 Doig and Flewitt's non-equilibrium segregation model

In 1981, Doig and flewitt [68] established a non-equilibrium grain boundary segregation model. The model states that vacancies created during cooling from a higher temperature result in segregation of solute atoms due to coupled vacancy-solute pair migration. For this non-equilibrium segregation, solute atoms are driven thermodynamically by the decrease in free energy associated with the annihilation of excess vacancies at grain boundaries. As a result, the local vacancy-solute pairing reaction may be considered to be balanced. This is a reasonable assumption because the pairing reaction depends on short range diffusion in small volume elements and may, therefore, be thought to be instantaneous as compared with long range diffusion necessary to set up overall solute equilibrium. For a system containing vacancy-solute pairs (complexes) with a concentration C_c , in equilibrium with solute atoms with a concentration C_i and vacancies with a concentration C_v , The reaction is given by



such that

$$C_c \rightleftharpoons (C_v - C_c) + (C_i - C_c) \quad (2.16)$$

The mass action relationship for the reaction is

$$[C_c]/([C_v - C_c][C_i - C_c]) = K \quad (2.17)$$

where the mass action constant, K , is given by

$$K = Z \exp(E_b^{iv}/kT) \quad (2.18)$$

where E_b^{iv} is the vacancy-solute binding energy;

Z is the coordination number;

T is the absolute temperature; and

k is Boltzmann's constant.

Statistically the probability of a vacancy-solute interaction increases with decreasing temperature whereas the equilibrium vacancy concentration decreases. If C_i is much greater than C_c , then Equation (2.17) changes to

$$C_c = KC_i C_v / (1 + KC_i) \quad (2.19)$$

At high temperatures there is a low probability of a vacancy coupling with a solute atom which is equivalent to a short life-time for a vacancy-solute pair. As the temperature decreases the probability of coupling increases yet the reducing vacancy concentration with temperature lowers the overall value of C_c . The resultant gradient of vacancy-solute pairs leads to solute segregation to the boundary. More details about the model may be seen in Ref. [68].

2.2.1.3. Xu and Song's non-equilibrium segregation model

In 1989, Xu and Song [69] developed a new non-equilibrium grain boundary segregation model by slightly modifying the base model of Faulkner. This model states that when a sample is so quickly cooled to a lower temperature T , from a high quenching temperature T_0 that no mass transfer occurs during cooling and then maintained at the lower temperature, the maximum concentration of non-equilibrium grain boundary segregation induced during holding at this lower temperature, $C_{bn}^m(T)$, is given by

$$C_{bn}^m(T) = C_s \left(\frac{E_b^{iv}}{E_f^v} \right) \exp \left(\frac{E_b^{iv} - E_f^v}{kT_0} - \frac{E_b^{iv} - E_f^v}{kT} \right) \quad (2.20)$$

It is obvious that the maximum concentration, $C_{bn}^m(T)$ is only dependent on the difference between the quenching temperature T_0 and the lower temperature T , and is independent of the cooling rate from T_0 to T . Therefore, Equation (2.20) is an important quasi-thermodynamic relation describing the non-equilibrium segregation.

When a sample is so quickly cooled from a temperature T_i to a temperature T_j ($T_i > T_j$) that no mass transfer takes place in the sample during cooling and held at temperature T_j , the non-equilibrium grain-boundary segregation kinetics, $C_{bn}(t)$, derived by means of Equation (2.20), is given by

$$\frac{C_{bn}(t) - C_{bn}^m(T_i)}{C_{bn}^m(T_j) - C_{bn}^m(T_i)} = 1 - \exp\left(\frac{4D_c t}{\alpha_n^2 d_n^2}\right) \operatorname{erfc}\left(\frac{2\sqrt{D_c t}}{\alpha_n d_n}\right) \quad (2.21)$$

where D_c is the diffusion coefficient of complexes in the matrix;

t is the holding time at temperature T_j ;

d_n is the thickness of the concentrated layer of impurity atoms;

$C_{bn}^m(T_i)$ is the maximum segregation level at temperature T_i , i.e. the grain boundary concentration of segregants at the holding time $t = 0$ at temperature T_j ; and

α_n is the enrichment ratio, given by

$$\alpha_n = \frac{C_b^m(T_j)}{C_s}$$

and

$$\operatorname{erfc}\left(\frac{2\sqrt{D_c t}}{\alpha_n d_n}\right) = 1 - \frac{2}{\sqrt{\pi}} \int_0^{2\sqrt{D_c t}/\alpha_n d_n} \exp(-Y^2) dY$$

Equation (2.21) is an isothermal kinetic relationship of non-equilibrium segregation for the segregation process. It depicts the non-equilibrium segregation level of impurity atoms at the grain boundaries as a function of holding time t at temperature T_j , as the segregation process of the complexes to the grain boundaries is dominant (see Fig. 2.4). From Equation (2.21) one may predict the non-equilibrium segregation level of impurities in the sample quenched from a high temperature.

It should be noted that Equation (2.21) is much different from Equation (2.9) in nature although they have the same form. In Equation (2.9), the concentration and the diffusion coefficient both are concerned with the impurity atoms; In Equation (2.21), the concentration is associated with the impurity atoms but the diffusion coefficient is related to the complexes. Details on the diffusion analysis of the non-equilibrium segregation process may be found in Ref. [69].

Furthermore, Equation (2.21) seems to be more reasonable than Equation (2.11). This is because for Equation (2.11) the grain boundary concentration is always equal to the maximum segregation level C_{bn}^m and is independent of time, which seems to have some problems.

As mentioned above, a critical time t_c (see Fig. 2.2) exists at some temperature. At a certain temperature when the critical time is longer than the effective time of impurity diffusion corresponding to the cooling process, t_c , the process in which the segregation is dominant occurs alone whereas when t_c is shorter than t_c , the process in which desegregation is dominant also appears.

The process in which desegregation is dominant will take place as the effective time is longer than the critical time at temperature T_j . The desegregation process is illustrated in Fig. 2.5. In this case, the segregation level of impurity atoms at the grain boundaries, $C_{bn}(t)$, is given by

$$C_{bn}(t) = C_s + \frac{1}{2}[C_{bn}(t_c) - C_s][\operatorname{erf}\left(\frac{d/2}{[4D_s(t-t_c)]^{1/2}}\right) - \operatorname{erf}\left(\frac{-d/2}{[4D_s(t-t_c)]^{1/2}}\right)] \quad (2.22)$$

where t is the holding time at temperature T_j , $t_c = t_c(T_j)$ and D_s is the diffusion coefficient of impurity atoms in the matrix. Evidently, Equation (2.22) is only concerned with desegregation. Thus the condition $t > t_c$ is necessary for Equation (2.22).

A diffusion effective time is required for predictions of non-equilibrium grain boundary segregation during cooling. As discussed elsewhere [64,65], any continuously cooling curve for a sample may be approximately replaced by a corresponding stepped curve, each step of which is formed by horizontal and vertical segments so as to calculate an effective time t_e at a given temperature for

the cooling process (see Fig. 2.6). The effective time corresponding to a stepped cooling curve consisting of n steps at temperature T is given by

$$t_e = \sum_{i=1}^n t_i \exp\left(-\frac{E_A(T - T_i)}{kTT_i}\right) \quad (2.23)$$

where E_A is the activation energy for the diffusion of complexes in the matrix, t_i and T_i are the isothermal holding time and temperature at the i th step of the stepped curve, respectively. When the chosen steps are small enough, the effective time corresponding to the stepped curve at a certain temperature will accurately enough be equal to that corresponding to the continuously cooling curve at the same temperature. It may be expected that the effect of diffusion of impurities (or complexes) during cooling is the same as that during isothermal holding for the effective time corresponding to this cooling process at some temperature. This means that it is possible that the calculation of segregation levels of impurities, caused by the diffusion of complexes, may be changed to that during isothermal holding by means of the concept of the effective time.

2.2.2. Radiation-induced segregation

During the past twenty years, a lot of experimental [1-27] and theoretical [28-39] research has been focused on a basic understanding of radiation-induced segregation in alloys. Nowadays, the segregation of impurities and alloying elements towards or away from external surfaces, grain boundaries, dislocations, voids and other types of defect sinks has become a common effect in a wide variety of alloys under irradiation with neutrons or charged particles. Since the alloy composition near internal sinks as well as external surfaces is altered, this irradiation-induced segregation will influence a number of bulk and surface properties which are susceptible to alloy composition, for example, mechanism properties, void swelling, phase stability and corrosion resistance. As a consequence, a good understanding of irradiation-induced segregation is of significant importance not only to fission and fusion reactor technology but also to potential applications in the development of special materials. In this section, existing radiation-induced segregation theories will be briefly addressed.

2.2.2.1. Segregation mechanisms

Current theoretical models relate solute segregation in irradiated alloys to the formation of mobile defect-solute complexes and/or to inverse Kirkendall effects

resulting from differences in the diffusion rates of free solute and solvent atoms as migrating via a vacancy or interstitial mechanism.

2.2.2.1.1. Inverse Kirkendall effects

As well known from Kirkendall type experiments, when the components of an alloy diffuse via vacancies at different rates, a composition gradient can give rise to a net flux of vacancies across a lattice or "marker" plane even though the vacancy distribution is initially uniform. During irradiation, the inverse situation emerges near the sinks where gradients in the vacancy and interstitial concentrations can lead to a net flux of solute and solvent atoms across a "marker" plane in an initially homogeneous alloy. This inverse Kirkendall effect is illustrated in Fig. 2.7a for the case of a vacancy gradient in the vicinity of a sink in a binary alloy consisting of elements A and B. The vacancy gradient generates a vacancy flux, J_v , towards the sink that induces an atom flux ($J_A^v + J_B^v$) of equal magnitude in the opposite direction, where J_A^v and J_B^v are the fluxes of A and B atoms, respectively. Since J_A^v and J_B^v transport A and B atoms in quantities proportional to their local atomic fractions, C_A and C_B , and to their partial diffusion coefficients, D_A^v and D_B^v , it is easy to see that the alloy composition around the sink dose not change when $D_A^v = D_B^v$. However, if $D_A^v \neq D_B^v$, the flux, away from the sink, of the faster diffusing component will be greater, compared with that of the slower diffusing component. As a result, the inverse Kirkendall effect caused by a vacancy flux will always bring about depletion, at the sink, of the faster diffusing component.

An inverse Kirkendall effect can also be caused by an interstitial gradient. However, any difference in the partial diffusion coefficient of A and B atoms via an interstitial mechanism, i.e. $D_A^i \neq D_B^i$, will result in the preferential transport of the faster diffusing component to the sink because the interstitial flux and the associated atom fluxes, J_A^i and J_B^i , migrate in the same direction (see Fig. 2.7b). Consequently, depending on the relative magnitudes of the ratios D_A^v/D_B^v and D_A^i/D_B^i , the two inverse Kirkendall effects may aid or oppose each other in causing solute enrichment or depletion near the sinks.

For a concentrated binary alloy, Wiedersich et al. [32] obtained the following relation between the steady-state concentration gradient for component A and the vacancy concentration gradient:

$$\nabla C_A = \frac{D_I^B D_I^A}{\alpha(D_I^B D_A^{IRR} + D_I^A D_B^{IRR})} \left(\frac{D_A^v}{D_B^v} - \frac{D_A^i}{D_B^i} \right) \nabla C_v \quad (2.24)$$

where D_I^A and D_I^B are the partial diffusion coefficients of interstitials diffusing via A and B atoms, respectively;
 D_A^{IRR} and D_B^{IRR} are the total radiation-enhanced diffusion coefficients for A and B atoms, respectively; and
 α is a thermodynamic factor that deviates from unity for non-ideal solutions.

The two cases of interest predicted by Equation (2.24) are illustrated in Fig. 2.8. Depletion of component A takes place at the sink as $D_A^v/D_B^v > D_A^I/D_B^I$, i.e. when the preferential transport of A atoms via vacancies outweighs that via interstitials. Conversely, enrichment of A atoms at the sink occurs as $D_A^v/D_B^v < D_A^I/D_B^I$.

2.2.2.1.2. Solute-defect complexes

In addition to the inverse Kirkendall effects, solute segregation to the sinks can also occur if solute atoms interact with vacancies or self-interstitials to form mobile solute-defect complexes. The complexes are especially important for segregation in dilute alloys and have been extensively treated by Johnson and Lam [28-30]. If the complexes go through protracted random walks before thermal dissociation, they may be considered as distinct entities diffusing down their own concentration gradients. In initially homogeneous alloys, the complexes diffuse towards sinks, and hence tend to cause solute enrichment in the vicinity of sinks.

In general, the contribution of solute-defect complexes to segregation is determined by their binding and migration energies. This segregation mechanism is expected to be quite important for undersized solutes as both experimental and theoretical studies [70-72] demonstrate that undersized solutes trap interstitials much more strongly than do oversized solutes. In fcc crystals, mechanisms for the long range transport of undersized solutes in the form of $\langle 100 \rangle$ mixed dumbbells have been proposed by Johnson and Lam [28] and Dederichs et al. [72].

Since solute-defect interactions for the long range transport of undersized solutes are less effective at high temperatures, diffusion of solute-defect complexes can be dominant at low temperatures, while the inverse Kirkendall effects may be able to be dominant at high temperatures. In the absence of solute-interstitial interactions, solute enrichment at sinks may take place at low temperatures via solute-vacancy complexes, and solute depletion may occur at high temperatures via the vacancy-induced inverse Kirkendall effect. Calculations by Wiedersich et al. [73] for the case of dilute binary alloys show that for solute-vacancy binding energies above ~ 0.2 eV,

solute segregation to sinks is dominated by the diffusion of solute-vacancy complexes; for lower solute-vacancy binding energies, solute depletion at sinks only arises due to the inverse Kirkendall effect.

2.2.2.2. Modelling

Theoretical treatments for irradiation-induced segregation are generally based either on rate theory [28, 35-37] or more recently on a simplified analytical approach [38]. Early calculations were applied almost exclusively to fcc alloys, but the recent studies of Faulkner et al. [38,74] have covered ferritic steels. In this section, Models on irradiation-induced segregation for dilute alloys will only be addressed, and models for concentrated alloys will not be described but they may be seen in Refs. [32-35].

2.2.2.2.1. Rate theory model

Johnson and Lam [28] first developed a phenomenological model for segregation in dilute alloys with an fcc structure. They considered mobile solute-vacancy complexes as well as mobile and immobile solute-interstitial complexes. Recently a new model has been established by Murphy [36], which is based on the kinetic theory of diffusion for a dilute alloy [45]. Johnson and Lam [28] adopted geometrical arguments to attain equations for the fluxes of solute atoms, vacancies, and interstitials. Allnatt et al. [44] have shown that their results are not in agreement with the kinetic theory of diffusion.

Murphy [36] took account of isolated vacancies, which are composed of a vacancy on a site neighbouring a solute atom, and obtained equations for the fluxes of vacancies, interstitials and solute atoms across a plane by considering in detail the jumps of isolated vacancies and interstitials in sites adjacent to solute atoms. In Murphy's model, the fluxes of vacancies, interstitials and solute atoms are given by

$$J_v = -D_v \nabla n_v - D_{sv}^v n_s \nabla n_v - D_{vs}^v n_v \nabla n_s \quad (2.25)$$

$$J_i = -D_i \nabla n_i - D_{si}^i n_s \nabla n_i - D_{is}^i n_i \nabla n_s \quad (2.26)$$

$$J_s = -(D_{vs}^s n_v + D_{is}^s n_i + D_R^s) \nabla n_s - D_{sv}^s n_s \nabla n_v - D_{si}^s n_s \nabla n_i \quad (2.27)$$

where n_v , n_i and n_s denote the concentrations of free vacancies, interstitials and solute atoms, i.e. excluding those defects and solute atoms that are trapped in

solute-defect complexes (solute-interstitial complexes of types a and b are distinguished by the relative positions of the solute and interstitial. complexes of type a can migrate over long distances; complexes of type b cannot.); the coefficients D_{sv}^v , etc. are functions of the various jump frequencies for vacancies and interstitials; there is also an additional radiation-induced diffusion term $D_R^s \nabla n_s$ in Equation (2.23), which arises because the direct interaction of the solute atoms with the bombarding particles or knock-on atoms produces additional mixing of the solute and solvent atoms. The coefficient D_R^s is proportional to the displacement damage rate. It is important to realise that, in contrast to Johnson and Lam's model [28], the cross-coefficients in Equations (2.25-2.27) are not equal each other, i.e., $D_{sv}^v \neq -D_{sv}^s$, $D_{vs}^v \neq -D_{vs}^s$, $D_{si}^i \neq D_{si}^s$, and $D_{is}^i \neq D_{is}^s$. The details for the determination of various coefficients presented above may be seen in Refs. [36, 37]. It should be recognised that the rate theory model is based on the inverse Kirkendall effects.

One disadvantage with these models for dilute alloys is a large number of different jump frequencies that need to be determined. Generally, these are unknown parameters, although thermal diffusion studies may supply some information about the jump frequencies of vacancies in alloys. The only practical method of obtaining detailed information on the jump frequencies, especially for interstitials, is atomistic simulation, but up to now little work has been done in this area.

2.2.2.2.2. Analytical approach

In 1993, Faulkner et al. [38] developed an innovative model of irradiation-induced grain boundary segregation for dilute alloys. This model originally predicted the maximum magnitude of segregation, based on a thermodynamic approach using the equilibrium concentrations of point defects expected at the grain boundary ratioed to the quasi-equilibrium concentrations expected in the grain interior. Diffusion of point defect-impurity complexes takes place down the complex concentration gradient created around the grain boundary by irradiation at rates by solving Fick's Second Law for the appropriate boundary conditions. The theoretical treatments of the model are depicted as follows.

It is well known that for undersized solutes the solute-interstitial complexes are dominant in leading to solute segregation. Therefore, the solute-interstitial complexes are only taken into account in the model.

The concentration of solute-interstitial complexes, C_c , is given by

$$C_c = K_c C_i C_i \exp\left(\frac{E_b^{ii}}{kT}\right) \quad (2.28)$$

where C_i is the interstitial concentration;

C_i is the solute concentration;

k is Boltzmann constant;

E_b^{ii} is the solute-interstitial binding energy; and

T is the absolute temperature.

At the interface where segregation is occurring, the concentration of interstitials may be assumed to be in equilibrium. This gives the equilibrium interstitial concentration as

$$C_i = A \exp\left(\frac{-E_f^i}{kT}\right) \quad (2.29)$$

where E_f^i is the formation energy of interstitial and A is a constant.

Consequently, from Equations (2.28) and (2.29), the ratio C_c/C_i at the boundary is given by

$$\left(\frac{C_c}{C_i}\right)_b = K_c A \exp\left(\frac{E_b^{ii} - E_f^i}{kT}\right) \quad (2.30)$$

In the matrix, the steady-state concentration of interstitials enhanced by irradiation is given by

$$C_i = A \exp\left(\frac{-E_f^i}{kT}\right) + \frac{G}{D_i k_d^2} \quad (2.31)$$

where G is the defect production or dose rate;

D_i is the diffusion coefficient of interstitials in the matrix; and

k_d^2 is the grain interior sink strength for the interstitial.

For simplicity it is supposed that only one type of sink exists inside the grain and that the sinks are dislocations and are uniformly distributed. In this case, k_d^2 is approximately given by

$$k_d^2 = \sqrt{Z_i \rho} \left(\frac{6}{R} + \sqrt{Z_i \rho} \right) \quad (2.32)$$

where ρ is the dislocation density;

Z_i is the bias parameter defining the preferential interaction between interstitials and dislocations, compared with that between vacancies and dislocations; and

R is the grain size.

From Equation (2.28) the value of C_c/C_i in the matrix is given by

$$\left(\frac{C_c}{C_i} \right)_s = K_c A \exp\left(\frac{E_b^{ii} - E_f^I}{kT}\right) + \frac{K_c G}{D_i k_d^2} \exp\left(\frac{E_b^{ii}}{kT}\right) \quad (2.33)$$

Dividing Equation (2.33) by Equation (2.30) gives

$$\frac{(C_c/C_i)_s}{(C_c/C_i)_b} = 1 + \frac{G}{AD_i k_d^2} \exp\left(\frac{E_f^I}{kT}\right) \quad (2.34)$$

The left-hand side of Equation (2.34) can be rearranged to give

$$\frac{(C_i/C_c)_b}{(C_i/C_c)_s} = 1 + \frac{G}{AD_i k_d^2} \exp\left(\frac{E_f^I}{kT}\right) \quad (2.35)$$

From previous work of Faulkner [67], the ratio of solute concentration at the grain boundary, C_b , to that in the matrix, C_s , predicted by Equation (2.35), has to be modified to account for the absolute concentration of the complexes, which is controlled by the binding energy, E_b^{ii} . Thus

$$\frac{C_b}{C_s} = \frac{E_b^{ii}}{E_f^I} \cdot \frac{(C_i/C_c)_b}{(C_i/C_c)_s} \quad (2.36)$$

When $(C_c)_b = (C_c)_s$, the maximum grain boundary segregation level induced by irradiation, C_{br}^m may be attained. Thus

$$C_{br}^m = C_s \cdot \frac{E_b^{ii}}{E_f^I} \left[1 + \frac{G}{AD_i k_d^2} \exp\left(\frac{E_f^I}{kT}\right) \right] \quad (2.37)$$

It is obvious that the maximum concentration is only dependent on irradiation temperature and is independent of irradiation time. As a consequence, Equation (2.37) is an important quasi-thermodynamic relation depicting irradiation-induced grain boundary segregation.

The concentration of solute at a given distance, x , from the boundary at irradiation time = t , $C_{\text{sl}}(t, x)$ is given by

$$\frac{C_{\text{sl}}(t, x)}{C_{\text{s}}} = \frac{C_{\text{br}}^{\text{m}}}{C_{\text{s}}} + \left(1 - \frac{C_{\text{br}}^{\text{m}}}{C_{\text{s}}}\right) \text{erf}\left(\frac{x}{2\sqrt{D_{\text{c}}t}}\right) \quad (2.38)$$

where D_{c} is the diffusion coefficient of complexes in the matrix.

A further refinement to this model is involved by introducing the concept of a critical time t_{c} , at which the steady state is achieved. At this critical time the net supply of solute atoms from the grain centres becomes exhausted. After this time the reverse flow of solute atoms caused by the non-equilibrium segregation concentration gradients created by irradiation will be equal to the forward flow of the complexes. This process is illustrated in Fig. 2.9. The factors controlling the critical time are the diffusion coefficient of the complexes (D_{c}) and that of the isolated solute atoms (D_{i}), and the grain size (R). t_{c} may be determined by Equation (2.14). However it should be noted here that under these circumstances the diffusion coefficient of solute-vacancy complexes in Equation (2.14) should be replaced by the diffusion coefficient of solute-interstitial complexes.

It may be seen from this model that although the model may well predict the concentration profile around the grain boundary, the grain boundary concentration of segregants [i.e. $C_{\text{sl}}(t, x = 0)$] is always equal to the maximum segregation level C_{br}^{m} in the whole irradiation process, which appears to need modifying.

Appendix 2.1

Figures for Chapter Two

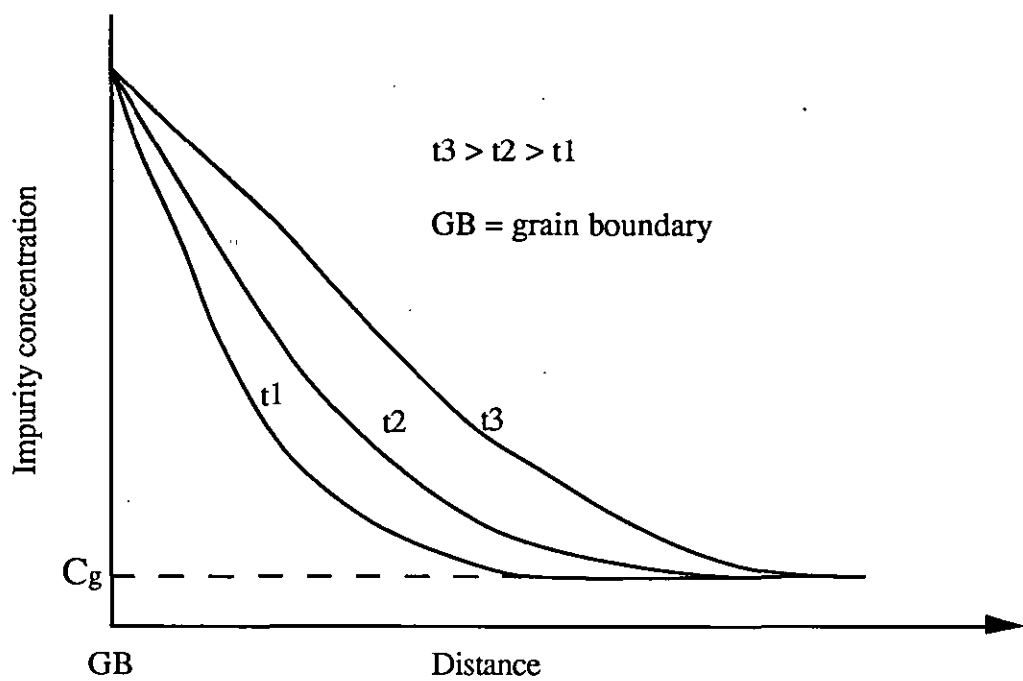


Fig. 2.1. Schematic diagram of the magnitude and extent of non-equilibrium segregation for the segregation process, predicted by Faulkner's model [67].

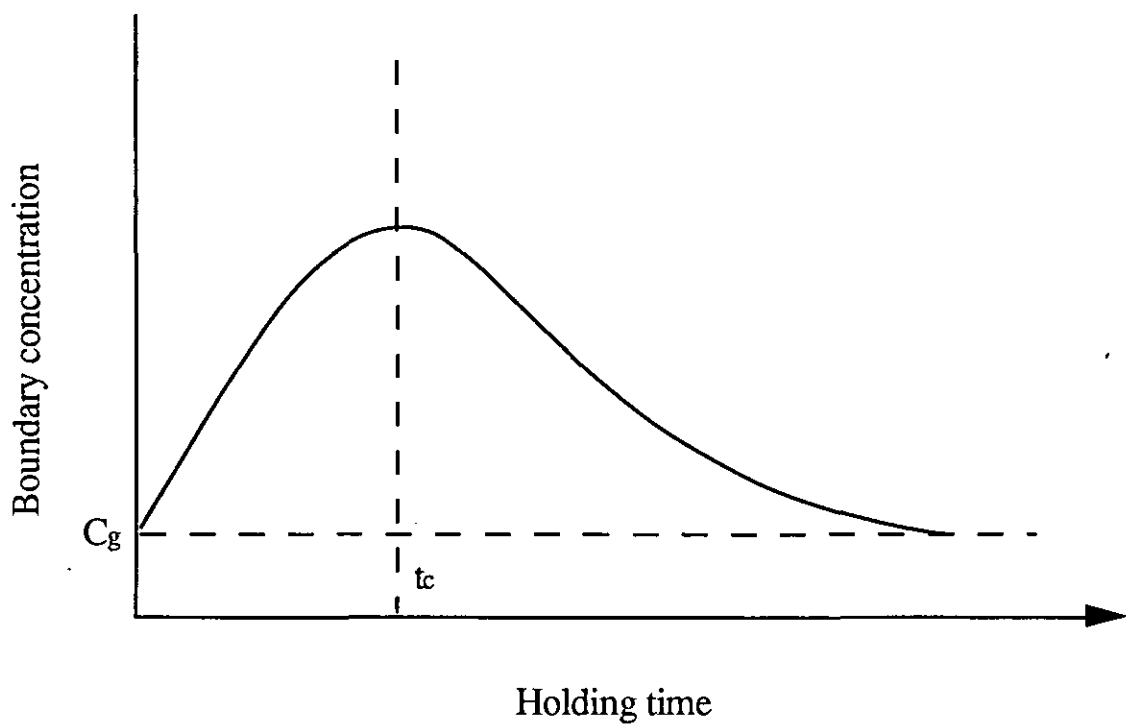


Fig. 2.2. Schematic diagram showing the segregation level as a function of holding time at a given temperature in the sample quenched from a high temperature.

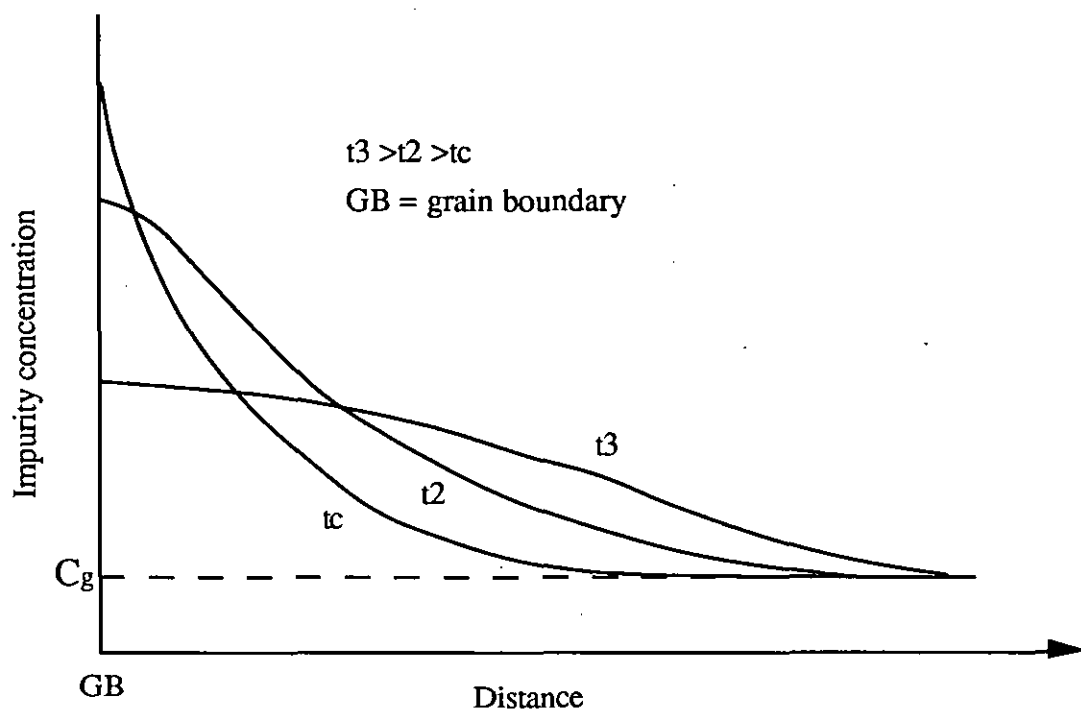


Fig. 2.3. Schematic diagram of the magnitude and extent of non-equilibrium segregation for the de-segregation process, predicted by Faulkner's model [67].

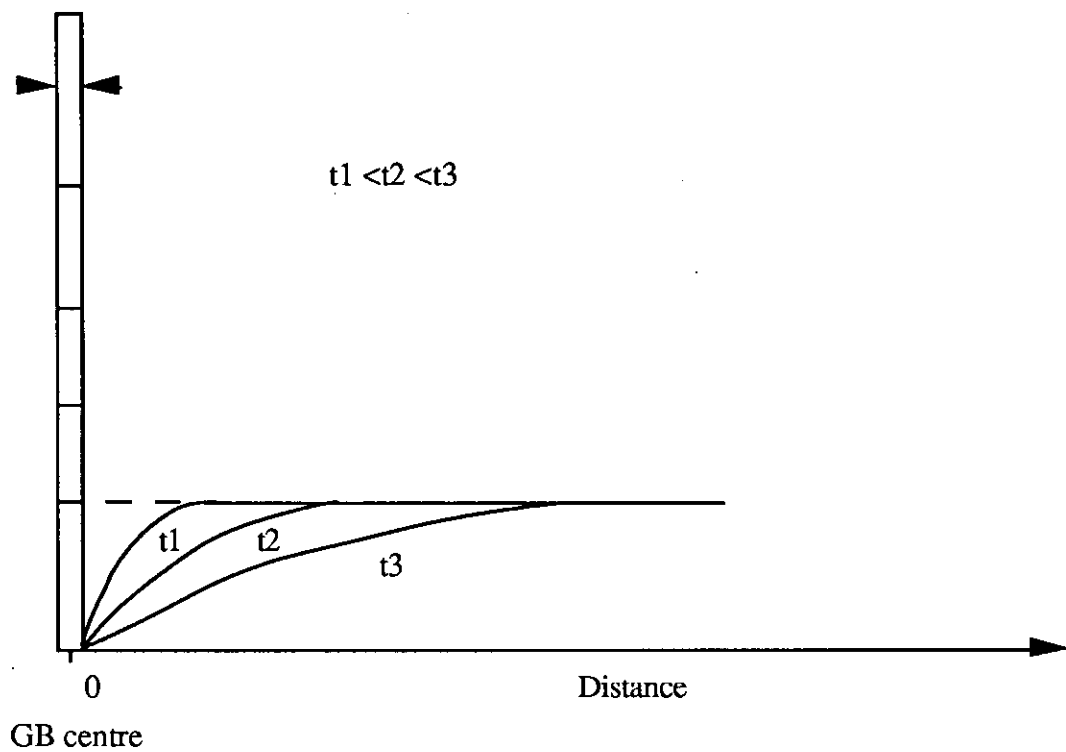


Fig. 2.4. Schematic diagram showing the segregation process of non-equilibrium grain boundary segregation, predicted by Xu and Song model [69].

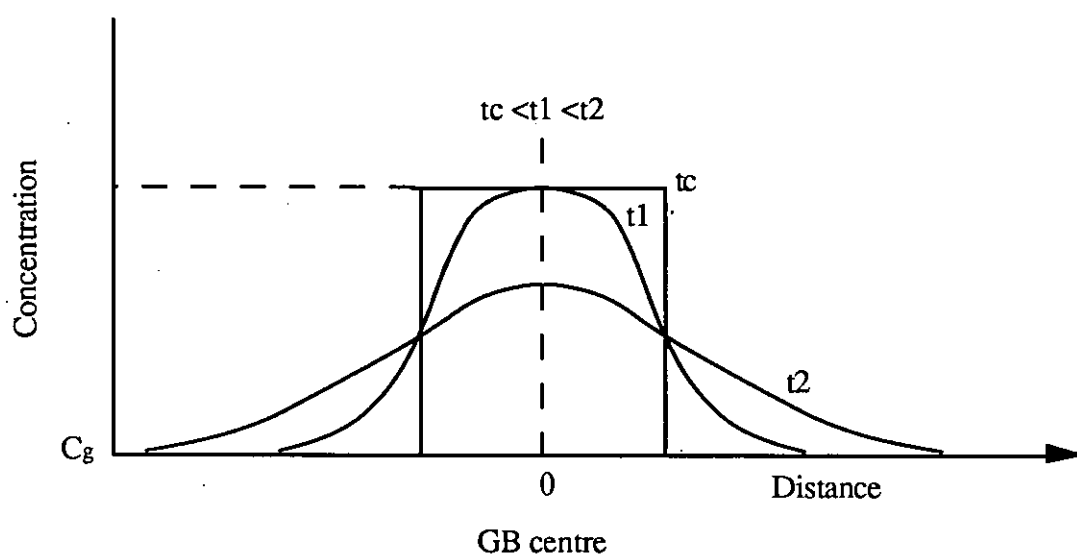


Fig. 2.5. Schematic diagram showing the desegregation process of non-equilibrium grain boundary, predicted by Xu and Song's model [69].

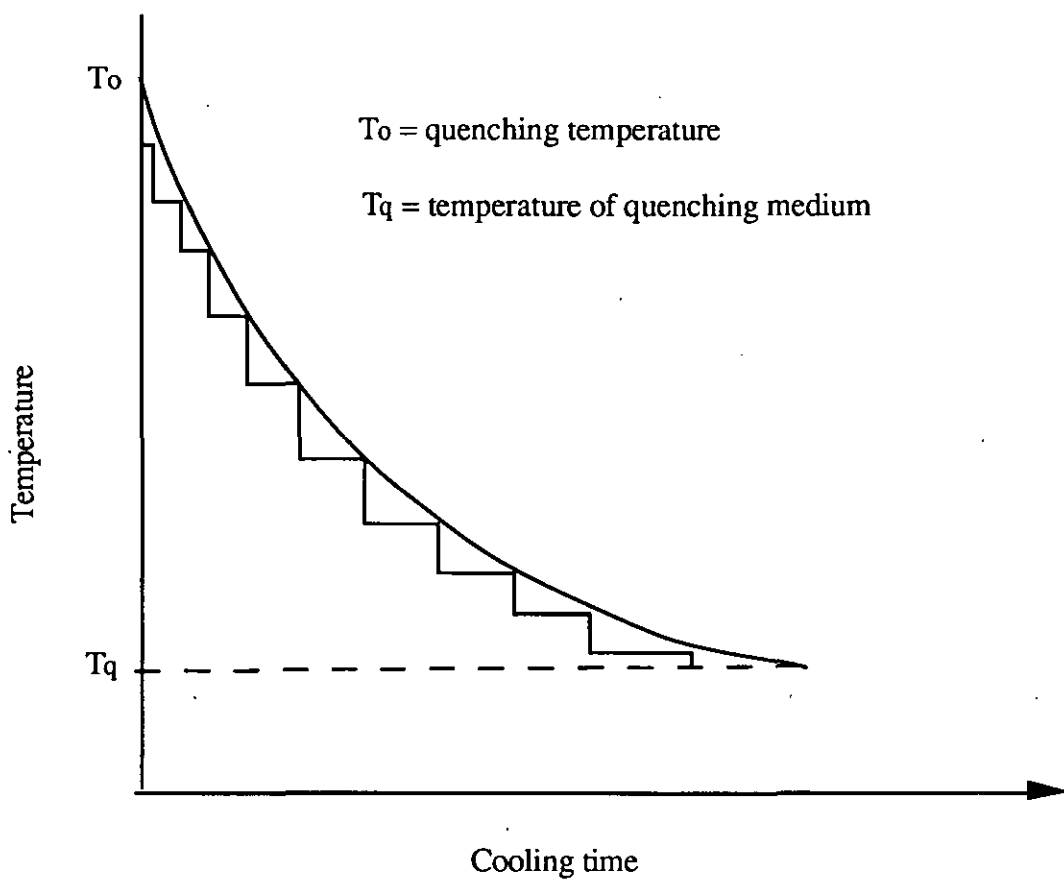


Fig. 2.6. The continuously cooling curve and the corresponding stepped curve.

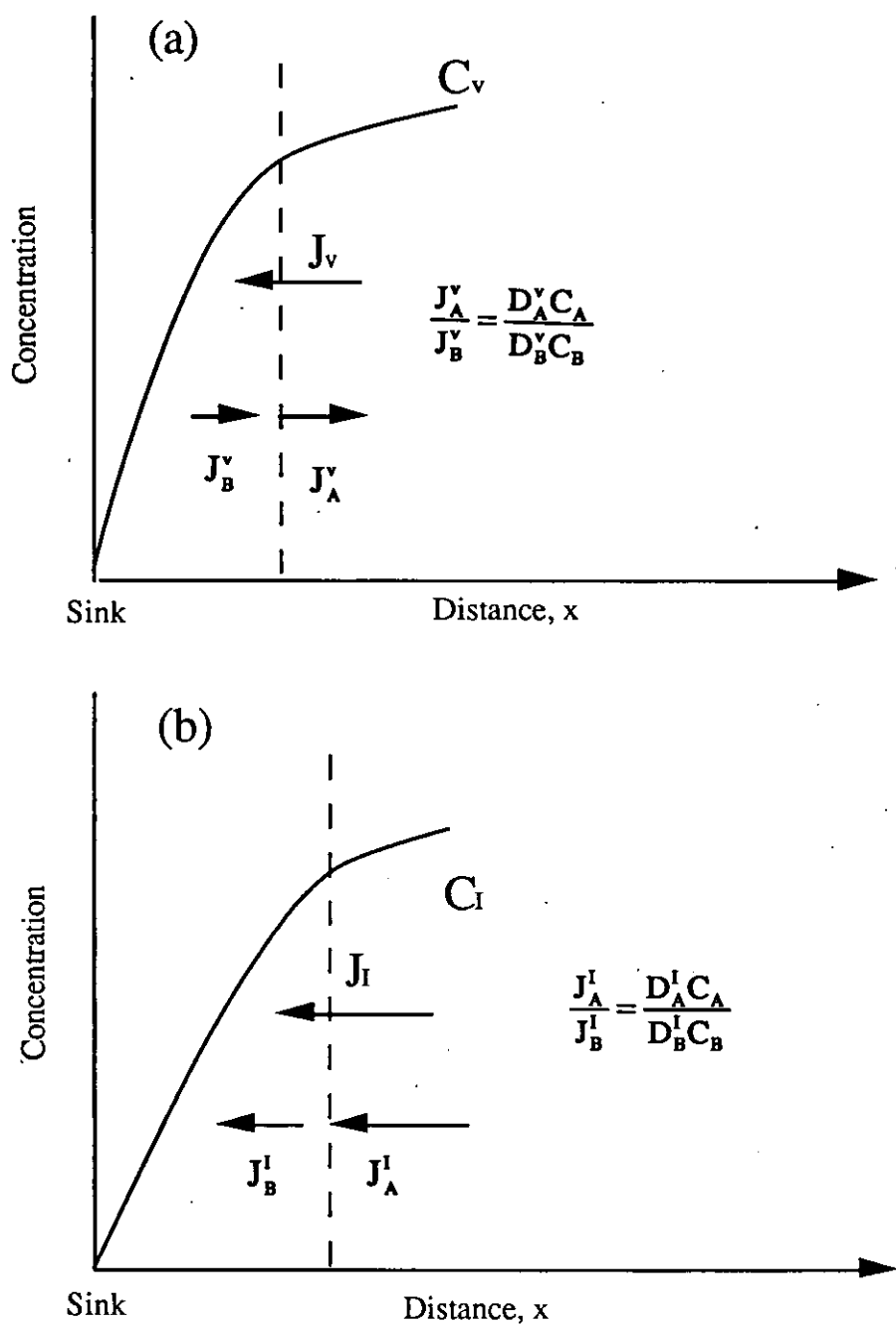


Fig. 2.7. Schematic illustration of inverse Kirkendall effects induced by (a) vacancy and (b) interstitial fluxes.

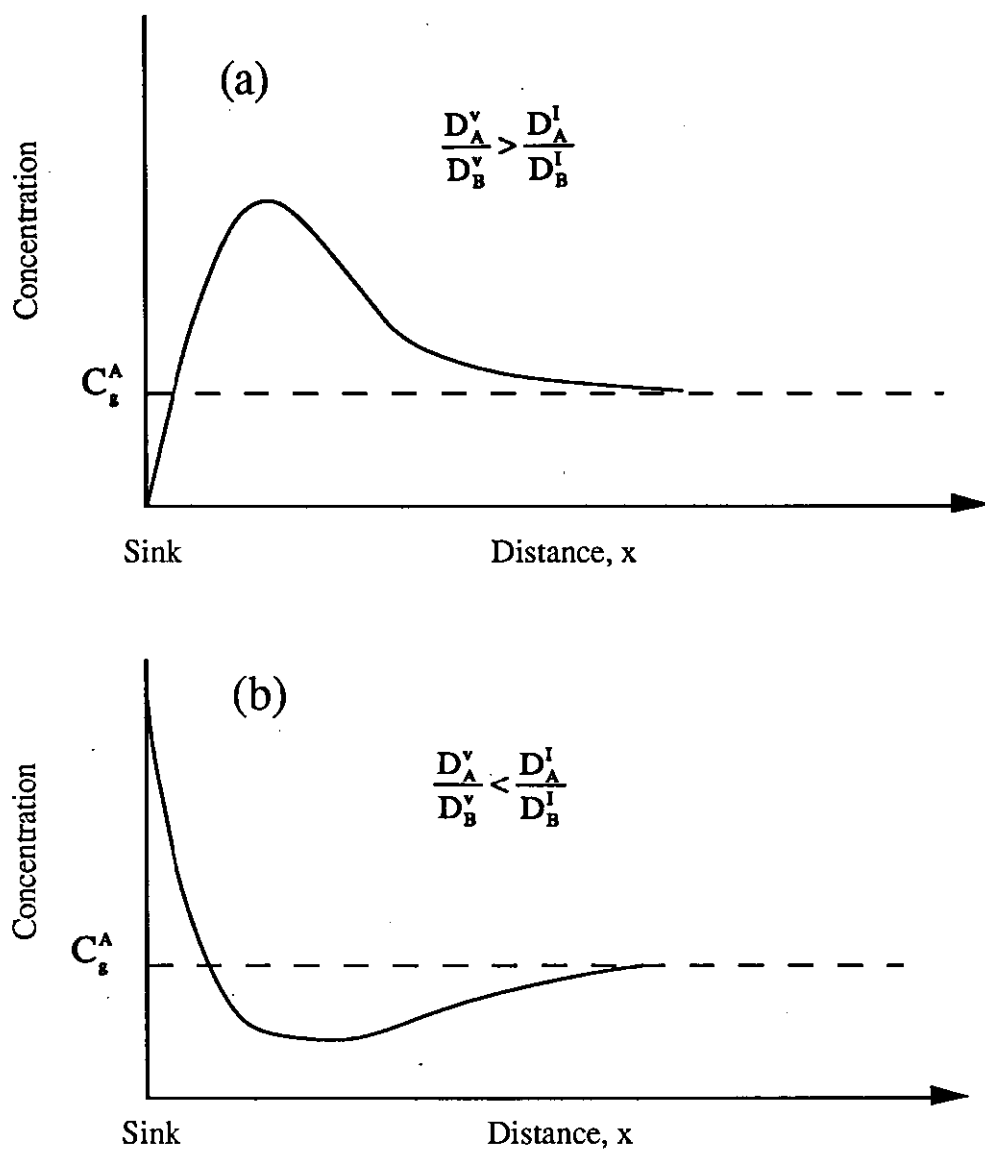


Fig. 2.8. Effects of partial diffusion coefficients on the depth distribution of A atoms.

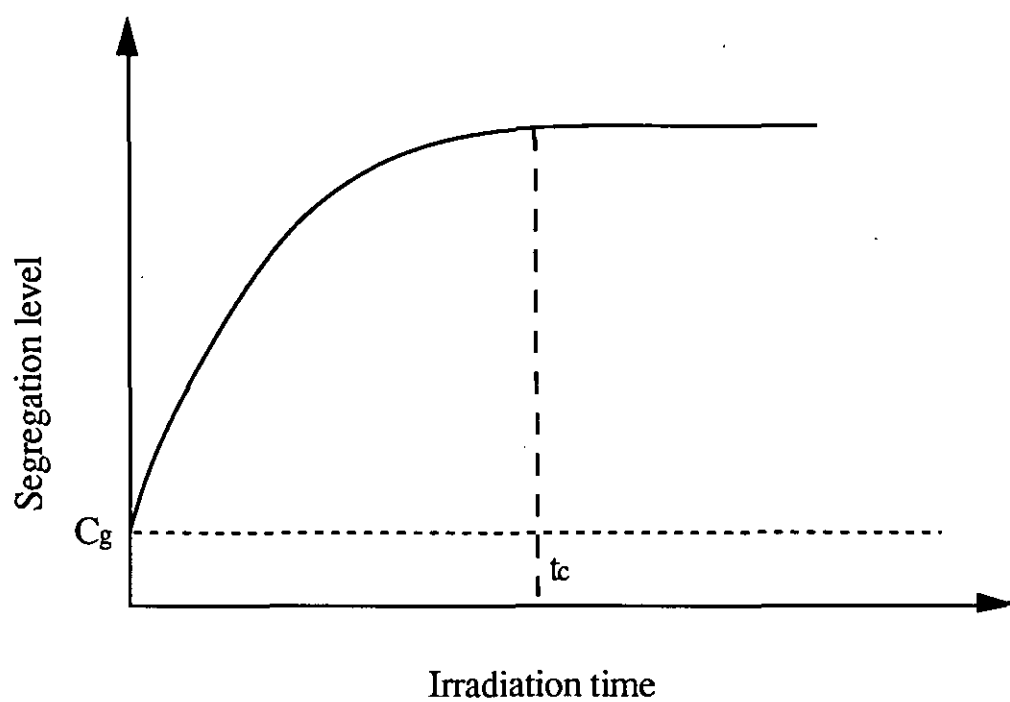


Fig. 2.9. Schematic diagram showing radiation-induced segregation level as a function of irradiation time at a given irradiation temperature. t_c is the critical time.

Chapter Three

Previous Experimental Studies on Radiation-Induced Segregation

A large amount of experimental research has been directed to an understanding of radiation-induced segregation. Much attention has been paid to austenitic alloys but not so much to ferritic alloys. In this chapter, the experimental techniques employed in the studies will be briefly addressed. Following this, some existing experimental results will be concisely presented.

3.1. Experimental techniques

The investigations of radiation-induced segregation requires (i) the creation of an irradiation environment in which concentration gradients of point defects are built up within the material; (ii) the application of an analytical technique that has sufficient precision to measure accurately the changes in local composition, induced by irradiation.

During irradiation with energetic particles such as neutrons, there exists essentially no spatial variation in the production rate of point defects. The fluxes of point defects are set up in the vicinity of point defect sinks such as grain boundaries, and it is the compositional profile near these sinks that needs determining.

Non-uniform, depth-dependent, concentrations of point defects can be created by irradiating specimens with heavy ions that have a short range (typically ~100 nm). In this case, the compositional changes in the region of point-defect production need to be measured. Since these changes are close to the surface because of the limited range of these ions, an analytical technique with good depth resolution is required. In general, first the solute is implanted into the sample at room temperature, and then the sample is irradiated at a higher temperature, and then the solute concentration profile is measured. The determination of irradiation-induced grain boundary segregation is more complicated because of the very small thickness of the grain boundary. consequently, an analytical technique with good transverse resolution is needed for the measurement of irradiation-induced grain boundary segregation in the case of not fracturing the sample along grain boundaries. The main analytical techniques are now briefly described as follows.

The local composition adjacent to grain boundaries grain boundaries can be determined by fracturing the sample and observing grain boundaries using Auger

electron spectroscopy (AES), analytical scanning transmission electron microscopy (STEM), analytical field emission gun scanning transmission electron microscopy (FEGSTEM) and others.

AES technique relies on the specimen failing along grain boundaries and it is possible that the selection process involved brings about a systematic error in the results. For example, it is possible that only the most highly segregated boundaries fail. Moreover, this technique has a low spatial resolution so that the misleading results may be acquired if small precipitates are present at the grain boundaries.

In STEM microanalysis, the grain boundary is oriented parallel to the incident beam. Spatial compositional profiles are produced by suitably positioning the incident electron beam to varying distances from the boundary plane and collecting the resultant X-ray spectra. Clearly the meaningful spatial resolution of the technique is determined by the electron-excited volume of material. This in turn, for a specific material, is dependent upon both the incident electron probe diameter and the degree of high angle elastic scattering of the beam through the foil thickness. For an infinitely thin foil the incident probe diameter places the limit on the attainable spatial resolution, which is progressively increased by the beam spreading effect with increasing foil thickness. Generally, in STEM the electron source is tungsten hairpin or LaB₆ filaments. The practical minimum probe sizes are usually 10-20 nm in diameter. Radiation-induced segregation is often on a scale less than this [75]. As a result, the spatial resolution of the above conventional STEM X-ray microanalysis is not high enough for compositional analysis of grain boundaries.

The analytical field emission gun scanning transmission electron microscopy (FEGSTEM) can offer much better spatial resolution. It is now possible to scan perpendicularly across the grain boundary to gain a concentration profile with a resolution of ~2 nm [76]. The electron beam may be positioned between precipitates to obtain accurate grain boundary concentrations of most atomic species. The main disadvantage of this technique is the small size of the regions which may be studied. This technique will be detailed in Section 7.3. A similar approach may also be employed to study segregation at grain boundaries in the sample irradiated with 1 MeV electrons arising in the high-voltage electron microscope (HVEM) [77-79].

As described above, when ion-beam techniques are adopted the segregation of an implanted solute is determined by observing the movement of the solute after

irradiation. This may be done by using a depth-profiling technique such as secondary ion mass spectrometry (SIMS) or AES. Because ion-beam techniques allow experiments to be done relatively easily and quickly, in well controlled conditions this type of experiment is well suitable for studying the mechanisms of irradiation-induced solute segregation in model alloys. Researchers at Argonne have used these techniques to investigate the mechanisms of irradiation-induced segregation [43,80]. As also depicted above, FEGSTEM is a good analytical technique for studying irradiation-induced grain boundary segregation of solute or impurity atoms. Researchers at Oak Ridge [26, 27] and Harwell and Loughborough [22,24] have utilised this technique to investigate irradiation-induced grain boundary segregation in austenitic stainless steels [26, 27] and grain [24] and lath [22] boundary segregation in ferritic-martensitic steels.

In addition, electron energy loss spectrometry (EELS) can be employed in microanalysis. The analysis of the distribution of electron energies emergent from a thin foil specimen is termed EELS. As a microanalytical technique, EELS is complementary to energy dispersive X-ray microanalysis (EDX) in that it is more sensitive to light elements where conventional EDX is limited. Unlike EDX (and other analytical techniques such as AES), EELS is concerned with detecting the primary event, namely the loss of electron energy due to an inelastic interaction, and not a secondary event connected with the return of the atom to ground state. Since the secondary events are usually competitive they are accordingly less efficient signals to seek.

In principle, energy loss measurements should be much more effective than X-ray techniques for low atomic number elemental detection as well as microanalysis. However, the application of EELS to materials is not yet as wide as that of EDX as there are specific experimental limitations, generally with respect to the specimen thickness and also the precision and ease of quantification.

3.2. Experimental results

There have been many experimental studies of irradiation-induced segregation. It is well confirmed [1,43] that irradiation facilitates the segregation of undersized solutes to defect sinks whereas it causes oversized solutes to be depleted. The results imply that complicated interaction between solute atoms and defects takes place depending on the type of defects and the size of solutes during irradiation. In this section, some existing experimental results on irradiation-induced segregation will be briefly presented.

3.2.1. Segregation in austenitic alloys

Rehn et al. [6] investigated irradiation-induced solute segregation to free surfaces in four binary alloys of 1 at% Al, Ti, Mo and Si in Ni. In this study, the samples were irradiated with 3.5-MeV Ni^+ ions at temperatures between 385 and 660 °C. Auger analysis of the solute concentration as a function of depth indicates that the oversized solutes, Al, Ti and Mo, are depleted near the irradiated surface whereas the undersized solute, Si, is enriched; The magnitude of this irradiation-induced segregation in the Ni-1 at%Si alloy is sufficient to result in precipitation of a surface layer of Ni_3Si after a total dose of 5 dpa near 600 °C; the segregation diminishes at both lower and higher temperatures. Ratios of the solute-to-nickel Auger peak-to-peak amplitudes measured for several samples are shown in Fig. 3.1 as a function of depth from the irradiated surface.

The three oversized solutes (Ti, Al and Mo) exhibit a depleted zone close to the irradiated surface followed by a region of solute enrichment; the undersized solute Si exhibits an enriched zone at the surface followed by a depleted region. The Si/Ni peak-to-peak ratio in the surface-enriched zone corresponds to ~25 at%Si as determined by AES analysis of samples of known Si concentration, indicating the formation of a surface film of the Ni_3Si phase. Rehn et al. [6] studied the dependence of Si segregation on irradiation temperature in a Ni-1 at%Si alloy. The Si depth profiles, determined by AES, are shown in Fig. 3.2. Little segregation occurs below ~400 °C and above ~660 °C. The Si/Ni Auger ratio of 0.033 in this figure corresponds to a silicon concentration of 25 at% (see Fig. 3.3), indicating that at intermediate temperatures segregation of silicon takes place at a sufficient rate to form a thin layer of the Ni_3Si γ -phase. The film growth rate and hence the segregation rate may be seen to undergo a maximum at ~560 °C, i.e., there exists a peak segregation temperature for irradiation-induced segregation, which is in line with the theoretical prediction [28, 38].

The major cause of irradiation-assisted stress corrosion cracking (IASCC) is the grain boundary depletion in chromium. There have been several studies of the magnitude of grain boundary chromium depletion in 300 series stainless steels as a function of alloy impurity content for both neutron and ion irradiations. Chung et al. used AES to measure irradiation-induced grain boundary segregation in a commercial purity (CP) heat and a high purity (HP) heat of type 304 steel after neutron irradiation and found greater grain boundary chromium depletion in the HP alloy [81]. Jacobs et al. adopted AEM and showed that A HP type 348 heat

required ~2.3 times higher dose to produce similar grain boundary chromium depletion as in a CP 348 heat [82].

Carter et al. [27] investigated irradiation-induced grain boundary segregation in 304L stainless steel. In their work, controlled purity alloys of 304L stainless steel were irradiated with protons at 400 °C to a dose of 1 dpa and analysed via FEGSTEM. The alloys studied were an ultra-high purity (UHP) alloy and UHP alloys containing phosphorus (UHP+P), and silicon (UHP+Si). The measured segregation profiles for all of the alloys are shown in Fig. 3.4. The profiles providing the best agreement with the mean grain boundary value are presented for each alloy. Greater degrees of chromium and nickel segregation are observed in the UHP+P alloy than those in the UHP alloy, possibly showing a synergism between radiation-induced segregation and the presence of impurities. Phosphorus enrichment of 1.4 at% is measured in the grain boundary of the UHP+P alloy. The chromium concentration at the boundary drops to 16.5 at% from the bulk concentration of 21.02 at% and the nickel concentration increases to ~12.0 at% from the bulk concentration of 8.68 at% in the UHP+P alloy. The UHP+Si alloy shows the most segregation at grain boundaries, with chromium concentration dropping to 14.4 at% from the bulk concentration of 20.41 at%, nickel enriching to 13.1 at% from the bulk concentration of 8.55 at%, and silicon enriching to 3.2 at% from the bulk concentration of 0.87 at%.

A lot of work on radiation-induced segregation in 304 stainless steel has also been done at the Berkeley Technology Centre of the Nuclear Electric in the UK by using FEGSTEM and AES [83]. It was found that radiation-induced segregation of silicon, phosphorus, nickel and an unidentified element producing an Auger peak at 59 eV occurred in the CP (commercial purity) material whereas such segregation was negligible (except for Ni) in the HP (high purity) 304 stainless steel. However, chromium depletion was more pronounced in the HP 304, and for this the authors postulated a relationship between impurity segregation and chromium depletion such that higher levels of the former inhibited the latter.

Fig. 3.5 illustrates a large number of radiation-induced grain boundary segregation measurements of chromium for 300 series stainless steels as compiled by Bruemmer and Simonen [84]. The majority of the data is based on AEM; however several AES measurements are also involved. The AEM measurements underestimate to some extent the magnitude of the grain boundary depletion, as a result of the analysis volume being similar in spatial extent to the actual segregation profile whereas

AES measurements should supply a closer estimate to the grain boundary depletion for intergranular fractures. As the dose rises, the degree of chromium depletion increases to saturation, easily reaching levels where intergranular stress corrosion cracking (IGSCC) emerges for thermally sensitised materials. A second point of interest is that the initial chromium levels at low doses [$< 5 \times 10^{20}$ n/cm² (0.8 dpa)] surpass the bulk chromium concentration of the alloy. Such a chromium enrichment has been associated with phosphorus segregation and has been attributed to equilibrium enrichments of those elements prior to irradiation. Similar co-segregation of phosphorus, chromium, and molybdenum have been found in unirradiated type 300 stainless steels [85,86].

3.2.2. Segregation in ferritic alloys

Definitive experimental data on irradiation-induced segregation in ferritic alloys are significantly more limited compared with those available for austenitic alloys. Published studies have included binary [17,87-89], ternary [17,90], commercial pressure vessel steels [25] as well as 10-12% Cr martensitic grades, i.e. HT9 [23,88,89,91], 1.4914 [20] and FV448 [22]. The data are based on electron [87, 90], ion [20, 88, 89] and neutron [17,22,25,91] irradiations in the temperature range ~300-625 °C at doses from <1 to 46 dpa. The techniques of Auger electron spectroscopy (AES) [17,23,88,89,91], atom probe field ion microscopy (APFIM) [25], energy dispersive X-ray analysis/scanning transmission electron microscopy (STEM) [20,87,90], and high spatial resolution field emission gun scanning transmission electron microscopy (FEGSTEM) [22] have been used to determine solute profiles.

Kameda and Bevolo [17] studied neutron irradiation-induced grain boundary solute segregation in Fe-base alloys. It was found by fracture surface Auger analysis that while neutron irradiation enhanced grain boundary segregation of S in an Cu-doped alloy with the absence of P segregation, it mitigated S segregation and promoted P segregation in P-containing alloys. The magnitude of segregated P was much greater for the irradiated alloys than for the thermally 1000 h aged alloys. Miller and Burk [25] investigated neutron-irradiated pressure vessel steels using APFIM and found that the grain boundaries were enriched in phosphorus, nickel and manganese and that phosphorus segregation was observed to almost all microstructural features.

The most recent data on radiation-induced segregation to martensite lath boundaries in FV448 martensitic plate [22], determined by FEGSTEM, serve to illustrate the

form of the solute redistribution profiles as a function of distance from the sink. Fig. 3.6 illustrates typical concentration profiles for Cr, Ni, Si and Fe on either side of a martensite lath boundary in FV448 steel following fast reactor irradiation at 465 °C to 46 dpa [22], which shows that Ni and Si are enriched at the sink and Fe is depleted; Cr is locally enriched at the sink but depleted in the adjacent matrix, and this is explained in terms of competing effects between thermal and radiation-induced segregation [92].

Appendix 3.1
Figures for Chapter Three

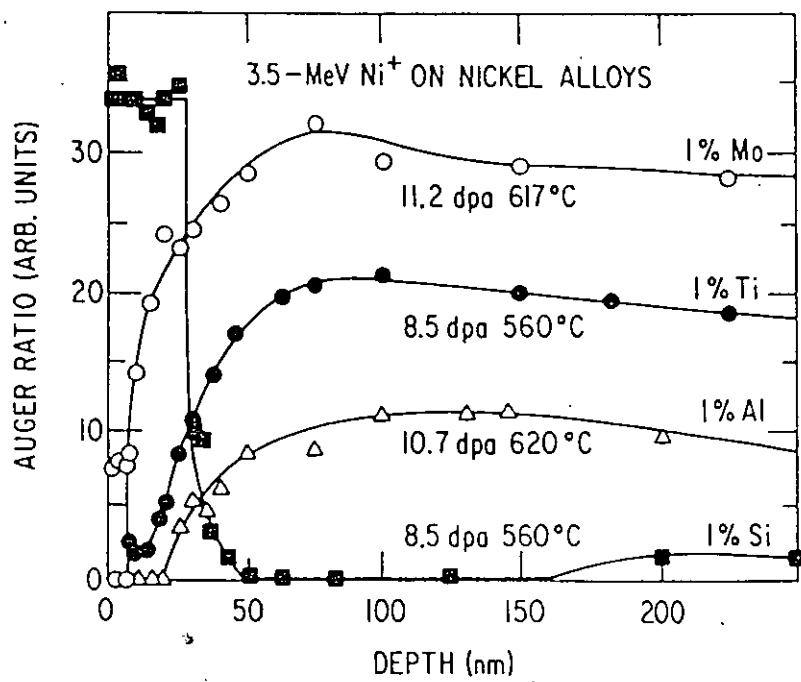


Fig. 3.1. AES chemical depth profiles of solutes in a series of 1 at%Ni alloys after ion irradiation at the temperatures and doses indicated, after Rehn et al. [6].

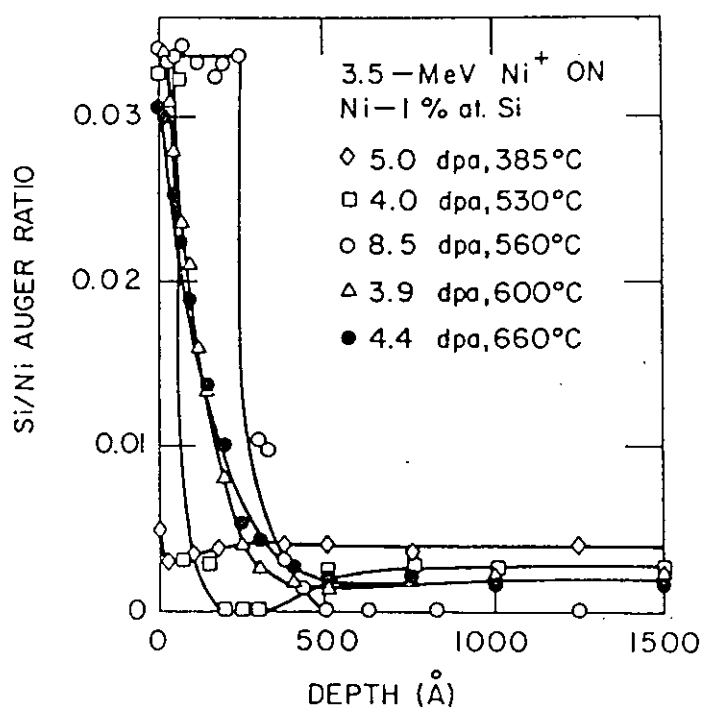


Fig. 3.2. Si/Ni peak-to-peak ratios versus depth from the irradiated surface for a series of Ni - 1 at%Si alloys irradiated at various temperatures and doses indicated. A Si/Ni ratio of 0.033 corresponds to 25 at%Si, after Rehn et al. [6].

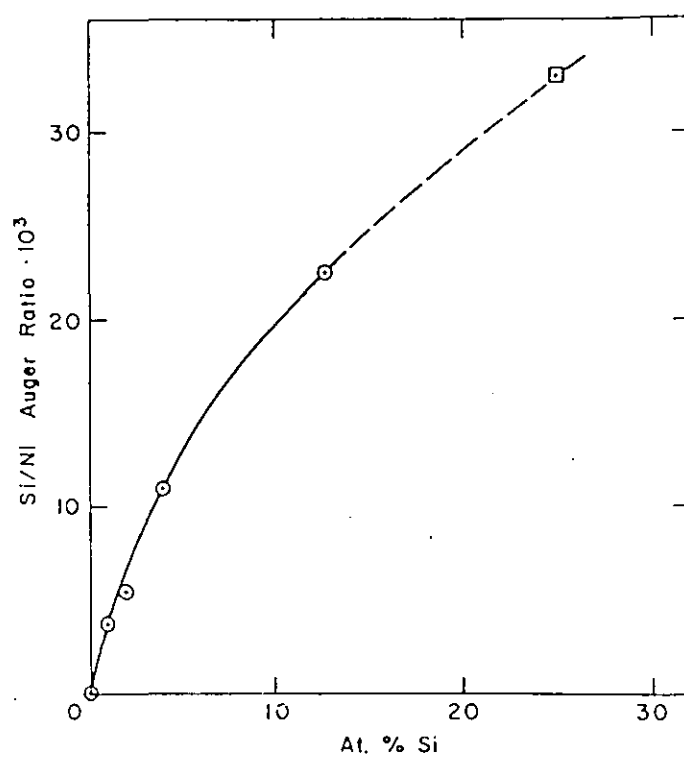


Fig. 3.3. Measured Si/Ni Auger peak-to-peak ratios in samples of Ni containing known concentrations of Si, after Rehn et al. [6].

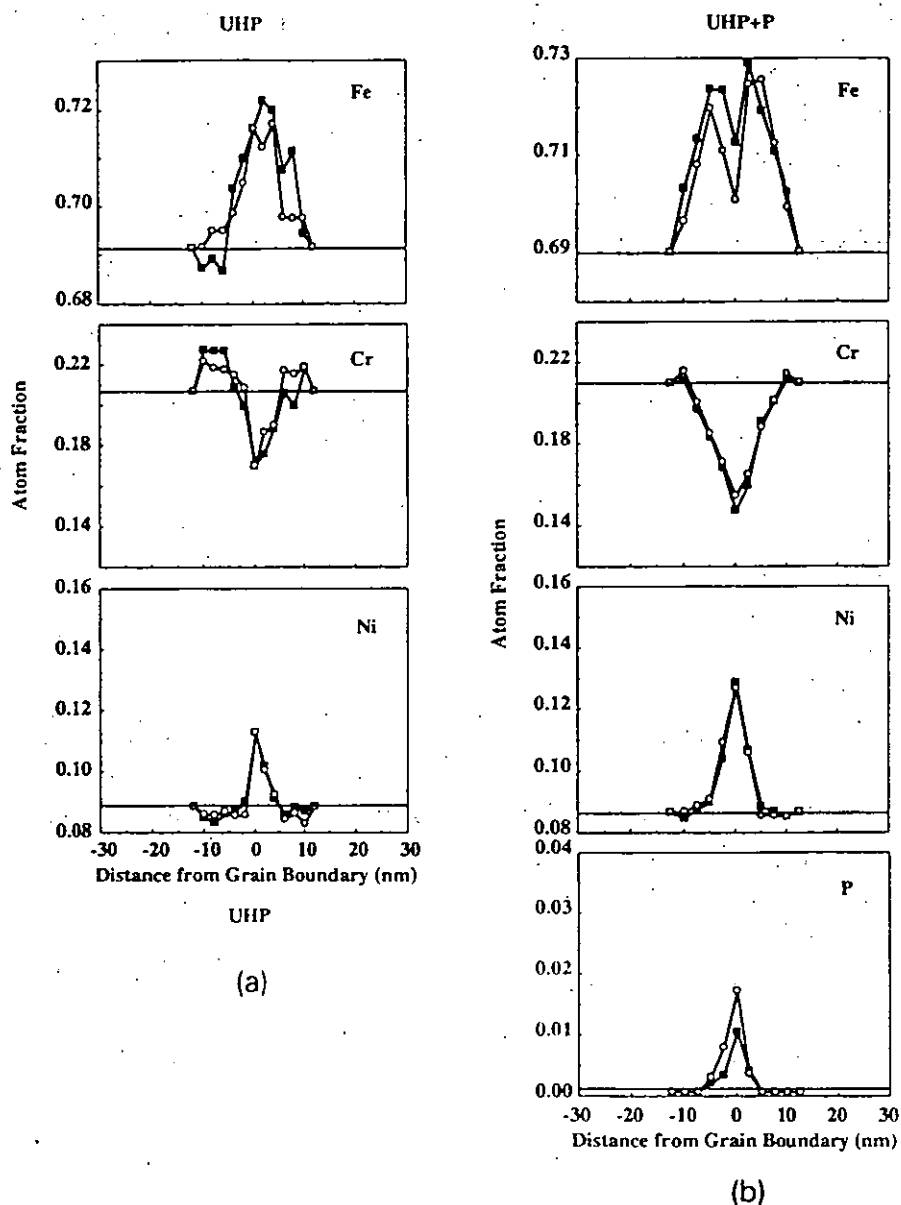


Fig. 3.4. FEGSTEM/EDS measured composition profiles across two grain boundaries for Fe, Cr, Ni and Impurity elements, included: (a) UHP alloy; (b) UHP+P with P profiles; and (c) UHP+Si alloy with Si profile. The horizontal line in each graph denotes the bulk concentration of the element. After Carter et al. [27].

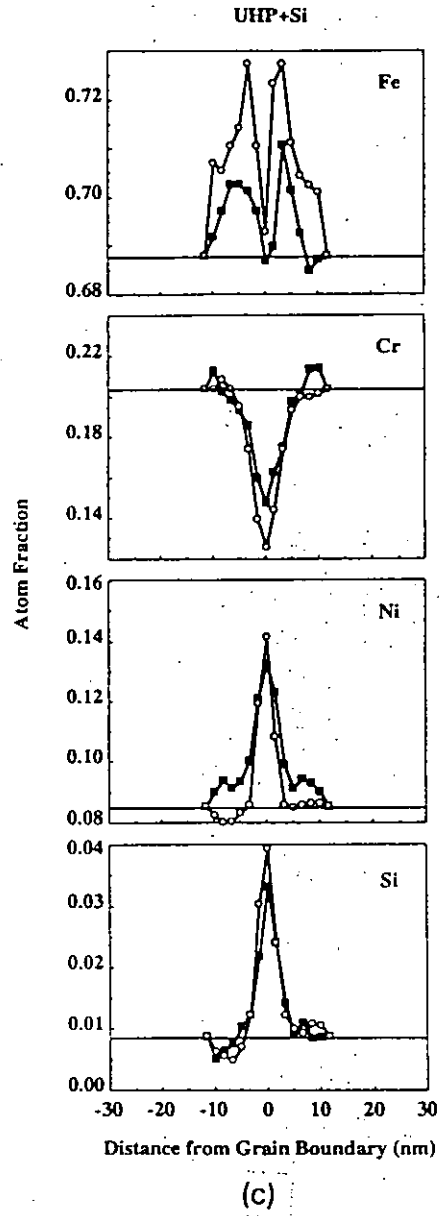


Fig. 3.4 (continued)

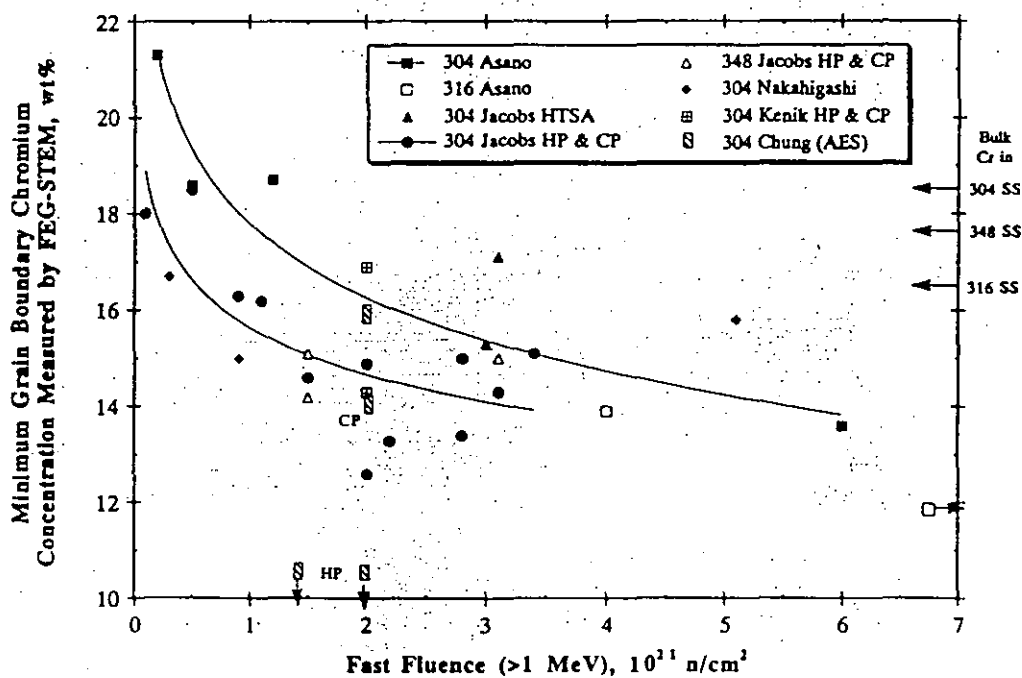


Fig. 3.5. Comparison of a large number of irradiation-induced grain boundary segregation measurements of chromium as a function of neutron fluence for a series of 300 series stainless steels, compiled by Bruemmer and Simonen [84]. Nominal alloy chromium levels are indicated on the right side of the figure for comparison.

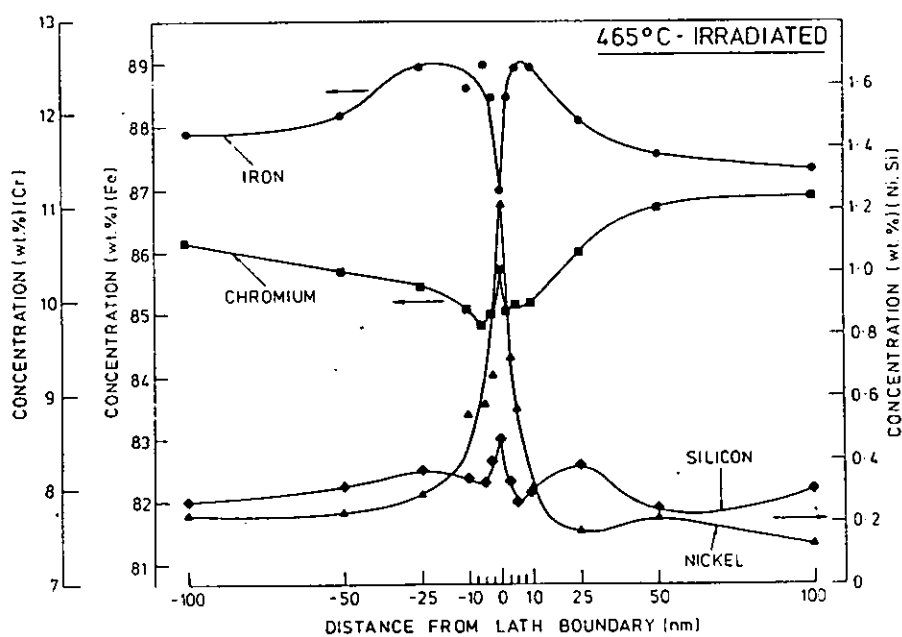


Fig. 3.6. Typical concentration gradients for Cr, Ni, Si, and Fe on either side of a martensite lath boundary after 465 °C irradiation to 46 dpa, after Morgan et al. [22].

Chapter Four

Effects of Radiation-Induced Segregation on Properties of Alloys

Since irradiation gives rise to segregation of impurity or alloying elements near internal sinks such as grain boundaries and external surfaces, i.e. the alloy composition in the vicinity of the sinks is varied, this irradiation-induced segregation will influence a number of bulk and surface properties, which is susceptible to the alloy composition, for instance, phase stability, void swelling, mechanical properties and corrosion resistance. These effects will be briefly described in this chapter.

4.1. Effect on phase stability

When the local concentration of an alloying element exceeds the solubility limit for transformation a new phase may form. The local regions may be highly enriched or depleted in solute in comparison to the bulk. As discussed above, such segregation usually takes place at point defect sinks.

Several researchers [93-95] have investigated precipitate development in 12%Cr steels during irradiation and their results on the formation and stability of radiation-induced phases have recently been reviewed by Maziasz [96]. A number of radiation-induced phases have been observed to form, which could be associated with radiation-induced segregation to defect sinks.

4.2. Effect on void swelling

The effect of solute segregation on swelling of metals and alloys has been studied by Lam et al. [97-101]. The formation of voids, which leads to swelling of materials, depends on several factors, one of which is the composition of the material, including the concentration of trapping sites for mobile defects. The swelling suppression that arises from trapping of point defects by minor additions of alloying elements, is affected by irradiation-induced solute redistribution in alloys. If the interaction between point defects and solute atoms are sufficiently strong, appreciable solute segregation occurs during irradiation, resulting in a solute depletion or enrichment at defect sinks.

For a given damage rate and strong solute-interstitial binding, solute depletion in the matrix at temperatures below the peak swelling temperature of the alloy makes the defect trapping effects insufficient. At higher temperatures, segregation is reduced so that the trapping centres remain relatively uniformly distributed and void

swelling is suppressed. The net result is a shift of the peak swelling to lower temperatures for the case of strong solute-interstitial binding. The depletion of solute traps and thus the loss of swelling resistance is especially severe as irradiation-induced segregation brings about precipitation of the solute. An increase in solute concentration would be beneficial until the excess solute has precipitated out. For dominant vacancy interactions, solute depletion near the sinks and hence solute enrichment in the matrix may take place for very weak solute-vacancy binding. In this case, void swelling decreases monotonically when the solute concentration increases. For very strong solute-vacancy binding, solute depletion in the matrix may appear so that void swelling increases.

4.3. Effect on ductility of ferritic steels

For ferritic steels there is a well-known ductile-brittle transition. Above the ductile-brittle transition temperature (DBTT) the material fails in a ductile mode, and the fracture toughness, a measure of the energy required to cause fracture, is high. Below the DBTT the material fails in a brittle mode, and the energy required to cause fracture is low. Irradiation of ferritic steels causes the DBTT to increase and also reduces the energy for fracture in the ductile region. This is a problem of current concern in light-water reactor pressure vessel steels. Of most concern is the possibility that with large DBTT shifts, the brittle behaviour may be encountered in the temperature regime of normal reactor operation or of reactor shutdown.

Metallurgical research has led to substantial improvements in this area. The poor behaviour of some steels has been correlated with the level of alloying, especially of copper, phosphorus and nickel. Steels with more than 0.15 copper generally exhibit high sensitivity to irradiation. Those with levels less than 0.10% are much improved. Fig. 4.1 (bottom) shows the results for A533-B type steel containing controlled amounts of copper (0.10%) and phosphorus (0.012%) [47]. For comparison, Fig. 4.1 also shows (top) the results on the same type of steel, where the copper and phosphorus contents were not controlled. The shift in the DBTT is reduced by nearly a factor of four for the copper/phosphorus-controlled steel, compared with the uncontrolled steel. Nickel content has also been associated with the poor irradiation response. Fig. 4.2 shows the results of Charpy-V notch tests on ferritic weld metals containing similar copper (0.10%) and phosphorus (0.017%) contents but differing in nickel content by an order of magnitude [48], which indicates that the higher nickel alloys exhibit considerably higher DBTT.

It is clear [49] that embrittlement of reactor pressure vessel steels is classified into non-hardening embrittlement and hardening embrittlement. The non-hardening embrittlement is generally associated with intergranular failure resulting from grain boundary segregation of impurities such as P, S, As, Sn and Sb. However, During irradiation, grain boundary segregation of phosphorus, which gives rise to shifts of DBTT to higher temperatures, plays a dominant role in the non-hardening embrittlement. The hardening embrittlement arises from the production of hardening centres, both precipitates and matrix defects. The precipitation of copper to supply effective dislocation pinning sites with a resultant increase in hardness and a shift in DBTT to higher temperatures plays a dominant part in the hardening embrittlement. For the role of nickel in RPV steels containing copper it is now well established that irradiation-induced hardening embrittlement is due to irradiation-enhanced precipitation of copper due to the increased vacancy concentration. In high nickel variants, the nickel actually alloys with the copper causing a change in precipitation kinetics and thus a change in precipitate number density; also the nickel in the copper changes the modulus of the copper precipitate which thereby changes its strength by the modulus hardening reaction with dislocations. In either way the nickel can thus change radiation-induced embrittlement. In fact, the most recent studies show [50] that the nickel is concentrated in an outer shell on the copper precipitates - hence the nickel effect is even more complicated.

A similar phenomenon occurs in ferritic stainless steels [102-104]. These steels contain much higher chromium levels than the pressure vessel steels and are possible candidates for the much higher dose applications of fusion reactor first walls and coolant ducts in sodium-cooled fast breeder reactors. For these steels there may be a significant shift in DBTT after irradiation ($> 120^{\circ}\text{C}$ in alloy HT-9 containing 12 %Cr) and a lowering of the upper shelf energy. Segregation of alloying elements and impurities to defect sinks such as grain boundaries could be partially responsible for this.

4.4. Effect on stress corrosion cracking of austenitic stainless steels

Irradiation-assisted stress corrosion cracking (IASCC) has been described as the accelerated intergranular cracking of materials exposed to radiation [105,106], and is a main concern in light-water reactors around the world. The growing body of research regarding IASCC has identified some of the major material and environmental factors involved. Much research has been carried out to characterise the role of environmental factors, principally oxygen concentration, electrochemical potential and impurity concentration, on the crack propagation rate in furnace-

sensitized austenitic stainless steels at high temperatures [107-109]. However, the difficulty, expense, and time needed to test neutron-irradiation samples has meant that the stress corrosion cracking consequences of irradiation-induced microstructural and microcompositional changes have not yet been extensively studied. Usually, the microstructural and microchemical features, or persistent effects due to neutron exposure are modelled by other forms of radiation such as heavy ions, helium, and protons in much less time and with little or no sample activation.

The majority of light water reactor (LWR) experience with IASCC failures is concentrated on austenitic alloys in high temperature water. Though both intergranular and transgranular SCC failures are possible, the preponderance of IASCC failures have been intergranular in nature. Alloys which are otherwise immune to cracking have been shown to be susceptible after exposure to neutron irradiation. The observation of cracking is unexpected based on causes for sensitisation, i.e., chromium depletion associated with grain boundary carbide precipitation. Alloys susceptible to IASCC do not exhibit grain boundary carbides and thus alternative radiation-induced reasons could be radiation-induced chromium depletion at grain boundaries.

As described above, depletion of chromium at grain boundaries without carbide precipitation has been measured in neutron-irradiated stainless steels. Significant levels of grain boundary chromium depletion result in active path corrosion at grain boundaries and hence may lead to IGSCC. The inverse Kirkendall vacancy mechanism could be the likely radiation mechanism for chromium depletion in the absence of grain boundary carbides. This is because the chromium level in stainless steels is so high and moreover it will be seen from Section 6.1. that in γ -Fe the chromium-interstitial and -vacancy binding energies should be so low that the solute-point defect complex mechanism could be no longer valid. In the light of the inverse Kirkendall vacancy mechanism, fast-diffusing solutes such as chromium and molybdenum in austenitic stainless steels preferentially exchange with the vacancy fluxes leading to a depletion of such fast-diffusing elements at point defect sinks such as grain boundaries. Of the major components in austenitic stainless steels, nickel has the slowest diffusion rate and thus enriches at grain boundaries.

In addition to chromium depletion, enrichment of impurities such as phosphorus and silicon at grain boundaries has also been measured in neutron-irradiated alloys [80, 81]. Cookson et al. [110-112] investigated in detail irradiation-assisted stress

corrosion cracking (IASCC) of controlled purity 304L austenitic stainless steels. The effect of chromium, phosphorus, and silicon on the stress corrosion cracking of the 304L stainless steel in constant extension rate tensile (CERT) tests in high purity water or argon at 288 °C following irradiation with 3.4 MeV protons at 400 °C to 1 dpa was studied using ultrahigh purity(UHP) alloys with controlled impurity additions. Grain boundary segregation of phosphorus(UHP+P) or silicon(UHP+Si) due to proton irradiation was quantified by using both AES and FEGSTEM. The alloys with impurity element addition were observed to have greater grain boundary chromium depletion and nickel enrichment than the UHP alloy. The UHP alloy suffered severe cracking in CERT tests in the higher temperature water , and less cracking was found after CERT tests of irradiated UHP+P and UHP+Si alloys, in spite of greater chromium depletion. Consequently, their results suggest that phosphorus and silicon is not detrimental and perhaps beneficial, while chromium depletion may be deleterious in the IASCC of proton-irradiated type 304L stainless steel.

Other impurities identified at the grain boundaries of alloy 600 (a nickel-base stainless alloy) include boron and sulphur. Grain boundary segregation of boron and sulfur has been observed, even when bulk contents are only several parts per million [113]. Boron may be particularly important since it is often observed at grain boundaries of mill-annealed specimens [114], and quite easily segregates to grain boundaries by thermal equilibrium and non-equilibrium segregation mechanisms [115-117]. However, boron segregation has not been shown to induce intergranular (IG) corrosion or stress corrosion cracking (SCC). Since low levels of boron retard chromium carbide precipitation and higher levels accelerate precipitation, boron may affect SCC through its effect on IG chromium carbide formation kinetics [118]. Sulphur has not been shown to consistently segregate to grain boundaries in alloy 600 due to the presence of sulphide formers such as magnesium, calcium and titanium. Significant segregation has only been addressed in samples after extremely high-temperature anneals (>1300 °C) where sulfur is released from pre-existing inclusions and is able to segregate to grain boundaries. Although sulphur has been proposed to play an important part in IGSCC, it is unlikely based on the limited segregation that occurs in alloy 600 tubing under normal processing and fabrication conditions. In the irradiated samples of 304L stainless steel, there is no apparent segregation of sulphur to grain boundaries and hence no considerable effect of sulphur on the IGSCC [110-112].

It is worth mentioning that the simulation of neutron irradiation by other forms of irradiation such as heavy ions, helium, and protons in much less time appears to be improper. This is because the microstructural and microchemical changes due to irradiation are associated with irradiation temperature and time, which means that the dose rate plays an important part in the kinetic processes.

Appendix 4.1
Figures for Chapter Four

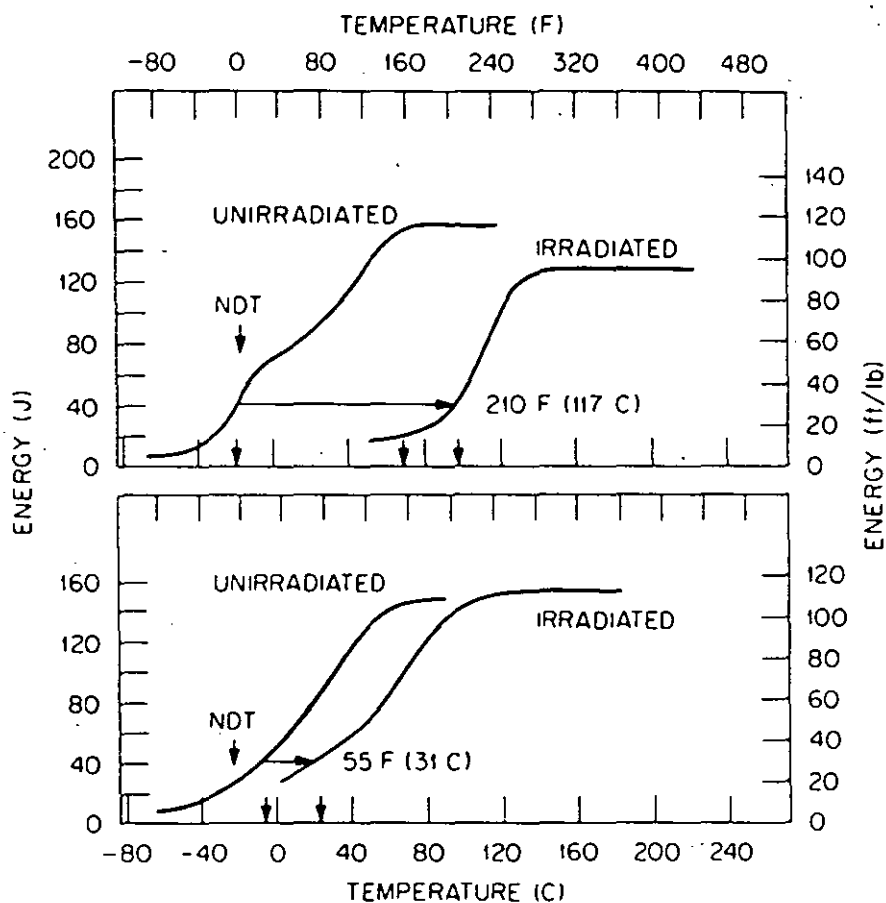


Fig. 4.1. Results of Charpy V-notch tests on A533-B pressure vessel steel. Material was irradiated to about 6×10^{23} n/m² (neutron energies > 1 MeV) at 288 °C. Upper plot shows material in which copper and phosphorus contents were not controlled, and lower plot shows improved material in which copper and phosphorus were reduced to lower levels. After Ref. 46.

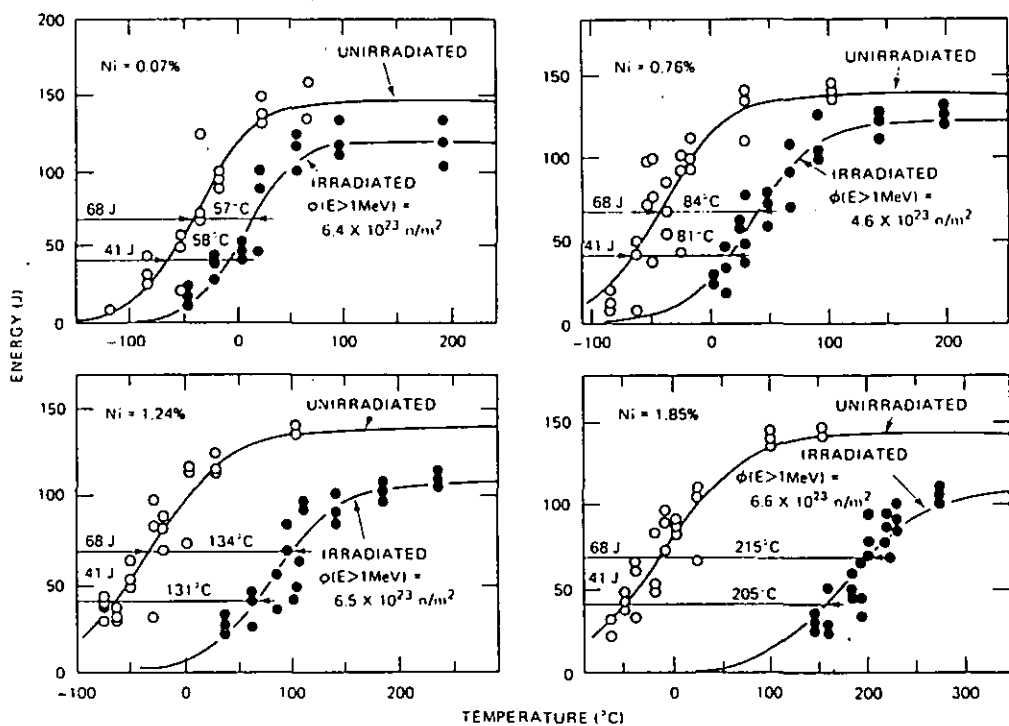


Fig. 4.2. Results of Charpy V-notch tests on ferritic weld metals differing in nickel content by an order of magnitude. The irradiation-induced temperature shifts are indicated at both 41 and 81 J. Irradiations were done at 288 °C. After Ref. 47.

Chapter Five

Production of Point Defects and Their Interactions with Solutes

Radiation-induced solute segregation is a kinetic process controlled by point defects (vacancies and interstitials) created by irradiation. As a consequence, it is necessary to briefly describe irradiation damage and point defect-solute interactions.

5.1. Primary recoil spectra

The first step in understanding damage production is to determine the primary recoil energy spectra produced by irradiating particles such as neutrons. The upper limit of recoil energy is useful as a benchmark. For projectiles whose rest energy is large compared to their kinetic energy, such as neutrons or ions in the MeV range, classical collision theory is adequate to describe the energy transfers in elastic collision. Conservation of energy and momentum gives the result

$$T_i = \frac{4E_1 M_1 M_2}{(M_1 + M_2)^2} \quad (5.1)$$

where T_i is the maximum possible energy transfer from a projectile of mass M_1 and kinetic energy E_1 to a target atom of mass M_2 . The corresponding relativistic expression for the maximum energy transfer to a target atom by an electron of kinetic energy E_1 and rest mass M_1 is

$$T_i = \frac{2E_1(E_1 + 2M_1c^2)}{M_2c^2} \quad (5.2)$$

where c is the speed of light.

The maximum energy transfer can only take place in head-on collisions. Other collisions result in lower energy transfers. Irradiating a target with monoenergetic projectiles generates a complete range of elastic and inelastic collisions, resulting in a corresponding distribution of recoil energies. This probability distribution has a characteristic shape for each type of projectile and is a fundamental concept in the calculation of damage production. The probability is depicted by a cross section that has units of area. In detail, the primary recoil spectrum is often described by a differential cross section, this being the derivative of the cross section with respect to energy. It depicts the probability of producing a recoil with an incident projectile in a given differential energy interval.

For ions the primary recoil spectrum is given by the Rutherford differential scattering cross section

$$\frac{d\sigma}{dT_g} = \frac{\pi M_1 Z_2^2 Z_1^2 e^4}{M_2 E_1 T_g^2} \quad 0 < T_g \leq T_i \quad (5.3)$$

where σ is the scattering section;

Z_1 and Z_2 are the atomic numbers of projectile and target, respectively;

e is the charge of the electron; and

T_g is the energy transferred to the target atom.

Note the inverse square dependence on T_g , thus strongly favouring low-energy transfers. At very high energies, a few Mega-electron-volts (MeV) per projectile nucleon, this cross section must be corrected both for nuclear forces and for inelastic nuclear collisions. At the opposite extreme, at energies below about

$$Q_2 = (24.8 \text{ KeV}) M_1 Z_1^{1/2} \quad (5.4)$$

Capture of electrons by the projectile in the target becomes significant [119]. The atomic interaction again then differs significantly from the interaction between the projectile and nucleus, described by Equation (5.3). As a result, for much of the heavy ion irradiation work in progress, the cross section of Equation (5.3) is not generally applicable, but for typical light-ion irradiation experiments, it is quite good.

For heavy ions below Q_2 , the theory of Lindhard, Scharff and Schiott (LSS) [120] may be used. This is an energy partition model where energy loss is divided into electronic and nuclear components. The differential scattering cross section of this model gives a primary knock-on atom (PKA) spectrum that obeys a dependence on PKA energy similar to that of Equation (5.3) - it decreases with increasing T_g only slightly less rapidly than T_g^{-2} .

For neutrons in the range from the lowest energy which can produce displacement to 1 MeV, the elastic scattering dominates. A simple approximation is the isotropic elastic scattering expression

$$\frac{d\sigma}{dT_s} = \frac{\sigma_e}{T_s} \quad \text{for } T_s < T_i \quad (5.5)$$

where σ_e is the total elastic scattering cross section that is energy-dependent. This model is fairly accurate up to about 0.1 MeV, but it is inadequate at energies of 1 MeV and above. The elastic scattering distribution at these higher energies is complex, details of which may be found elsewhere [119]. Low-energy transfers are favoured. Above about 1 MeV non-elastic processes begin to contribute where the nucleus is excited by the incident neutron and emits a particle.

5.2. Defect production

In terms of the LSS theory, Energy loss by the PKA occurs by both electronic and nuclear processes. In metals and alloys it is usually assumed that only the energy lost in nuclear collisions can displace atoms. This energy is denoted as T_d . A standard procedure for the calculation of T_d can be found in Ref. [119].

The energy transferred in nuclear collisions, the damage energy is translated into displaced atoms via a secondary displacement model. Secondary displacements are all atoms that are displaced in the stopping of a PKA. The following model based on the initial work of Kinchin and Pease [121] is widely utilised:

$$\begin{aligned} N_d &= 0 & T_d &< E_d \\ N_d &= 1 & E_d &\leq T_d < 2E_d \\ N_d &= \frac{\gamma T_d}{2E_d} & T_d &\geq 2E_d \end{aligned} \quad (5.6)$$

where N_d is the number of displaced atoms, or vacancy-interstitial pairs, and E_d is a threshold energy, generally in the range of tens of electron-volts (eV), which is required to displace an atom. The recommended value of γ is 0.8, and this accounts for the deviation from the hard sphere model of the interatomic potential [122].

A link with common experimental situations is supplied by the following sketch. The rate of displaced atom production, G , is approximately given by [123]

$$G = \sigma_d \phi N_d \rho_A \quad (5.7)$$

where σ_d is the spectrum-averaged displacement cross section;
 ϕ is the neutron flux; and

ρ_A is the atomic density, i.e. the number of atoms per unit volume.

In a liquid metal fast breeder reactor (LMFBR), the mean neutron energy is about 0.6 MeV. The mass M_2 of the major constituent atoms in stainless steels is about 60 in units of neutron mass, and the maximum energy transferred from a neutron of mean energy is then about 40 KeV, obtained from Equation (5.1). As a consequence, N_d , The number of atoms displaced by a typical PKA, created by fast reactor neutron irradiation is of the order of 100. Fast fission reactors typically have a neutron flux of $\sim 10^{19} \text{ m}^{-2}\text{s}^{-1}$, and the displacement producing collision cross section of the nuclei of the structural materials is about 10^{-27} m^2 . The result is $\sim 10^{23}$ displacements/(m^3s). In fusion reactors, the neutron fluxes are somewhat lower, but the number of atoms displaced by a typical PKA is higher because its higher energy. Hence the resulting displacement rate is similar to that of fast reactors. Normalised to the atomic density, this gives $\sim 10^{-6}$ displacements/(atom.s). The meaning of this is that after 10^6 seconds, roughly 12 days, every atom in the structural material of a reactor has on the average been displaced once by neutron irradiation. The unit displacements per atom (dpa) is a convenient measure of the dose of displacement-creating radiation.

The most common means of calculating defect production in metals is by the method of Norgett, Robinson and Torrens (NRT) [124], which is essentially the modified Kinchin-Pease expression, integrated over the primary recoil spectrum of the irradiation particle, i.e.,

$$v^p(E) = \rho_A \Delta x \int_{T_{\min}}^{T_{\max}} dT_r \frac{d\sigma(E, T_r)}{dT_r} v(T_r) \quad (5.8)$$

where $v^p(E)$ is the number of Frenkel pairs created in a material of thickness Δx by a primary particle, p , with initial energy E ; $d\sigma(E, T_r)/dT_r$ is the differential cross section for a particle of energy E to produce a recoil of energy T_r ; T_{\min} and T_{\max} are the minimum and maximum energies of recoils, respectively; and $v(T_r)$ is the damage function. Usually the modified Kinchin-Pease expression for $v(T_r)$ is employed in defect calculations,

$$v^{KP}(T) = \begin{cases} 0 & \text{for } T_r < E_d \\ 1 & \text{for } E_d < T_r < 2.5E_d \\ \frac{0.8E_d(T_r)}{2E_d} & \text{for } T_r > 2.5E_d \end{cases} \quad (5.9)$$

where $E_D(T_r)$ is the damage energy associated with a recoil of energy T_r , \bar{E}_d is the average displacement energy and E_d is the threshold displacement energy. Division of Equation (5.8) by $\rho_A \Delta x$, the number of atoms per unit area within a slab of thickness Δx , yields the number of times for which each atom within the target is displaced per unit fluence and is called the "Frenkel-pair cross section",

$$\sigma_{FP} = \int_{T_{min}}^{T_{max}} dT_r \frac{d\sigma(E, T_r)}{dT_r} v(T_r). \quad (5.10)$$

The product of the Frenkel-pair cross section and particle fluence, therefore, produces the number of times for which each atom is displaced during irradiation, i.e. the number of displacements per atom (dpa).

$$dpa = \Phi \sigma_{FP} = \Phi \int_{T_{min}}^{T_{max}} dT_r \frac{d\sigma(E, T_r)}{dT_r} v(T_r) \quad (5.11)$$

where Φ is the fluence of irradiation. The use of dpa thus provides a convenient means to normalise the fluence when comparing effects brought about by different types of irradiation.

For ion irradiation, since ions slow down quickly in solids and thus their energy is not constant, it is necessary to rewrite Equation (5.8) using the relation

$$\frac{dE}{dx} = \rho_A [S_n(E) + S_e(E)]. \quad (5.12)$$

Consequently, substituting Equation (5.12) into Equation (5.8) yields

$$V^P(E) = \int_{E_d}^E \frac{dE}{S_n(E) + S_e(E)} \int_{T_{min}}^{T_{max}} dT_r \frac{d\sigma(E, T_r)}{dT_r} v(T_r). \quad (5.13)$$

This is the total number of defects produced as an ion is stopped in a material. Here $S_n(E)$ and $S_e(E)$ are the nuclear and electronic stopping powers, respectively. Calculations of damage production(dpa) in this case are more difficult. The details about this may be seen in Ref. [124].

It is convenient to think of Equation (5.13) in three parts. The outer integral over E describes how the particle slows down in the material, depending only on the stopping powers. These functions are well known [125]. The differential cross

section, which is essentially the primary recoil spectrum, depicts the atomic collisions between the particle and the atoms in the target material, and is accurately known too. The last part of Equation (5.13) is the damage function. It depends only on the material and is independent of the type of irradiation. Once the damage function has been specified, defect production may be calculated for any type of irradiation for which the primary recoil spectrum is available.

5.3. Displacement cascade characteristics

The characteristics and structure of the cascade in which point defects and point defect clusters are born is important. A displacement cascade is the branching sequence of collisions initiated by a PKA. Neutron and ion irradiations typically create PKAs with damage energies in the range of many kilo-electron-volts or more. Hence cascades may consist of a number of displaced atoms ranging into hundreds. The interstitials may be produced by simple events where an atom is knocked from its equilibrium site and reaches thermal energies in an interstitial position. Interstitials are also produced by the replacement collision sequence (RCS). Here the vacancy member of the defect pair is created by placing the corresponding atom on the next lattice site and the atom on that lattice site is nudged onto the next site and so on. When the sequence stops, the last atom nudged from its lattice site becomes an interstitial. This is a mechanism for the long-range separation of a vacancy from its interstitial. It may account in part for the form of the cascade - vacancy-rich core surrounded by a shell of interstitials. However, the recent study of Calder and Bacon [126] by means of molecular dynamics computer simulations has shown that individual RCSs play little role in the separation of interstitials and vacancies in cascades in α -Fe, and that the mechanism which leads to the separation, and thus to defect production, is the incomplete relaxation of the collective, focused displacement events, which gives rise to the production of interstitials at the periphery of the cascade zone.

Cascade size increases with increasing PKA energy. Above a certain energy, however, the cascade morphology begins to change. It breaks up into subcascades that are separated each other. Each subcascade has the usual form [127]. In materials of interest for technological applications, subcascade formation takes place as the PKA energy exceeds 30-50 KeV.

After the initial displacement events, mechanical relaxations or collapses of unstable configurations occur. A large number of observations of surviving cascade structures have been made using electron microscopy [127-133]. As a result of

these observations, it has been found that interstitials form clusters, usually dislocation loops, while vacancies may exhibit more variety in their clustering morphologies. Cascade cores often collapse into vacancy loops [128]. Vacancy clustering to create stacking fault tetrahedra is observed in fcc materials such as copper, gold, nickel, Cu_3Au , and austenitic stainless steels [129,130]. A significant observation is that vacancy clusters form in cascades at temperatures both higher and lower than those at which they would be expected to form by homogeneous diffusion and aggregation of thermal vacancies and di-vacancies.

5.4. Point defect-solute interaction

Point defect-solute interactions are generally manifested as the formation of defect-solute complexes. The formation of defect-solute complexes is easiest to visualise, and is conceptually valid in the case of dilute alloys. Here each solute atom may be considered in isolation so that in general each point defect will have only one nearest neighbour solute atom. There would normally be a binding energy between solute atoms and point defects. The binding energy is a result of the relaxation of some of the strain energy related to both species as distinct entities when the two occupy nearest neighbour sites. In the case of irradiated materials there is a non-equilibrium concentration not only of vacancies, but also of interstitials, so that both vacancy-solute and interstitial-solute complexes may form. However it will be seen in Chapter 6 that only undersized solutes have positive binding energies with interstitials.

5.4.1. Vacancy-solute complexes

The formation of a vacancy-solute complex is accomplished by bringing together an isolated vacancy and solute atom to nearest neighbour sites. The binding energy for the complex is the free energy difference of the lattice between the two states. Strain energy relaxation is obviously one factor in determining the binding energy, but so are electrostatic and, in the case of $\alpha\text{-Fe}$, magnetic effects [134].

Despite the importance of the vacancy-solute binding energy to atomistic processes in physical metallurgy, few reliable experimental values have been accommodated even for single solute-monovacancy interactions. Because of its importance and difficulty in measurement, several attempts have been made to theoretically and empirically predict the vacancy-solute binding energy. These have been reviewed by several authors [135,136]. Early models evaluated the electric effects and neglected relaxation effects. More recently models have been based on a pseudopotential method to determine interatomic potentials [137]. However, successful applications of pseudopotentials to a solid are limited to alkali and simple metals. In a recent approach Faulkner [53] has calculated vacancy-solute binding energies, giving values for complexes in iron varying with solute atom radius as shown in Fig. 5.1.

So far there have been few reports on mechanisms for migration of vacancy-solute complexes. As an attempt, the migration process of the complexes is described as follows. with a bcc crystal taken as an example, as illustrated in Fig. 5.2, the vacancy in the complex first jumps from site A to Site B, and then exchanges with the solute atom in the same complex. After jumps depicted above, the position of the complex is shown in Fig. 5.3. This migration mechanism for vacancy-solute complexes are here termed the non-dissociation mechanism.

It is worth mentioning that in this migration process the vacancy has to undergo a jump to a secondary nearest lattice site, and this must overcome a higher potential barrier at the saddle point. If the energy required for overcoming this higher potential barrier is greater than the sum of the vacancy migration (jumping to the nearest lattice site that is occupied by a matrix atom) and vacancy-solute binding energies, the complex migration may take the dissociation mechanism, i.e., partial dissociation and re-formation together with vacancy-solute atom exchange. As illustrated in Fig. 5.4, the vacancy in the complex first jumps from site A to site B and then from site B to site C, and finally exchanges with the solute atom in the same complex. After jumps described above, the position of the complex is the same as that shown in Fig. 5.3. It is clear that the activation energy for this process is dependent on which one is higher in the following two energies: the sum of the vacancy migration and vacancy-solute binding energies or the vacancy-solute atom exchange energy. The migration energy of complexes should be the higher one of the above two energies.

5.4.2. Interstitial-solute complexes

it is well known that the presence of solute atoms interferes with the resistivity recovery of dilute alloys compared with pure metals [138]. The suppression of stages I_D and I_E in recovery experiments on irradiated materials is attributable to an interaction between the solute atoms and self-interstitials. This interaction can lead to the formation of stable interstitial-solute complexes. Their subsequent configuration changes and migration may cause distinct substages in stage II recovery. In addition, the migration of interstitial-solute complexes play an important part in irradiation-induced solute segregation in dilute alloys. To understand this interaction it is helpful to first have a look at the configuration and jump-modes of self-interstitials.

5.4.2.1. Self-interstitial

The configuration of self-interstitials in pure metals has been a subject of extensive discussion during conferences on point defects and reviewed by several authors [72,139,140]. Most attentions have been given to face-centred cubic (fcc) materials, although knowledge regarding body-centred cubic (bcc) and hexagonal materials is improving.

Lattice theory calculations, pioneered by Johnson [141,142], have achieved the most stable interstitial configurations for cubic crystals. The configuration takes the form of a split-interstitial, or dumbbell. Two atoms are associated with a single lattice position. the two atoms have mutually repulsive cores and thus arrange themselves in the form of a dumbbell centred about the normal lattice site. The axis of the dumbbell has been found to be aligned in a $\langle 100 \rangle$ direction for fcc crystals and a $\langle 110 \rangle$ direction for bcc crystals. In order to accommodate the two dumbbell atoms the neighbouring atoms are displaced outwards, producing an elastic strain field around the defect. This long range strain field brings about self-interstitial formation energies being very high such that at thermal equilibrium their concentration is very low.

Jump processes involved in the migration of self-interstitial dumbbells in fcc metals is found to be three dimensional, including a translation with simultaneous rotation, as illustrated in Fig. 5.5(a) [143]. One of the two dumbbell atoms moves towards a nearest neighbour position, displacing the nearest neighbour to form a new dumbbell with this partner, while the old partner returns to its original lattice site, thus allowing long range migration of the dumbbell.

The bcc $\langle 110 \rangle$ dumbbell may undergo an analogous three dimensional jump or a two dimensional jump, shown in Figs. 5.5(b) and 5.5(c), respectively. In the three dimensional jump, there is a simultaneous translation in the original $\langle 110 \rangle$ direction with a 60° rotation to form a new dumbbell, lying on a different $\langle 110 \rangle$ axis. Recent evidence for molybdenum [144] has demonstrated that migration without reorientation may also take place in bcc metals. This two dimensional migration corresponds to a pure translation so that the dumbbell lies on a parallel axis after migration. Johnson [145] has performed energy calculations and suggested a two step process with an intermediate $\langle 223 \rangle$ split interstitial (see Fig. 5.6). The existence of this two dimensional jump has been employed by Evans [146] to explain planar ordering of voids in molybdenum. The activation energy for self-interstitial migration is low, ranging from only 0.01 eV for Pb to 0.3 eV for α -Fe [139].

5.4.2.2. Interstitial-solute interaction

Their large local lattice distortion causes self-interstitial dumbbells to interact strongly with other strain fields such as those associated with solute atoms and dislocations [140]. The interaction between interstitials and solute atoms is dependent on the impurity size; whether it is over- or under-sized with respect to the matrix lattice. In the proximity of a solute atom there are a number of possible configurations for the interstitial dumbbell to adopt. Those favoured will be where the displacement field of the solute atom fits best with that of the interstitial dumbbell. Configurations that are attractive for undersized solutes will be repulsive for oversized solutes and *vice versa*.

Undersized solute atoms are actually incorporated directly into the dumbbell, replacing the host dumbbell atoms to form a mixed dumbbell (interstitial-solute complex), illustrated in Fig. 5.7 [140]. The solute atom is displaced, to some extent, towards the octahedral site, causing a relaxation of the displaced lattice atoms towards their original sites as shown in Fig. 5.8 [72]. This relaxation in lattice distortion allows undersized solutes to form very stable complexes with interstitials. The complex binding energies, in general, increase with decreasing solute atom size [72]. Oversized solutes are not favoured to be incorporated into an interstitial dumbbell since they would cause even greater lattice distortion. Oversized solutes may remain substitutional and trap self-interstitial dumbbells on nearest neighbour sites. However, the binding energy for this kind of complex is low and the solute atom cannot undergo long range migration by means of the complex [143].

5.4.2.3. Interstitial-solute complex migration

The important consequence of complexes in terms of irradiation-induced segregation is not so much their formation, but their ability to undergo long range migration as a complex. Attentions have been focused on the situation in fcc metals and mechanisms in bcc metals are more speculative. The mechanisms that have been set forward for complex migration in bcc metals [143] are analogies of those for fcc metals. Hence it is helpful to deal with those first.

The equivalent jump to the self-interstitial jump (see Fig. 5.5) is shown in Fig. 5.9a [143]. It is obvious that in this scenario the mixed dumbbell is merely reoriented around the octahedral site: the solute atom stays in a cage centred on the octahedral site, the various configurations of which were shown in Fig. 5.6. Thus this process cannot lead to long range complex diffusion. If instead the mixed dumbbell purely rotates as shown in Fig. 5.9(b), the solute atom is transferred to a different octahedral cage. Combined with the previous cage motion (see Fig. 5.9(a)), long range migration of the mixed dumbbell can occur. A further possibility, as shown in Fig. 5.9(c), is the jump of the host atom to a self-interstitial dumbbell and the solute atom then returns to a substitutional site. As a result the mixed dumbbell has dissociated and no long range migration of the solute atom takes place directly. If, however, the resultant self-interstitial dumbbell further jumps round in a loop back to the solute atom, as indicated in Fig. 5.9(d), the mixed dumbbell is reformed but with the solute atom displaced to a different octahedral cage. consequently long range migration of the solute-interstitial complex is possible again.

Analogous motion of the $\langle 110 \rangle$ mixed dumbbell in bcc crystals is possible. In this case there are only four equivalent sites on a plane around the octahedral centre which give rise to $\langle 110 \rangle$ mixed dumbbells, illustrated in Fig. 5.10 [143]. Planar caging of the solute is possible (see Fig. 5.11(a)); as with the caging motion of the $\langle 100 \rangle$ mixed dumbbell (see Fig. 5.9 (a)) no long range solute migration occurs so long as the solute atom remains in the cage. A rotational jump with a 60° change of axis of the $\langle 110 \rangle$ mixed dumbbell is indicated in Fig. 5.11(b). Here the solute atom is transferred to a different planar cage; this jump combined with the caging motion hence brings about long range migration of solute atoms via an interstitial mechanism. Fig. 5.11(c) shows a further likely jump: a combined translation and rotation associated with the three dimensional jump of the self-interstitial dumbbell (see Fig. 5.5). it also corresponds closely to the octahedral-octahedral diffusional jump of solute atoms in an interstitial solid solution such as carbon in α -Fe. Finally a two dimensional interstitial migration of solute atoms derived from the planar migration of self-interstitials (see Fig. 5.5(c)) has been proposed [147] and is

illustrated in Fig. 5.11(d). In addition to these jump modes, dissociation of the mixed dumbbell to form a self-interstitial dumbbell configuration is possible, but this does not result in long range solute migration.

From the preceding discussion it is evident that point defects may interact strongly with solute atoms to form defect-solute complexes. If the bound complexes are able to migrate in preference to dissociation then a point defect flux will incorporate a linked solute flux, leading to solute segregation at point defect sinks such as grain boundaries and free surfaces. However, it will be seen in Chapter 6 that most of undersized solutes interact with interstitials more strongly than with vacancies. Moreover, as well known, the solute-interstitial complex migrates much more easily than the solute-vacancy complex. As a consequence, it can be expected that for undersized solutes which have strong interactions with interstitials the solute-interstitial complex should play a dominant role in radiation-induced solute segregation in dilute alloys.

Appendix 5.1
Figures for Chapter Five

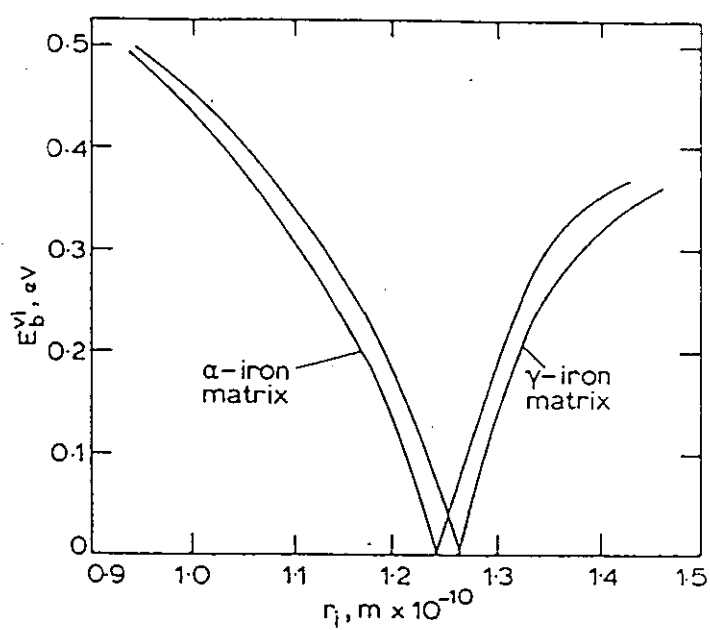
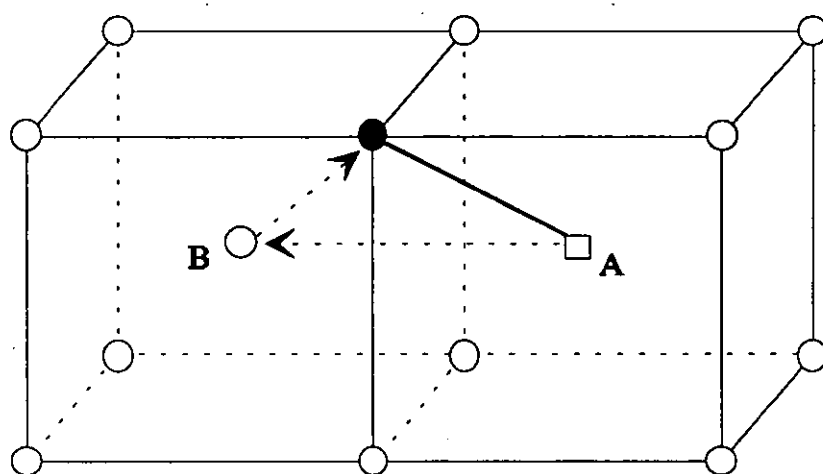


Fig. 5.1. The relationship between the vacancy-solute binding energy and the solute atom radius in iron, after Ref. [53].

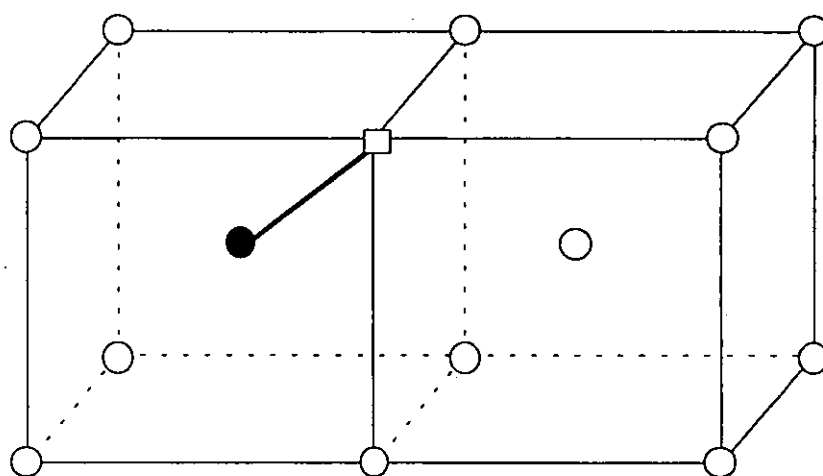


● : solute atom

○ : matrix atom

□ : vacancy

Fig. 5.2. Schematic diagram showing the migration process of vacancy-solute complexes in bcc crystals.



● : solute atom

○ : matrix atom

□ : vacancy

Fig. 5.3. Schematic diagram showing the position of the complex after jumps illustrated in Fig. 5.2.

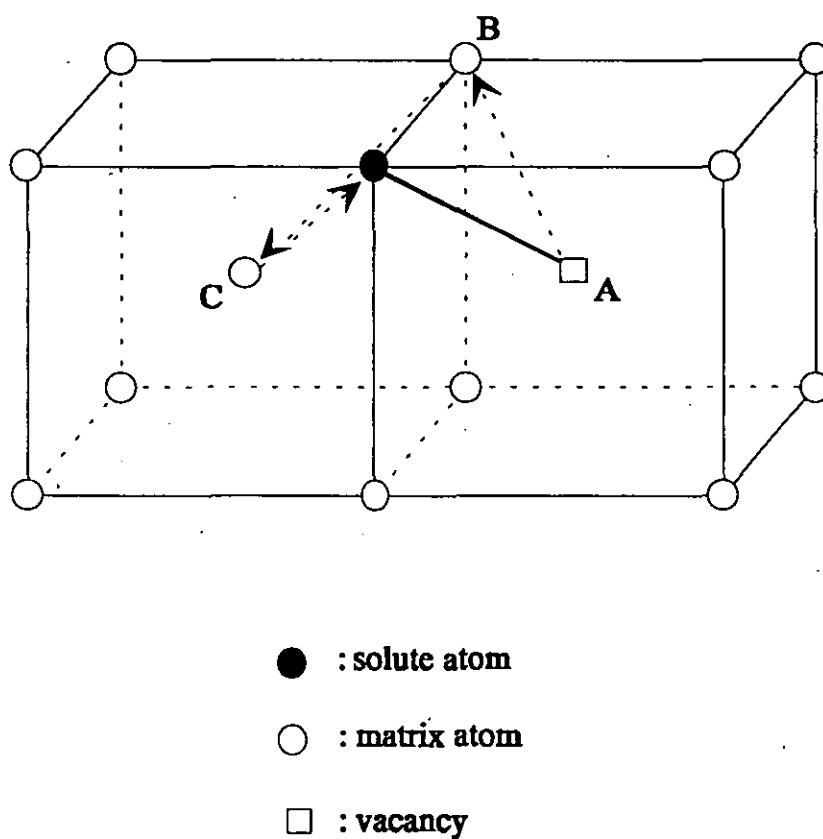


Fig. 5.4. Schematic diagram showing the migration process of vacancy-solute complexes in the dissociation mechanism in bcc crystals.

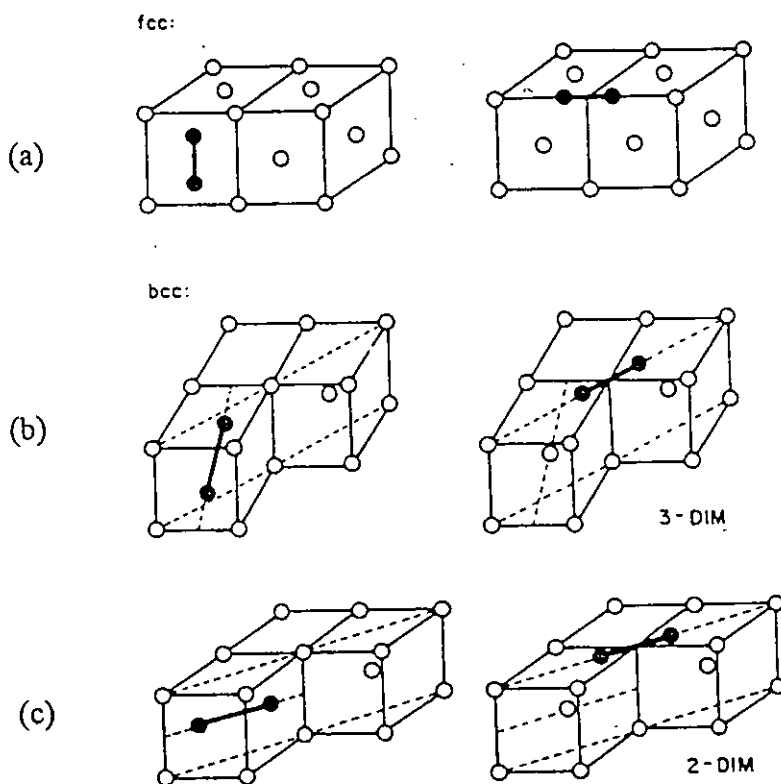


Fig. 5.5. (a) Migrational jump of the $[100]$ dumbbell in fcc crystals with simultaneous reorientation; (b) Migrational jump of the $[110]$ dumbbell in bcc crystals with a simultaneous reorientation of 60° ; (c) Migrational jump of the $[110]$ dumbbell in bcc crystals without reorientation (two dimensional migration), after Ref. [143].

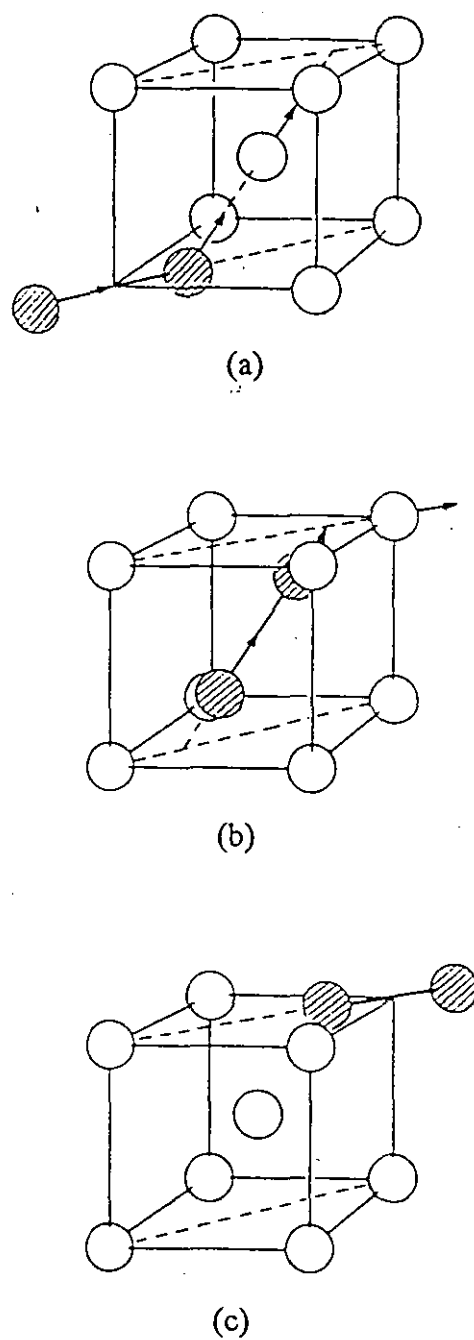


Fig. 5.6. The migrational jump process for two dimensional interstitial migration in bcc metals, showing (b) the intermediate $\langle 223 \rangle$ dumbbell, after Ref. [145].

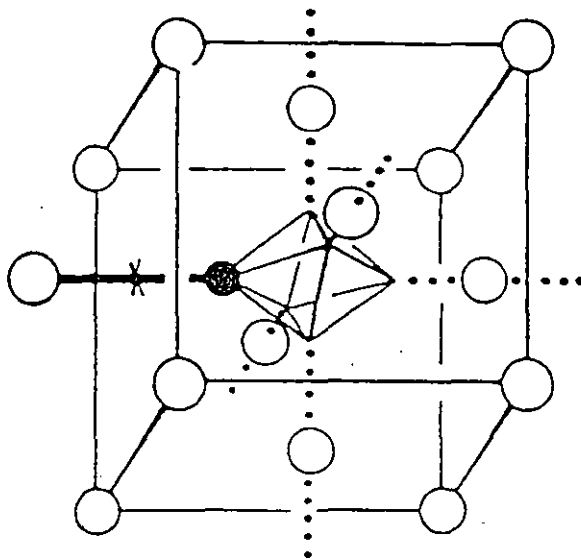


Fig. 5.7. The mixed dumbbell configuration of an undersized impurity-interstitial complex in the fcc lattice, showing as dotted lines the axes of a new mixed dumbbell which could be formed by motion of the impurity atom around the corners of the octahedral cage, after Ref. [140].

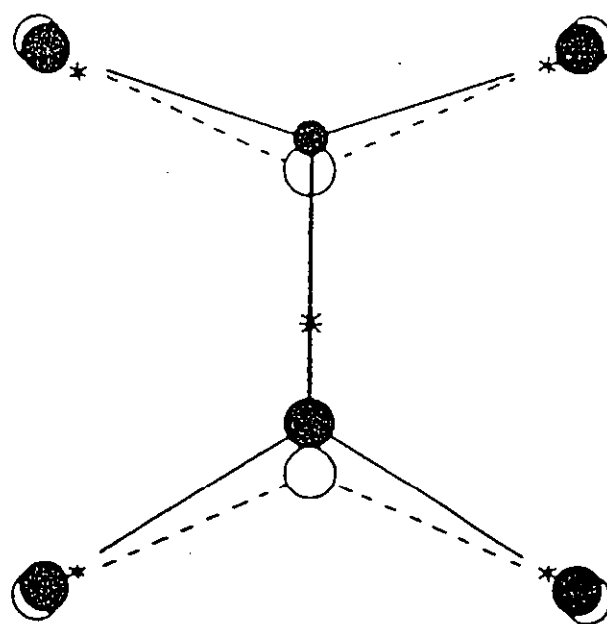


Fig. 5.8. Structure of the mixed dumbbell for an undersized solute atom in the fcc lattice, showing the relaxation of the atomic positions (•) towards the equilibrium positions (*) compared with the distorted positions of the self-interstitial (o), after Ref. [72].

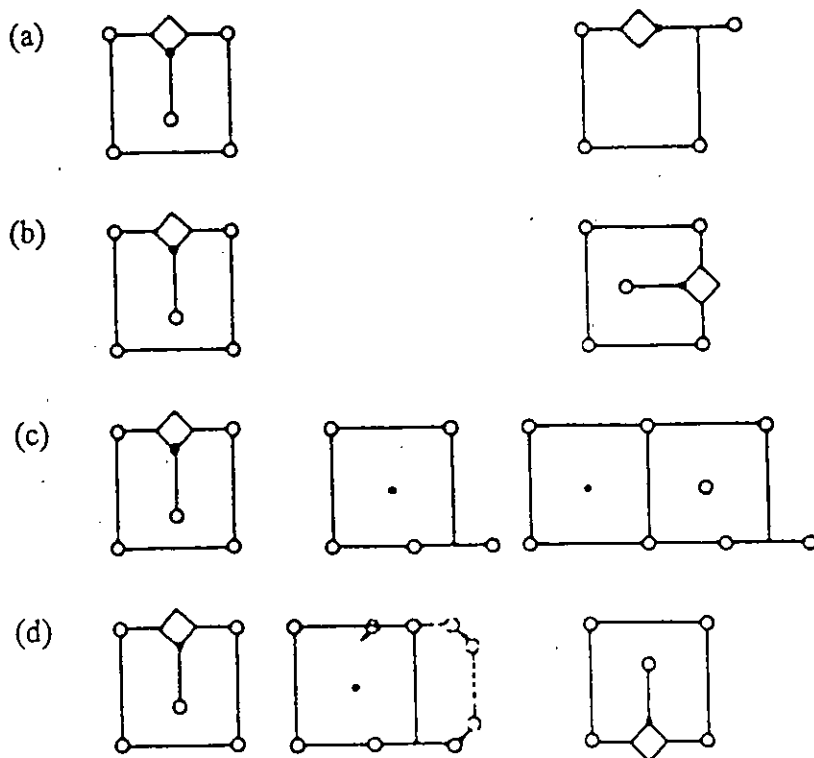


Fig. 5.9. Possible diffusional jumps of the undersized solute and matrix atoms incorporated in a [100] mixed dumbbell in fcc crystals - (a) caging, (b) rotation, (c) dissociation and (d) looping (•: solute atom, and o: matrix atom), after Ref. [143].

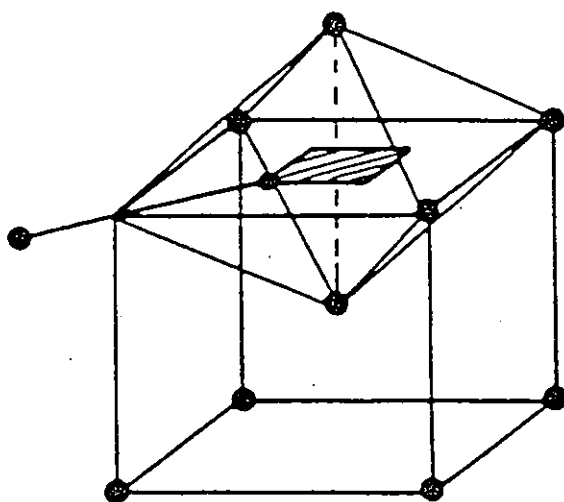


Fig. 5.10. Planar cage of the $[110]$ mixed dumbbell in the octahedral cell of the bcc lattice, after Ref. [143].

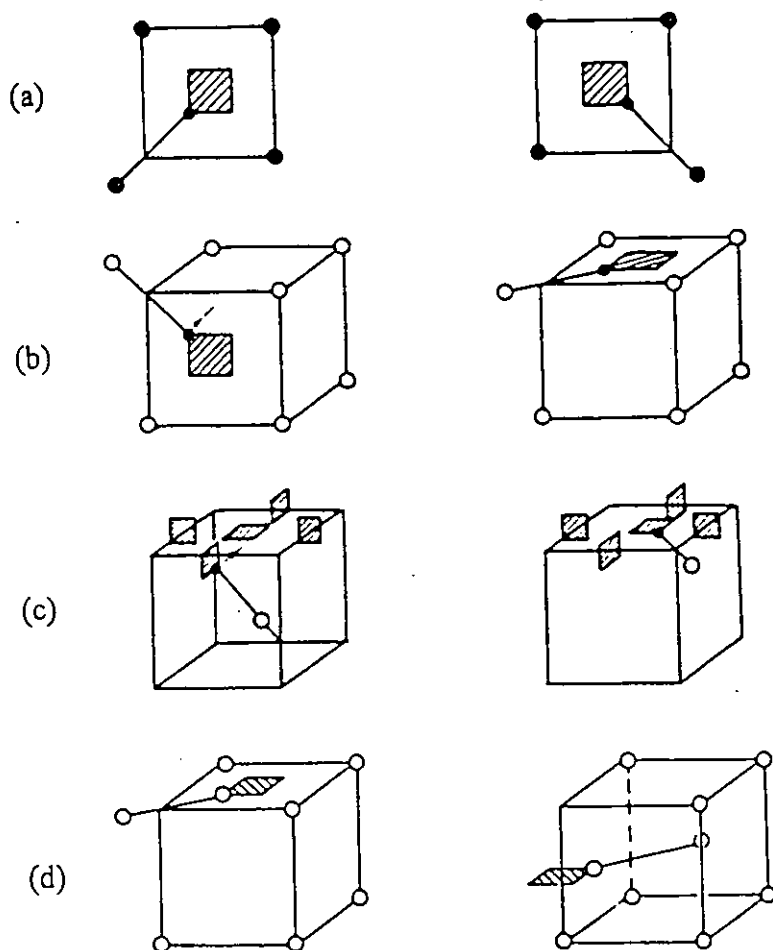


Fig. 5.11. Possible jump modes of the $[110]$ mixed dumbbell in the bcc lattice: (a) caging, (b) rotational jump, (c) octahedral-octahedral jump and (d) planar migration, after Ref. [143].

Chapter Six

Determination of Impurity-Point Defect Binding Energies in Alloys

As reviewed above, modelling of radiation-induced segregation or thermal non-equilibrium segregation requires data on the impurity-point defect binding energy. In general, these values are not available. A variety of electronic models used in attempting to quantify these binding energy values result in wide variations in the predicted results. For instance, using the electronic wave function model, Gupta [148] obtained that impurity-vacancy binding energies for Be, Si and Ge in nickel were -0.32, 0.73 and 0.55 eV, respectively, and impurity-interstitial binding energies, 0.58, 0.90 and 0.28 eV, respectively. In addition, the rate theory calculation employed to predict the radiation-induced segregation suggested that the Zn-vacancy and Zn-interstitial binding energies in silver [28], and Si-interstitial binding energy in nickel [8] were 0.05, 0.2, and 2.0 eV respectively. This large scatter of data suggests that more promising theoretical approaches need to be made.

Faulkner and Chapman [52,53] attempted to predict impurity-vacancy binding energies in some transition metal matrices, but their model requires slightly modifying for the evaluation of oversized impurity-vacancy binding energies. In this chapter, we have described such modifications and developed an initial approach to determining impurity-interstitial binding energies with some success on the basis of strain field arguments. Furthermore, the approach has been applied to predictions of point defect-solute binding energies in several important alloy matrices.

6.1. Impurity-vacancy binding energy

This quantity can be calculated by using the following equation [52,53]:

$$E_b^{iv} = E_f^i + E_f^v - E_f^{iv} \quad (6.1)$$

where E_f^i is the formation energy of the impurity;

E_f^v is the formation energy of the vacancy; and

E_f^{iv} is the formation energy of the impurity-vacancy complex.

For undersized impurities

$$E_f^i = E_s + \frac{8\pi}{3} \mu r_o (r_i - r_o)^2 \quad (6.2)$$

$$E_f^v = 4\pi r_v^2 S + \frac{8\pi}{3} \mu r_o (r_o - r_v)^2 \quad (6.3)$$

$$E_f^{iv} = E_f^{ii} - E_s + 4\pi r_c^2 S + \frac{8\pi}{3} \mu r_i (r_i - r_c)^2 \quad (6.4)$$

$$E_f^{ii} = 2E_s + \frac{14\pi}{3} \mu r_o (r_i - r_o)^2 \quad (6.5)$$

where E_f^{ii} is the formation energy of the di-impurity complex;

E_s is the matrix/impurity interfacial energy associated with an impurity atom placed on a matrix atom site;

S is the surface energy per unit area of the matrix;

μ is the shear modulus of the matrix;

r_o is the matrix atom radius;

r_i is the impurity atom radius; and

$$r_v = \frac{r_o}{1 + \frac{3S}{2\mu r_o}} \quad (6.6)$$

and

$$r_c = \frac{r_i}{1 + \frac{3S}{2\mu r_i}} \quad (6.7)$$

Consequently, the undersized impurity-vacancy binding energy is given by

$$\begin{aligned} E_b^{iv} &= E_f^i + E_f^v - E_f^{iv} \\ &= \frac{2}{3} \pi \mu r_o [4(r_v - r_o)^2 - 3(r_i - r_o)^2] \\ &\quad - \frac{8}{3} \pi \mu r_i (r_c - r_i)^2 + 4\pi S (r_v^2 - r_c^2) \end{aligned} \quad (6.8)$$

For oversized impurities, the modelling of the impurity-vacancy complex is not as easy as that of the undersized impurity-vacancy complex because when the complex is formed by removing an impurity atom from a di-impurity complex, the elastic distortion of the lattice caused by the impurity will be relaxed (see Refs. [52,53]). Therefore, Equation (6.4) has to be changed. In this case, the vacancy size is

effectively reduced. In the light of Faulkner's analysis [52,53], the extent of the reduction may be estimated by assuming that the radius of the hole has been reduced by an amount equal to the increased size of the retained impurity atom compared with that of the matrix atom, leading to a hole size r_p , where $r_p = 2r_o - r_i$, and then further shrinking to r_{cl} (see Fig. 6.1), leading to the negative distortion. Hence the following elastic strain energy may approximately be removed by the relaxing process, which was not taken into account in the work of Faulkner [52,53]:

$$E_R = \frac{8\pi}{3} \mu r_o (r_o - r_i)^2 \quad (6.9)$$

The increased elastic strain energy by shrinking of the hole may be given by

$$E_H = \frac{8\pi}{3} \mu r_p (r_p - r_{cl})^2 \quad (6.10)$$

where

$$r_{cl} = \frac{r_p}{1 + \frac{3S}{2\mu r_p}} \quad (6.11)$$

Consequently, the formation energy of the oversized impurity-vacancy complex is then given by

$$E_f^{iv} = E_f^i - E_s - E_R + E_H + 4\pi r_{cl}^2 S \quad (6.12)$$

and in turn the oversized impurity-vacancy binding energy is given by

$$\begin{aligned} E_b^{iv} &= E_f^i + E_f^v - E_f^{iv} \\ &= \pi\mu \left[\frac{2}{3} r_o (r_o - r_i)^2 + \frac{8}{3} r_o (r_o - r_v)^2 - \frac{8}{3} r_p (r_p - r_{cl})^2 \right] \\ &\quad + 4\pi S (r_v^2 - r_{cl}^2). \end{aligned} \quad (6.13)$$

6.2. Impurity-interstitial binding energy

Many damage rate studies [149,150] of dilute alloys have shown that interstitials can be strongly trapped by substitutional impurities. Some of these traps in aluminium have been confirmed by Swanson et al. [151] as mixed [100] dumbbells

consisting of an impurity atom and a matrix atom. The mixed dumbbell (impurity-interstitial complex) binding energy can be given by [72]

$$E_b^{ii} = E_f^I + E_f^i - E_f^{ii} \quad (6.14)$$

where

E_f^I is the interstitial atom (self-interstitial dumbbell) formation energy;

E_f^i is the impurity atom formation energy; and

E_f^{ii} is the impurity-interstitial complex (mixed dumbbell) formation energy.

It is well known that in metal crystals the self-interstitial atoms (SIA) exist in the form of dumbbells. It has been confirmed, as reviewed by Dederichs et al. [72], Young [139] and Schilling [140], that the [110] interstitial dumbbell is the stable configuration for bcc crystals (see Fig. 6.2) and the [100] for fcc crystals (Fig. 6.3). Two matrix atoms are assumed to fill the interstitials on either side of the vacant substitutional site. In terms of the work of Faulkner and Chapman [52,53], the interstitial (dumbbell) formation energy, E_f^I , may approximately be given by

$$E_f^I = \frac{14\pi}{3} \mu r_k (r_o - r_k)^2 + 8\pi r_o^2 S_o \quad (6.15)$$

where

r_o is the matrix atom radius;

r_k is the hole radius before the dumbbell formation;

S_o is the energy per unit area of the interface between a matrix atom and a perfect lattice; and

μ is the shear modulus of the matrix.

It is assumed here that S_o is the coherent twin boundary energy. The value of S_o for a coherent twin boundary is about 0.019 Jm^{-2} for Fe - Cr - Ni alloys, and about 0.043 Jm^{-2} for nickel [152].

Replacing a matrix atom in the self-interstitial dumbbell by an impurity atom creates an impurity-interstitial complex (mixed dumbbell, see Figs. 6.4 and 6.5). The impurity-interstitial formation energy is given by [52,53]

$$E_f^{ii} = E_f^I - \frac{8\pi}{3} \mu r_k (r_o - r_k)^2 - 4\pi r_o^2 S_o + \frac{8\pi}{3} \mu r_k (r_i - r_k)^2 + E_s \quad (6.16)$$

Thus the impurity-interstitial binding energy may be given by

$$\begin{aligned}
 E_b^{ii} &= E_f^I + E_f^I - E_f^{II} \\
 &= \frac{8\pi}{3} \mu [r_o(r_i - r_o)^2 + r_k(r_o - r_k)^2 \\
 &\quad - r_k(r_i - r_k)^2] + 4\pi r_o^2 S_o
 \end{aligned} \tag{6.17}$$

It is usual that matrix atoms in the self-interstitial dumbbell occupy positions of approximately (1/4,1/4,1/4) for bcc crystals (See Fig. 6.6) and positions of approximately (1/4,0,0) for fcc crystals (see Fig. 6.7). As a result, the hole radius before the dumbbell formation, r_k , may be approximately given by

for bcc crystals

$$\begin{aligned}
 r_k &= l - r_o \\
 &= \sqrt{\frac{3a^2}{8}} - \frac{\sqrt{3}a^2}{4}
 \end{aligned} \tag{6.18}$$

for fcc crystals

$$\begin{aligned}
 r_k &= l - r_o \\
 &= \frac{\sqrt{5}a^2}{4} - \frac{\sqrt{2}a^2}{4}
 \end{aligned} \tag{6.19}$$

where

l is the distance between the hole centre and the body-centred matrix atom for bcc crystals (see Fig. 6.6) or that between the hole centre and the face-centred matrix atom for fcc crystals (see Fig. 6.7);

r_o is the matrix atom radius; and

a is the lattice constant and is 0.286, 0.359, and 0.352 nm for ferritic steel matrices [153], austenitic stainless steel matrices [153,154], and nickel alloy matrices [153], respectively.

From the above data, r_k is acquired to be 0.0512, 0.0738, and 0.0723 nm for ferritic steel, austenitic stainless steel and nickel alloy matrices, respectively.

6.3. Results

An initial approach to determining impurity-interstitial binding energies has been established on the basis of strain field arguments and the earlier work of Faulkner

and Chapman [52,53] has been slightly modified for the evaluation of oversized impurity-vacancy binding energies. Predicted values of binding energies for ferritic steel, austenitic stainless steel and nickel alloy matrices are listed in Table 6.1 which shows that (i) the binding energies of the undersized impurity-interstitial complex, the undersized and oversized impurity-vacancy complexes increase with increasing difference between the impurity and matrix atom sizes; (ii) the binding energies of the oversized impurity-interstitial complexes decrease with increasing the difference between the impurity and matrix atom sizes and excepting nickel in α -Fe and chromium in nickel, which are marginally oversized impurities, oversized impurity elements have negative binding energies with the interstitial; (iii) the binding energy of the oversized impurity-vacancy complex is greater than that of the undersized impurity-vacancy complex as the size difference between the oversized impurity and matrix atoms is the same as that between the undersized impurity and matrix atoms; and (iv) the interaction of the undersized impurity and the interstitial is stronger than that of it and the vacancy. It is seen that for a ferritic steel matrix the phosphorus-interstitial and -vacancy binding energies are 0.57 and 0.36 eV, respectively. The above predictions are visually shown in Figs. 6.8-6.10.

6.4. Discussion

In this work, an initial approach to determining impurity-interstitial binding energies has been developed on the basis of strain field arguments. Predicted values of binding energies for several alloy matrices are shown in Table 6.1 and Figs. 6.8-6.10 which indicate that (i) the binding energies of the undersized impurity-interstitial complex, the undersized impurity- and oversized impurity-vacancy complexes increase with increasing the difference between the impurity and matrix atom sizes; (ii) the binding energies of the oversized impurity-interstitial complexes decrease with increasing the difference between the impurity and matrix atom sizes and excepting nickel that has very small difference in size with the matrix atom, other oversized impurity elements have negative binding energies with the interstitial; (iii) the binding energy of the oversized impurity-vacancy complex is greater than that of the undersized impurity-vacancy complex as the size difference between the oversized impurity and matrix atoms is the same as that between the undersized impurity and matrix atoms; and (iv) the interaction of the undersized impurity and the interstitial is stronger than that of it and the vacancy.

The predicted results present in this work are generally reasonable. This is because any free vacancy and impurity atom both lead to the distortion of matrix lattice, negative for the vacancy and the undersized impurity, and positive for the oversized

impurity. When the impurity-vacancy complex forms, the distortion energy, in general, will decrease. The reduction of the distortion energy is relatively small for the undersized impurity-vacancy complex because the distortion sign (negative distortion) caused by free vacancies is the same as that caused by free impurities. However, for oversized impurities, since the distortion caused by the oversized impurity is positive while that caused by the vacancy is negative, the distortion caused by the impurity will get partially relaxed, which causes the negative distortion caused by the vacancy to be reduced when this impurity forms a complex with a vacancy so that the binding energy of the oversized impurity-vacancy complex is greater than that of the undersized impurity-vacancy complex if the size difference between the oversized impurity and the matrix atom is the same as that between the undersized impurity and the matrix atom.

Faulkner and Chapman [52,53] have attempted to predict impurity-vacancy binding energies in some transition metal matrices, but their model needs to be slightly modified for more accurate calculation of oversized impurity-vacancy binding energies. This has been made in this work. For example, after modifying the Mo-vacancy binding energy in the ferritic steel matrix is 0.38 eV while the value is 0.31 eV before modifying.

It is interesting to note that except for nickel in the ferritic steel matrix, which is a marginally oversized impurity, oversized impurity elements have negative binding energies with the interstitial and moreover the nickel-interstitial binding energy in the ferritic steel matrix is very small (0.0072 eV) although it is positive. This indicates that in the irradiated material, there are few oversized impurity-interstitial complexes, which, as well known, is reasonable.

The results obtained in this work are similar to those predicted by Dederichs et al. [72]. Dederichs et al. established a method of calculating the impurity-interstitial binding energy on the basis of the assumption that the size of the impurity is the decisive quantity for the formation of impurity-interstitial centres. In their model, the impurity-interstitial binding energy is given by

$$E_b^{ii} = - \Delta E$$

where ΔE is the interaction energy for the complex configuration.

Using the shifted potential model they calculated the impurity-interstitial binding energies for the copper matrix. The results give binding only for $r_i < 0$ (r_i = impurity atom radius - matrix atom radius), i.e. for undersized impurities. Thus for an undersized impurity ($r_i < 0$), a large amount of energy can be gained by the formation of an impurity-interstitial complex so that $E_b^{ii} > 0$ ($\Delta E < 0$). For an oversized impurity ($r_i > 0$), the equivalent amount of energy is lost so that $\Delta E > 0$ and the complex is unstable. Therefore, their model predicts that impurity-interstitial complexes should be formed only for undersized impurities. In addition, their model also predicts that (i) the binding energies of the undersized impurity-interstitial complexes increase with increasing the difference between the impurity and matrix atom sizes and are positive; (ii) the binding energies of the oversized impurity-interstitial complexes decrease with increasing the difference between the impurity and matrix atom sizes and are negative. Clearly, these are consistent with the results presented in this work (see Figs. 6.8-6.10).

It may be considered that the elastic strain energy has been involved in the above shifted potential model because the larger the difference between the impurity and matrix atom sizes, the larger is the absolute value of the interaction energy ΔE . However the interfacial energy has not been involved in this potential model. In the present work, we have taken into account not only the elastic strain energy, but also the interfacial energy. As a result, it may be thought that the model presented in this work is more comprehensive.

Furthermore, some experimental phenomena on the irradiation-induced segregation may be relatively satisfactorily explained with the aid of the present predictions of the impurity-point defect binding energies. As well-known, the undersized impurity-interstitial complex (such as phosphorus-interstitial complex and silicon-interstitial complex) fluxes towards sinks such as grain boundaries and free surfaces are dominant during irradiation. This is because, as reviewed above, (a) the migration energy of impurity-vacancy complexes is larger than that of impurity-interstitial complexes; and (b) the interaction between the undersized impurity and the interstitial is stronger than that between it and the vacancy. Since the diffusion flux of species to the sink depends on the concentration gradient between the sink and the zones remote from it, and the diffusion rate of species in the matrix, the fluxes of undersized impurity-interstitial complexes with relatively high binding energies towards the sink are dominant. The effect of vacancies and impurity-vacancy complexes is small during irradiation so that the undersized impurities segregate to sinks. For oversized impurities, as discussed in Ref. [97], if impurity-vacancy

binding energies are nearly zero or relatively small, impurity depletion near sinks may be observed. This type of inverse segregation takes place because for small impurity-vacancy binding energies, the concentration of impurity-vacancy complexes is low and coupling between the impurity atom and the vacancy is quite weak. When vacancies flow to the sink, impurity atoms migrate in the opposite direction away from the sink, inducing an impurity depletion near the sink until the impurity concentration gradients are sufficiently steep to balance the forward and backward fluxes. It should be noted that for polynary alloys the segregation behaviour of different impurities and alloying elements is also dependent on their relative diffusion rates. For example, it is often found in irradiated stainless steels that grain boundary chromium depletion and nickel enrichment occur because the diffusion rate of chromium is faster than that of nickel. The impurity depletion in the vicinity of sinks is more pronounced as the impurity-interstitial binding energy is very low or negative. This is because, in addition to the vacancy flow effect that causes back-diffusion of impurity atoms, the free interstitials preferentially transport matrix atoms to the sink. If impurity-vacancy binding energies are very high, impurity-vacancy complex fluxes towards sinks become significant and then impurity enrichments adjacent to sinks might be found. As a consequence, it may be predicted that some oversized impurities, which interact quite strongly with the vacancy, segregate to sinks during irradiation. It has been shown from the work of Neklyudov and Voyevodin [157] that there exists grain boundary segregation of titanium in a neutron-irradiated austenitic stainless steel. However, for many oversized impurities, the interaction between the impurity and the vacancy is not strong enough to lead to the impurity enrichment. As discussed above, the diffusion flux of species to the sink is determined by the concentration gradient between the sink and the regions beyond it, and the diffusion rate of species in the matrix. Since the migration of free vacancies is more easy than that of impurity-vacancy complexes, only as the impurity-vacancy binding energy is high enough, may the diffusion flux of impurity-vacancy complexes to the sink be larger than that of impurity atoms away from it, caused by the impurity atom-vacancy exchange mechanism. In addition, another major reason for the depletion of many oversized impurities in the vicinity of sinks is that free interstitials preferentially transport matrix atoms towards sinks so that the ratio of the number of solvents to that of solutes is enhanced near sinks

6.5. Summary

Modelling of irradiation-induced segregation or thermal non-equilibrium segregation needs data on the impurity-point defect binding energy. These values

are generally unavailable. Faulkner and Chapman [52,53] have been in a good position for predicting impurity-vacancy binding energies, but their model requires to be slightly modified for more accurate calculation of oversized impurity-vacancy binding energies. In this work, an approach to calculating impurity-interstitial binding energies was established with some success on the basis of strain field arguments. The earlier work of Faulkner and Chapman was slightly modified for the evaluation of oversized impurity-vacancy binding energies. The method was applied to predictions of various impurity-point defect binding energies in several transition metal matrices. With the help of these predictions, some experimental results on irradiation-induced segregation were reasonably satisfactorily interpreted.

Appendix 6.1
Tables for Chapter Six

Table 1. Data on impurity-point defect binding energies for various impurities in several alloy matrices

Element	r_i (Å)	E_b^{iv} (eV)	E_b^{ii} (eV)	E_b^{iv} (eV)	E_b^{ii} (eV)	E_b^{iv} (eV)	E_b^{ii} (eV)
		in A	in A	in B	in B	in C	in C
S	1.04	0.421	0.78	0.46	0.90	0.39	0.77
P	1.09	0.36	0.57	0.41	0.69	0.33	0.58
Si	1.17	0.20	0.26	0.27	0.38	0.19	0.30
As	1.21	0.094	0.12	0.17	0.23	0.10	0.16
Ni	1.246	0.016	0.0072	0.073	0.10		
Cr	1.28	0.12	-0.096	0.036	-0.012	0.10	-0.049
Mo	1.36	0.38	-0.31	0.30	-0.26	0.33	-0.27
W	1.37	0.41	-0.33	0.33	-0.29	0.36	-0.29
Sb	1.41	0.54	-0.43	0.46	-0.40	0.48	-0.39
Sn	1.41	0.54	-0.43	0.46	-0.40	0.48	-0.39
Nb	1.43	0.60	-0.46	0.52	-0.45	0.54	-0.44
Ti	1.47	0.72	-0.54	0.65	-0.55	0.66	-0.52

A: the ferritic steel matrix ($r_o = 0.1241$ nm [153]); B: the austenitic steel matrix ($r_o = 0.1269$ nm [153,154]); and C: the nickel alloy matrix ($r_o = 0.1246$ nm [153]).

S: ~ 1.9 and ~ 1.73 Jm $^{-2}$ for steels and nickel alloys, respectively [155]; μ : $\sim 8.1 \times 10^4$ and $\sim 7.7 \times 10^4$ MNm $^{-2}$ for steels and nickel alloys, respectively [156].

Appendix 6.2
Figures for Chapter Six

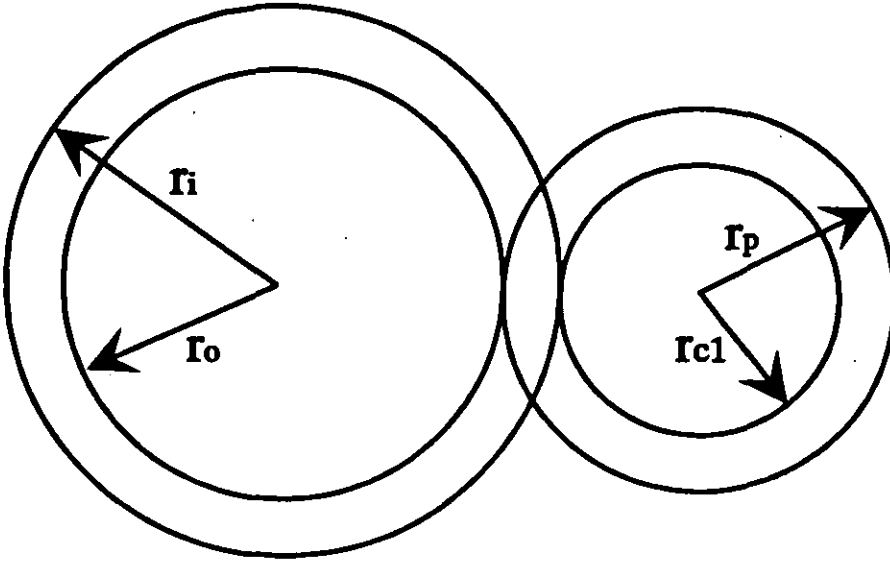


Fig. 6.1. The hole size for oversized impurity-vacancy complexes.

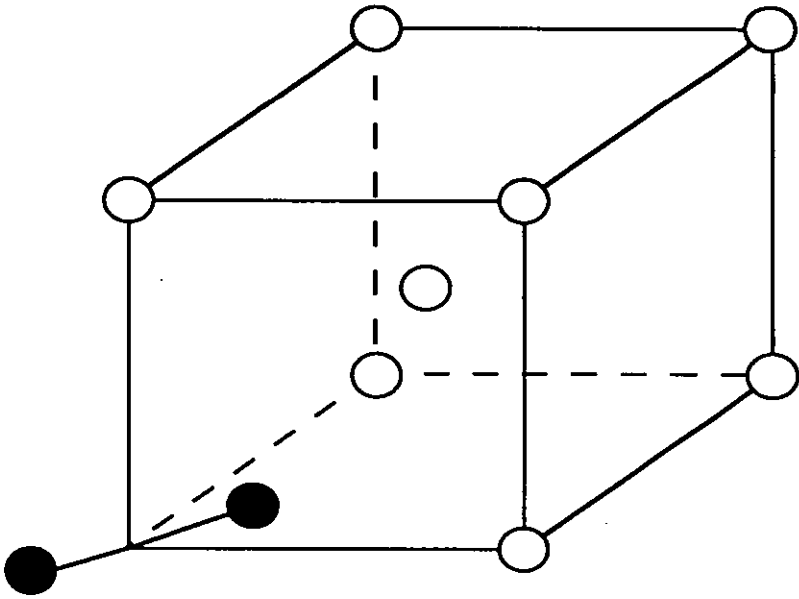


Fig. 6.2. The $[110]$ interstitial dumbbell in bcc crystals.

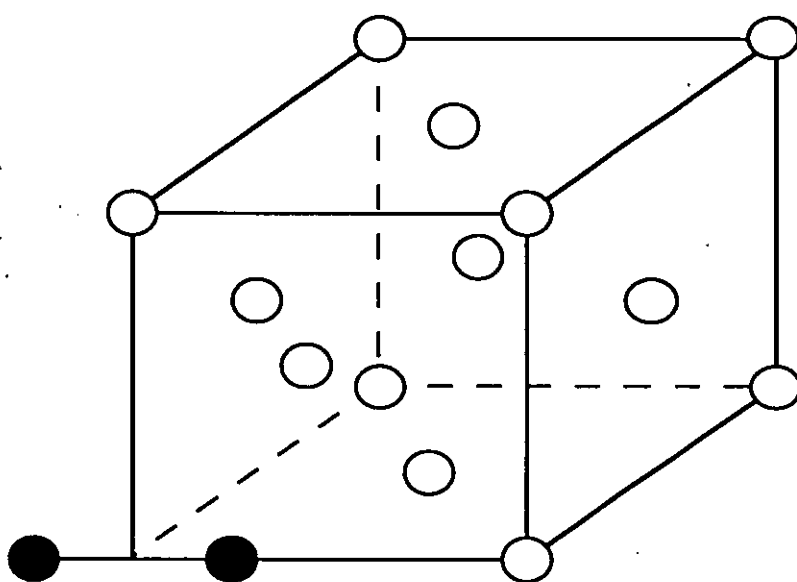


Fig. 6.3. The $[100]$ interstitial dumbbell in fcc crystals.

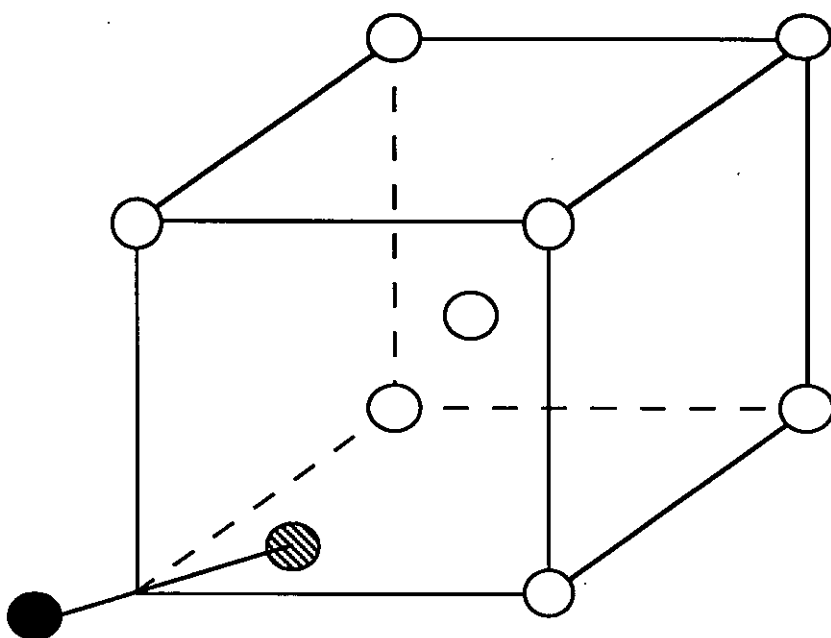


Fig. 6.4. The impurity-interstitial complex (mixed dumbbell) in bcc crystals.

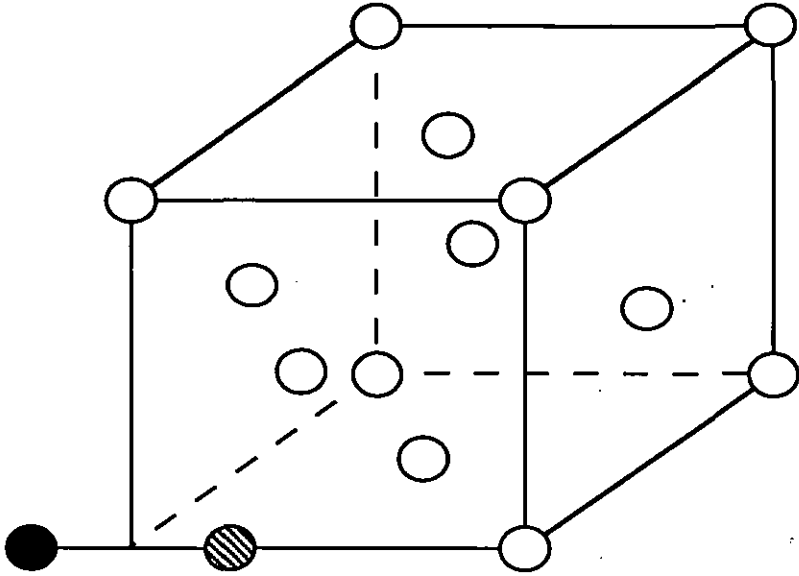


Fig. 6.5. The impurity-interstitial complex (mixed dumbbell) in fcc crystals.

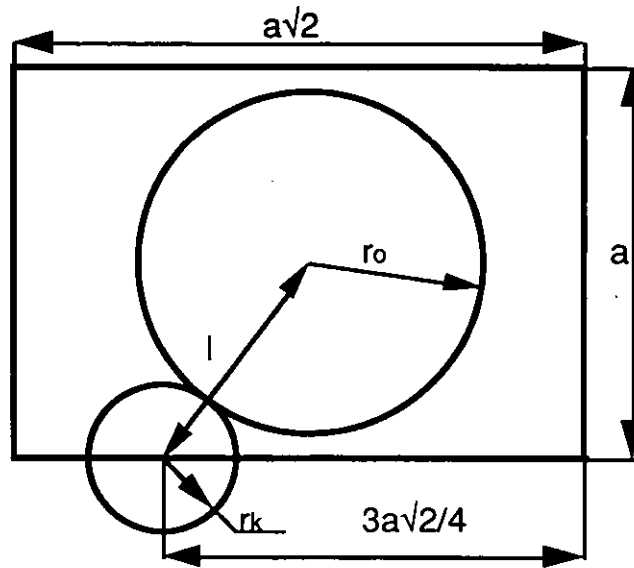


Fig. 6.6. The (110) section of Fig. 2 showing the hole radius r_k before the interstitial dumbbell formation in bcc crystals.

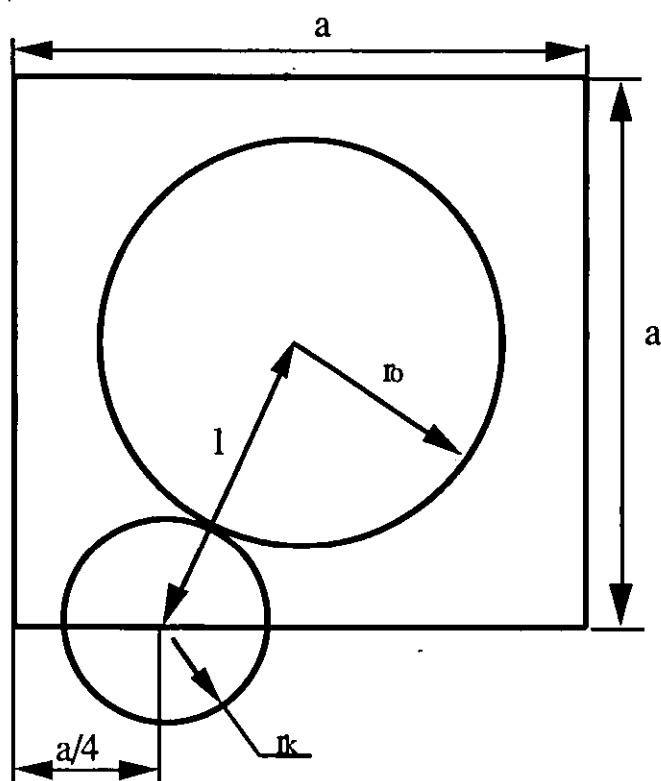


Fig. 6.7. The (100) section of Fig. 3 showing the hole radius r_k before the interstitial dumbbell formation in fcc crystals.

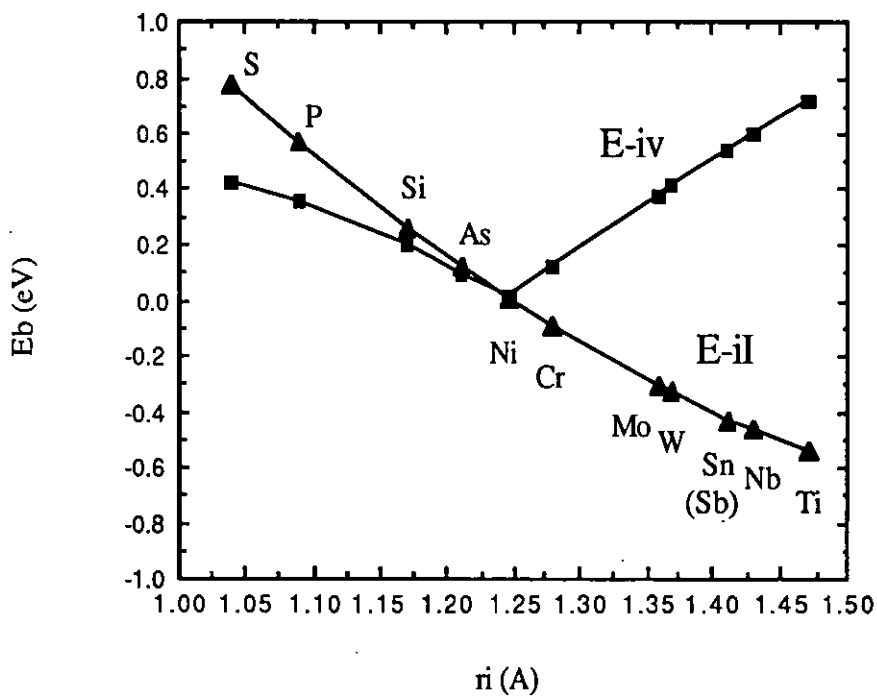


Fig. 6.8. The impurity-point defect binding energies as a function of impurity atom radius in the ferritic steel matrix.

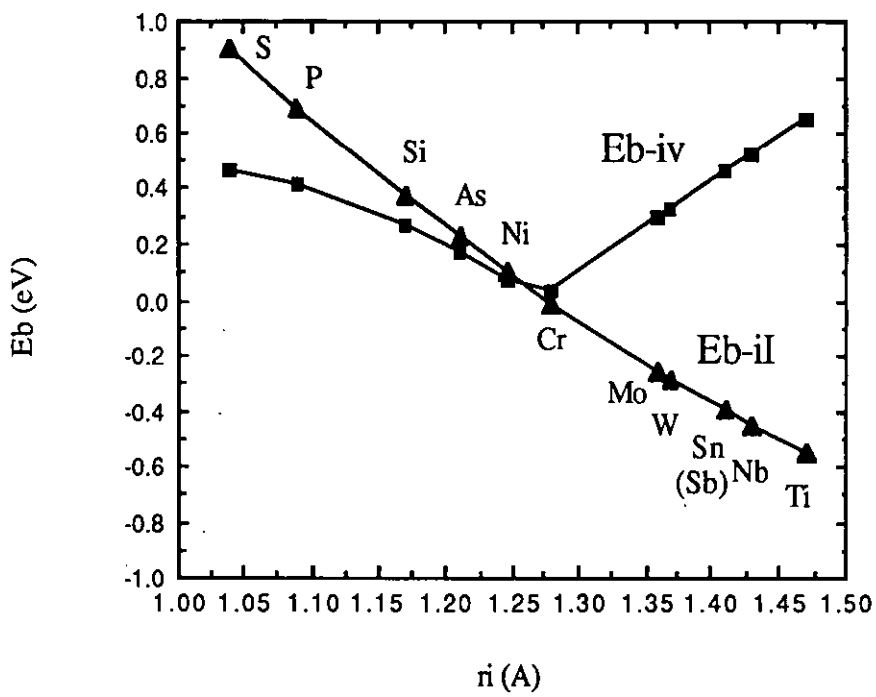


Fig. 6.9. The impurity-point defect binding energies as a function of impurity atom radius in the austenitic stainless steel matrix.

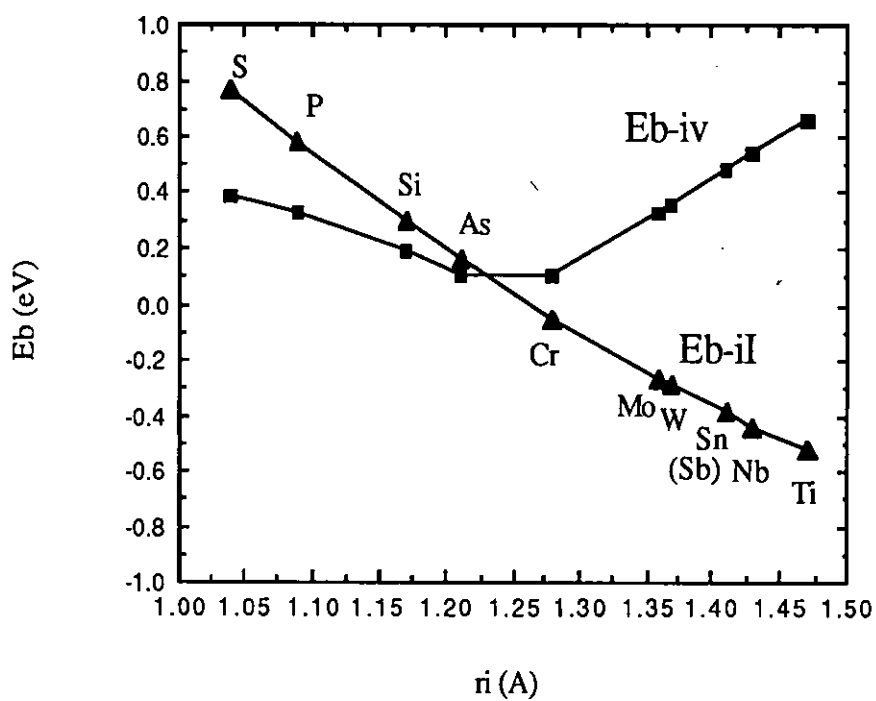


Fig. 6.10. The impurity-point defect binding energies as a function of impurity atom radius in the nickel alloy matrix.

Chapter Seven

Modelling of Radiation-Induced Grain Boundary Segregation

During the past twenty years, a large number of experimental and theoretical studies have been directed towards a basic understanding of radiation-induced segregation (RIS) in alloys. The segregation of alloying elements to or away from external surfaces, grain boundaries, dislocations and voids has been recognised as a common effect in a wide variety of alloys after irradiation with neutrons or charged-particles. Since the alloy composition in the vicinity of internal sinks and external surfaces is altered, this radiation-induced segregation will affect a quantity of bulk and surface properties which are sensitive to the alloy composition, for example, mechanical strength, void swelling, phase stability and corrosion-resistance. Therefore, a good understanding of radiation-induced segregation is of extreme importance to components and structures operating in this environment.

In this chapter, a radiation-induced grain boundary segregation model has been developed for dilute alloys. Furthermore, in the treatment of segregation during irradiation, thermal equilibrium segregation should be taken into consideration. For such reason, the radiation-induced segregation model has been combined with Mclean's equilibrium segregation model [51]. In recognition of strong thermal equilibrium segregation of phosphorus to grain boundaries [158], this model has been applied to predictions of phosphorus grain boundary segregation in irradiated α -Fe.

It should be recognised here that thermal non-equilibrium segregation may take place during pre-irradiation heat-treatments. This will be detailed in the future work and not taken into consideration in the present work.

7.1. Radiation-induced segregation (RIS)

For undersized solutes that have strong interactions with interstitials, the fluxes of solute-interstitial complexes to sinks such as grain boundaries, as well known [28-30, 70-72], are dominant during irradiation. In this work, we will only consider this case. The segregation mechanism depends on the formation of sufficient quantities of interstitial-solute complexes. Solute atoms, interstitials and their complexes are in equilibrium with each other at a given temperature. Irradiation makes the interstitial concentration exceed the thermal equilibrium concentration in the matrix. However, at sinks such as grain boundaries and free surfaces the interstitial concentration

approaches the thermal equilibrium concentration. The decrease in interstitial concentration results in the dissociation of the complexes into interstitials and solute atoms. This in turn leads to a decrease in complex concentration in the proximity of grain boundaries. Meanwhile, in regions away from the grain boundary, the steady state concentration of the complexes always remains. As a result, a complex concentration gradient appears between the grain boundary and the grain centre. The gradient of complex concentration drives complexes to migrate towards the grain boundary from regions remote from it. This migration of complexes causes excess solute atoms to concentrate in the vicinity of grain boundaries. It is obvious that the larger the supersaturation level of interstitials induced by irradiation, the larger the segregation level of solute atoms at the boundary.

The basic model of Faulkner et al. [38] is utilised to describe the process. This model originally predicted the maximum magnitude of segregation expected in dilute alloys on the basis of a thermodynamic argument using the equilibrium concentration of interstitials expected at grain boundaries ratioed to the quasi-equilibrium concentration expected within grains during neutron irradiation. The maximum segregation magnitude during irradiation, C_{br}^m , is given by [38]

$$C_{br}^m = C_s \frac{E_b^{ii}}{E_f^I} \left[1 + \frac{BG}{A_i D_i k_{di}^2} \exp\left(\frac{E_f^I}{kT}\right) \right] \quad (7.1)$$

where C_s is the solute concentration in the matrix;

E_b^{ii} is the solute-interstitial binding energy;

E_f^I is the interstitial formation energy;

D_i is the interstitial diffusion coefficient in the matrix;

A_i is a constant showing the vibrational entropy of atoms around the interstitial;

G is the point defect production rate or dose rate;

k is Boltzmann's constant;

T is the absolute temperature;

B is the dose rate correction factor, i.e. the fraction of freely migrating defects; and

k_{di}^2 is the grain interior sink strength for the interstitial, given by [38]

$$k_{di}^2 = (Z_i \rho)^{\frac{1}{2}} \left[\frac{6}{R} + (Z_i \rho)^{\frac{1}{2}} \right] \quad (7.2)$$

where R is the grain size and Z_l is the bias parameter defining the preferential interaction between interstitials and dislocations compared with that between vacancies and dislocations.

The introduction of the dose rate correction factor, B , which was not accommodated in the basic model [38], is based on the following reasons. As discussed in Ref. [159], an additional feature which acts to reduce the absolute magnitude of the solute segregation arises because only a small proportion of point defects created by irradiation may undergo long range migration. Recent studies by Rehn [160] and Naundorf et al [161] have shown that the ratio of freely migrating point defects produced by charged particle or neutron irradiation to those initially created amounts is only about 1%. More recent studies [162] indicate that the value of B is in the range of 0.01-0.05. Therefore, it is necessary to assume that the effective dose rate is only a very small part of the calculated value, i.e., a dose rate correction factor, B , should be applied to the term containing the dose rate. Moreover, as discussed in Ref. [163], long-range recombination of migrating vacancies and interstitials should be taken into account for high dose rate irradiation such as ion or electron irradiation but it may be neglected for low dose rate irradiation such as neutron irradiation. Therefore, this effect may be negligible in the case of this work.

It is evident that the maximum segregation concentration, C_b^m , is only dependent on the irradiation temperature and is independent of the irradiation time. Consequently, Equation (7.1) is an important quasi-thermodynamic equation describing the non-equilibrium grain boundary segregation during irradiation. The interstitial concentration in the matrix at the steady state of irradiation, C_i , may be approximately given by [38]

$$C_i = A_i \exp\left(\frac{-E_f'}{kT}\right) + \frac{BG}{D_l k_{dl}^2} \quad (7.3)$$

This interstitial concentration is invariant except in regions very close to the boundary. Modelling the point defect distribution in the proximity of grain boundaries is difficult. For this reason, several studies have assumed that the defect concentration is uniform up to the boundary [46,154]. In this scenario, the complex concentration may be approximately given by [38]

$$C_c = k_c C_i C_i(x, t) \exp\left(\frac{E_b^H}{kT}\right) \quad (7.4)$$

where k_c is a geometrical constant and $C_i(x, t)$ is the solute concentration.

Consequently, in consideration of very small thickness of the grain boundary compared with the grain size, the segregation process may be thought of as a linear flow in a semi-infinite mass feeding the boundary. In the light of Equation (7.4), the relevant diffusion equation describing this process may be given by

$$D_c \frac{\partial^2 C_i(x, t)}{\partial x^2} = \frac{\partial C_i(x, t)}{\partial t} \quad (7.5)$$

where D_c is the diffusion coefficient of complexes in the matrix.

Owing to the extremely small thickness of the boundary region where the concentration gradient may be neglected, we may envisage for convenience an interface between grain boundary and interior located exactly at $x = 0$ where the solute concentration, C , is $C = C_{br}(t)/\alpha$ where $C_{br}(t)$ is the solute concentration at the concentrated layer when irradiation time is equal to t , and changes with irradiation time at a given irradiation temperature, and $\alpha = C_{br}^m/C_g$. In terms of the Fick's First Law and the Principle of Mass Conservation, the interface should satisfy the following conditions:

$$C = C_{br}(t)/\alpha$$

$$D_c \left(\frac{\partial C}{\partial x}\right)_{x=0} = \frac{d}{2} \frac{\partial C_{br}(t)}{\partial t} \quad (7.6)$$

$$= \frac{1}{2} \alpha d \left(\frac{\partial C}{\partial t}\right)_{x=0}$$

where d is the thickness of the concentrated layer, and the factor $1/2$ is associated with the fact that the complexes diffuse to the boundary from both sides. In terms of above boundary conditions, the solution of Equation (20) is given by [69]

$$\frac{C_{br}(t) - C_g}{C_{br}^m - C_g} = 1 - \exp\left(-\frac{4D_c t}{\alpha^2 d^2}\right) \operatorname{erfc}\left(\frac{2\sqrt{D_c t}}{\alpha d}\right) \quad (7.7)$$

Equation (7.7) is an isothermal kinetic relationship for irradiation-induced grain boundary segregation. It describes the grain boundary segregation level as a function of irradiation time at a given irradiation temperature.

The time required for reaching the steady-state segregation during irradiation may be determined by a critical time. At this critical time the net supply of solute atoms from the grain centres becomes exhausted. After this the reverse flow of solute atoms created by the non-equilibrium segregation concentration gradient is equal to the forward one of the complexes. The critical time, t_c , is given by [38]

$$t_c = \frac{\delta R^2 \ln(D_c/D_i^*)}{4(D_c - D_i^*)} \quad (7.8)$$

where δ is a numerical constant (quoted by Faulkner [67] as 0.05), R is the grain size, D_i^* is the radiation-enhanced diffusion coefficient of the solute in the matrix (see Section 7.2).

7.2. Thermal equilibrium segregation

The above irradiation-induced grain boundary segregation model will be combined with the thermal equilibrium grain boundary segregation model. Here McLean's model [51] is used. This model states that, for a solute with a binding energy to the lattice, Q , at any temperature, T , there will be an increased concentration of that solute on boundaries or interfaces, C_{be}^m . The driving force for this is the reduction of energy, Q , of the solute on placing it in a strain-free region at the grain boundary. C_{be}^m may be determined by Equation (2.1). McLean refined these ideas through accounting for time, realising correctly that the finite time is required to reach equilibrium and this is controlled by the diffusivity of the solute in the matrix, D_i . The equilibrium segregation kinetics during irradiation, $C_{be}(t)$, is given by Equation (2.9).

It should be noted here that although Equation (7.7) is the same as Equation (2.9) in form, they are much different in nature. Equation (2.9) depicts the equilibrium grain boundary segregation level induced by the solute equilibration at the boundary whereas Equation (7.7) describes the non-equilibrium grain boundary segregation level induced by the complex diffusion to the boundary.

For diffusion of solute atoms, irradiation-enhanced diffusion should be considered. It well known that vacancy formation plays an important part in the solute diffusion.

We can calculate the relative concentrations of freely migrating defects under both thermal equilibrium and radiation-induced non-equilibrium conditions. The ratio of these two concentrations will determine the extent that the activation energy for solute diffusion is reduced by lowering the effective vacancy formation energy. A suitable expression could be

$$E_i^* = E_i - \frac{C_v^r}{C_v^e + C_v^r} E_f^v \quad (7.9)$$

where E_i^* is the radiation-reduced activation energy for solute diffusion;

E_i is the activation energy for diffusion of solute atoms in the presence of the thermal equilibrium vacancy concentration;

E_f^v is the vacancy formation energy;

C_v^e and C_v^r are the thermal equilibrium and radiation-generated vacancy concentrations, respectively.

The thermal equilibrium vacancy concentration may be given by

$$C_v^e = A_v \exp\left(-\frac{E_f^v}{kT}\right) \quad (7.10)$$

where A_v is a constant showing the vibrational entropy of atoms around the vacancy, and E_f^v is the vacancy formation energy. The radiation-generated vacancy concentration may be given by [38]

$$C_v^r = \frac{BG}{D_v k_{dv}^2} \quad (7.11)$$

where G is the point defect production rate or dose rate;

D_v is the diffusion coefficient of vacancies in the matrix;

B is the dose rate correction factor, i.e. the fraction of freely migrating defects; and

k_{dv}^2 is the grain interior sink strength for the vacancy, given approximately by [38]

$$k_{dv}^2 = \rho^{\frac{1}{2}} \left(\frac{6}{R} + \rho^{\frac{1}{2}} \right) \quad (7.12)$$

where ρ is the dislocation density, and R is the grain size.

During steady state irradiation, the radiation-generated vacancy concentration is invariant in the matrix, but in regions very close to the grain boundary it would be less than that indicated by Equation (7.11). At present, it is difficult to evaluate vacancy distributions near the grain boundary but this effect could be shown by inserting a factor ε (< 1) into Equation (7.11). Thus Equation (7.11) may be changed to

$$C_v^r = \frac{\varepsilon BG}{D_v k_{av}^2} \quad (7.13)$$

Equation (7.9) is reasonable because in the absence of radiation-generated vacancies the diffusion activation energy becomes the thermal diffusion activation energy. In modelling the radiation-enhanced diffusion coefficient D_i^* has been employed. The increased concentration of vacancies produced by irradiation enhances the solute diffusion rate but does not affect the equilibrium segregation level.

Radiation-induced non-equilibrium segregation and thermal equilibrium segregation are two different processes in nature. Non-equilibrium segregation is a kinetic process while equilibrium segregation is a thermodynamic process. Therefore, it can be envisaged that these two processes are independent each other. In calculations, the total segregation level is taken to be the sum of the non-equilibrium and equilibrium segregation levels minus the bulk concentration of the solute. Moreover, it is assumed in the calculation that (i) the grain boundary concentration of solute atoms before irradiation is C_g ;

7.3. Results

The above combined irradiation-induced and equilibrium grain boundary segregation model has been applied to predictions of grain boundary segregation of phosphorus in the irradiated α -Fe matrix. Data used in the theoretical calculation for phosphorus grain boundary segregation in the α -Fe matrix are listed in Table 1. The determination procedures for some data are as follows.

The diffusion coefficients are given by the following relations

$$D_c = D_{oc} \exp\left(-\frac{E_c}{kT}\right) \quad (7.14a)$$

$$D_v = D_{ov} \exp\left(-\frac{E_m^v}{kT}\right) \quad (7.14b)$$

$$D_I = D_{oI} \exp\left(-\frac{E_m^I}{kT}\right) \quad (7.14c)$$

$$D_i^* = D_{oi} \exp\left(-\frac{E_i^*}{kT}\right) \quad (7.14d)$$

where D_c , D_v , and D_I are the diffusion coefficients of solute-interstitial complexes, vacancies and interstitials in the matrix, respectively;

D_i^* is the irradiation-enhanced diffusion coefficient of solute atoms;

D_{oc} , D_{ov} , D_{oI} and D_{oi} are the pre-exponential constants for diffusion of solute-interstitial complexes, vacancies, interstitials and solute atoms, respectively;

E_m^c , E_m^v and E_m^I are the migration energies for diffusion of solute-interstitial complexes, vacancies and interstitials in the matrix, respectively;

E_i^* is the irradiation-reduced activation energy for diffusion of solute atoms;

T is the absolute temperature; k is Boltzmann's constant.

The dislocation density, ρ , is dependent upon the heat treatment temperature and time, and increases with increasing irradiation dose. In general, the dislocation density, ρ , is relatively high in the irradiated materials. This is because the collapse of vacancy plates created by irradiation can produce a large number of dislocation loops. In addition, the interstitial loop component of the damage structure can also produce a large number of dislocation networks. In general, at lower irradiation temperatures dislocation climb is difficult, and thus the higher dislocation density may be maintained. However, at higher irradiation temperatures the recovery processes may result in an overall net reduction in dislocation density by mechanisms such as climb of dislocations into grain and sub-grain boundaries [172] and dislocation recombination. Consequently, the dislocation density is dependent on the pre-irradiation heat treatment, dose rate, dose, and irradiation temperature. Norris et al. [173] have suggested an equation to describe the dose dependence of the dislocation density for austenitic stainless steels. The equation shows that the dislocation density always increases with increasing dose and is independent of the activation energy for dislocation recovery processes. This seems to be unreasonable because recently the experimental results of Loomis et al. [174] have demonstrated that the dislocation density first increases during irradiation, but it reaches a stable value after a certain dose. Moreover, the work of Hashimoto and Shigenaka [175]

has shown that the temperature dependence of dislocation density during steady state irradiation is in the form of an exponential function. As a result, it is assumed here that after the steady state of the point defect concentration is reached, the dislocation density will no longer vary with increasing the dose. In this case, ρ may be approximately given by

$$\rho = \rho_0 \exp\left(\frac{E_d}{kT}\right) \quad (7.15)$$

where ρ_0 is the dislocation density constant which depends on the pre-irradiation dislocation density, the dose rate, etc., and E_d is the activation energy for dislocation recovery processes.

Data on migration energies of solute-interstitial complexes are sparse. In accordance with the discussion in Ref. [72], there are two ways to lead to long-range migration of mixed dumbbells (impurity-interstitial complexes), one of which is dissociation together with re-formation as well as cage-motion of the mixed dumbbell, the other is rotation together with cage-motion. The cage-motion activation energy of the mixed dumbbell is smaller than the migration energy of the self-interstitial. The mixed dumbbell rotation energy is about 4-5 times as much as the migration energy of the self-interstitial, and is approximately 1.2-1.5 eV for the α -Fe matrix. The dissociation of the mixed dumbbell requires the sum of the self-interstitial migration energy and the mixed dumbbell binding energy. In terms of the calculated value of the phosphorus-interstitial binding energy (0.57 eV) plus the migration energy of 0.3 eV for the α -Fe matrix, this energy is about 0.87 eV. The complex migration energy of 0.87 eV has been employed in this work.

When evaluating the thermal diffusion coefficient of solute atoms, it is necessary to take account of the fact that molybdenum significantly influences phosphorus diffusivity. Low-alloy steels for atomic power mechanical engineering applications are characterised by molybdenum contents in the range of 0.4-1 wt%. The effect of other alloying elements (Mn, Cr and Ni) on the phosphorus diffusivity is considerably weaker than that of molybdenum and may be neglected. Hence the determination of the phosphorus diffusion coefficient in α -Fe alloyed with Mo needs to be modified [164]. The modified value has been applied to this work.

Figure 7.1 shows temperature dependences of P segregation in α -Fe for radiation-induced segregation, equilibrium segregation and total segregation (combined segregation). For equilibrium segregation, there exist two segregation peaks, one of

which is caused mainly by radiation-enhanced equilibrium segregation, the other is brought about mainly by thermal equilibrium segregation, and moreover there is a segregation transition temperature, below which radiation-enhanced equilibrium segregation is dominant and above which thermal equilibrium segregation is dominant. For total segregation there also appear two segregation peaks, one of which is caused mainly by combined radiation-induced non-equilibrium and radiation-enhanced equilibrium segregation, the other is caused mainly by thermal equilibrium segregation.

Effects of neutron dose on the radiation-induced segregation, equilibrium segregation and combined segregation are illustrated in Figs. 7.2-7.4, respectively. They indicate that the segregation peaks shift to lower temperatures with increasing neutron dose at the same neutron dose rate.

Effects of neutron dose rate on the radiation-induced segregation, equilibrium segregation and combined segregation are shown in Figs. 7.5-7.7, respectively, which indicate that segregation peaks all shift to lower temperatures with decreasing neutron dose rate at the same neutron dose. Influences of dislocation density on the radiation-induced segregation and equilibrium segregation are illustrated in Figs. 7.8 and 7.9, respectively. Clearly the dislocation density has an effect on both radiation-induced segregation and equilibrium segregation. The grain size has a considerable effect on radiation-induced segregation (see Fig. 7.10) while it has no effect on equilibrium segregation (see Fig. 7.11).

7.4. Discussion

A combined equilibrium and radiation-induced non-equilibrium grain boundary segregation model has been established for dilute alloys on the basis of the complex mechanism. In this model, the contribution of equilibrium segregation during irradiation was involved, and radiation-enhanced solute diffusion is accommodated. It is well known that when materials are heated at medium temperatures, equilibrium segregation will occur. For example, low-alloy steels will exhibit temper embrittlement as they are tempered in the temperature range, 350 - 600 °C. This temper embrittlement is associated with segregation of some impurities such as P, Sb, Sn, S, and As. Therefore, the above model should theoretically be reasonable.

The introduction of the dose rate correction factor B and dislocation density-temperature dependence (see Equation 7.1) allows the model to be closer to the actual case. As discussed above, an additional feature that acts to reduce the

absolute amount of the solute segregation produces because only a small proportion of point defects created by irradiation may undergo long range migration. Recent studies by Rehn [160] and Naundorf et al. [161] have shown that the ratio of freely migrating point defects produced by charged particle or neutron irradiation to those initially created quantities is only about 1%. More recent studies [162] show that the value of B is in the range of 0.01-0.05. As a consequence, in order to acquire a good agreement between the experimental and theoretical results, it is necessary to postulate that the effective dose rate is only a small part of the calculated value, i.e., a dose rate correction factor, B , should be applied to the term containing the dose rate. The dislocation density, ρ , is dependent upon the heat treatment temperature and time, and increases with increasing irradiation dose. In general, the dislocation density, ρ , is relatively high in the irradiated materials. This is because the collapse of vacancy plates created by irradiation can produce a large number of dislocation loops. In addition, the interstitial loop component of the damage structure can also produce a large number of dislocation networks. In general, at lower irradiation temperatures the dislocation climb is difficult, and then the higher dislocation density may be maintained. However, at higher irradiation temperatures the recovery processes may result in an overall net reduction in dislocation density by mechanisms such as climb of dislocations into grain and sub-grain boundaries [172] and the recombination of different sign dislocations. Consequently, the dislocation density is dependent on the pre-irradiation heat treatment, dose rate, dose, and irradiation temperature. Recently the experimental results of Loomis et al. [174] have demonstrated that the dislocation density first increases during irradiation, but it reaches a stable value after a certain quantity of doses. Furthermore, the work of Hashimoto and Shigenaka [175] has shown that the temperature dependence of dislocation density at the steady state of irradiation is in the form of exponential function and is not associated with the dose.

The above predicted results (see Fig. 7.1) demonstrate that above the transition temperature the effect of radiation-enhanced solute diffusion on equilibrium segregation is small because the radiation-generated vacancy concentration is small; below the transition temperature, radiation-enhanced solute diffusion begins to take effect obviously. However, it may be seen from Equation 7.13 that there is a temperature at which the influence of radiation-created vacancies on equilibrium segregation kinetics is greatest. Below this temperature, although the vacancy concentration is higher to reduce the activation energy for diffusion of solute atoms, the solute diffusion is still slower due to lower temperatures and above this temperature it is also still slower due to lower vacancy concentrations. Furthermore,

it may also be seen from Equations (7.1) and (7.7) that there should be a temperature at which the radiation-induced segregation magnitude is largest. Below this temperature, although the maximum non-equilibrium segregation amount is larger the radiation-induced segregation level is still lower because of slower kinetic processes, and above this temperature it is also still lower because of lower maximum segregation levels. As a consequence, for both equilibrium segregation and combined radiation-induced non-equilibrium and equilibrium segregation there will be two segregation peaks. In the two segregation peaks, one, at a higher temperature, is caused mainly by thermal equilibrium segregation, the other, at a lower temperature, is caused mainly by radiation-enhanced equilibrium segregation (for the temperature dependence of equilibrium segregation, see Fig. 7.3) or by combined radiation-induced non-equilibrium and radiation-enhanced equilibrium segregation (for the temperature dependence of total segregation, see Fig. 7.4).

The dislocation density has a noticeable effect on both radiation-induced segregation and equilibrium segregation. The influence of dislocation density is seen in the kinetics of equilibrium segregation (see Equation (7.9)) and the quasi-thermodynamics of radiation-induced segregation (see Equation (7.1)) as well as the critical time (see Equation (7.8)). The grain size has a considerable effect on radiation-induced segregation (see Fig. 7.10) while it has no effect on equilibrium segregation (see Fig. 7.11). The grain size effect on radiation-induced segregation is caused mainly by its influence on the critical time (see Equation (7.8)). Therefore, it is necessary, in theoretical calculations, to use the appropriate dislocation density and grain size in order to obtain a good fit between the experimental and predicted results.

The grain size effect shown in Fig. 7.10 is useful in explaining why some of the predictions for the enrichment suggest that the boundary concentration will be greater than 100%. For the pressure vessel steel being considered in this project the structure is that of tempered martensite. There are vast numbers of lath and lath packet boundaries present. There is some evidence to suggest that these boundaries act as good sinks for point defects. Hence the appropriate grain size is about 1 micron. In this case, the predicted phosphorus boundary concentrations will be much less than 100%, and the higher enrichments predicted for the larger grained materials are somewhat irrelevant to this case.

It is seen from Fig. 7.1 that the combined radiation-induced non-equilibrium and radiation-enhanced equilibrium peak segregation temperature and the thermal

equilibrium peak segregation temperature are about 150 and 550 °C, respectively, for phosphorus grain boundary segregation in the α -Fe matrix at dose rate = 10^{-6} dpa/s and dose = 1 dpa. Therefore, when analysing irradiation-induced embrittlement of low-alloy ferritic steels one should simultaneously think of equilibrium and radiation-induced non-equilibrium grain boundary segregation of embrittling elements such as phosphorus. If we assume here that irradiation-induced non-hardening embrittlement is brought about by P grain boundary segregation during irradiation, we may predict from this work that, at dose rate = 10^{-6} dpa/s and dose = 1 dpa, the ferritic steels will exhibit considerable phosphorus segregation as they are irradiated in the vicinity of 150 and 550 °C. In practice, when low-alloy ferritic steels are tempered in the range of 400-550 °C, they will exhibit temper embrittlement associated with grain boundary segregation of phosphorus [176,177], which leads to intergranular fracture. Similar intergranular fracture could be predicted to be associated with combined radiation-induced non-equilibrium and equilibrium segregation of phosphorus.

7.5. Summary

A combined equilibrium and radiation-induced non-equilibrium grain boundary segregation model has been established for dilute alloys on the basis of the complex mechanism. In the treatment of equilibrium segregation, radiation-enhanced solute diffusion is taken into account. The analysis has been applied to predictions of phosphorus grain boundary segregation in the α -Fe matrix under neutron irradiation.

The predicted results demonstrate that (i) there exists a segregation transition temperature below which combined irradiation-induced non-equilibrium and irradiation-enhanced equilibrium segregation is dominant, and above which thermal equilibrium segregation is dominant; (ii) peaks in the temperature dependence of segregation shift to lower temperatures with decreasing neutron dose rate and/or increasing neutron dose; (iii) the combined irradiation-induced non-equilibrium and irradiation-enhanced equilibrium peak segregation temperature and thermal equilibrium peak segregation temperature are about 150 and 550 °C, respectively, for phosphorus grain boundary segregation in α -Fe at dose rate = 10^{-6} dpa/s and dose = 1 dpa. Comparison of the predictions with some existing observations indicates that the model works satisfactorily.

The dislocation density has an effect on both radiation-induced segregation and equilibrium segregation. The grain size strongly influences radiation-induced segregation.

Appendix 7.1
Tables for Chapter Seven

Table 7.1. Data used in the theoretical calculation

A_I	1 [165]
A_v	1 [164]
E_f^v (eV)	1.4 [166]
E_f^I (eV)	3.0
E_b^{II} (eV)	0.57
E_i (eV)	2.68 [164]
E_m^c (eV)	0.87
E_m^I (eV)	0.3 [167]
E_m^v (eV)	1.24 [168]
D_{oi} (m^2s^{-1})	7.12×10^{-3} [164]
D_{∞} (m^2s^{-1})	8×10^{-7} [28]
D_{oi} (m^2s^{-1})	5×10^{-6} [28]
D_{ov} (m^2s^{-1})	5×10^{-5} [164,117]
k_e	12 [117]
Z_I	1.1 [169]
E_d (eV)	0.1 [170]
C_g (at%)	0.072
B	0.01
ϵ	0.1
β	0.775 [171]
Q (eV)	0.397 [171]
d (nm)	1.0

Appendix 7.2
Figures for Chapter Seven

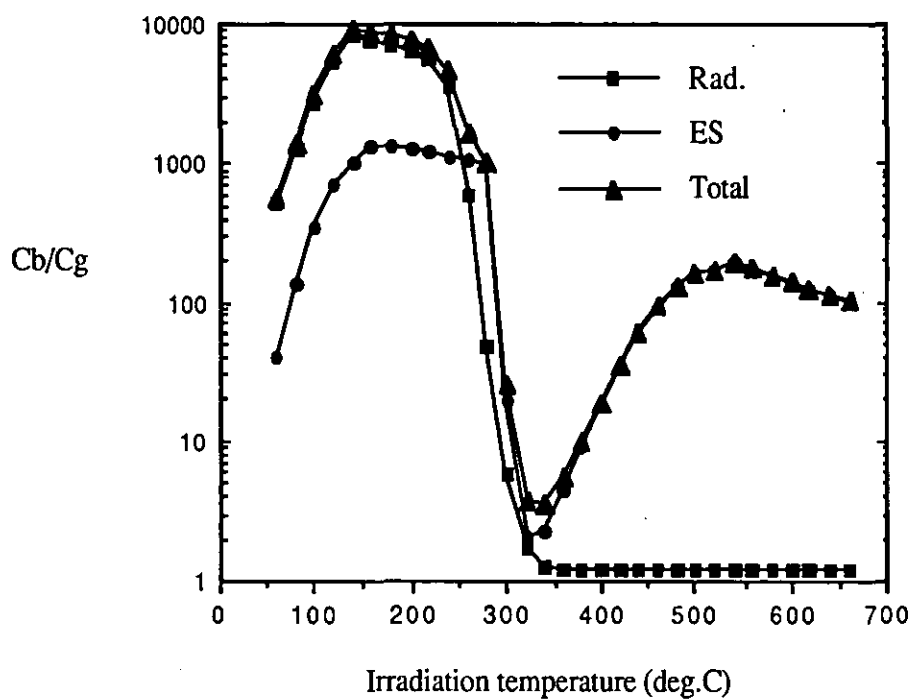


Fig. 7.1. Temperature dependences of radiation-induced segregation (Rad.), equilibrium segregation (ES) and total segregation (Total) of phosphorus in α -Fe (Dose rate = 10^{-6} dpa/s, Dose = 1 dpa, $\rho_o = 10^{18} \text{ m}^{-2}$, $R = 20 \text{ }\mu\text{m}$).

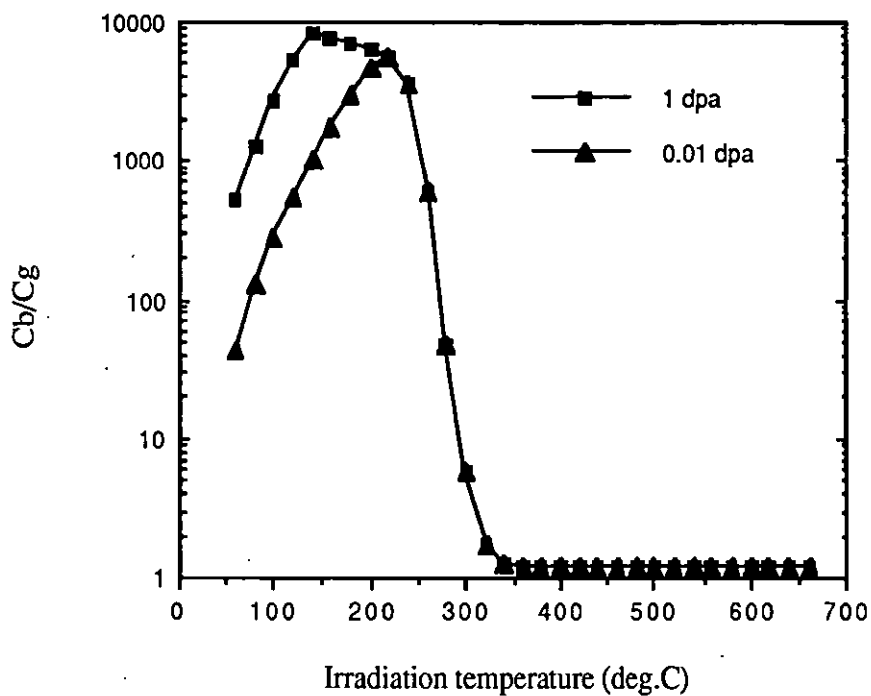


Fig. 7.2. Temperature dependences of radiation-induced phosphorus segregation in α -Fe at different neutron doses (Dose rate = 10^{-6} dpa/s, $\rho_o = 10^{18} \text{ m}^{-2}$, $R = 20 \text{ }\mu\text{m}$).

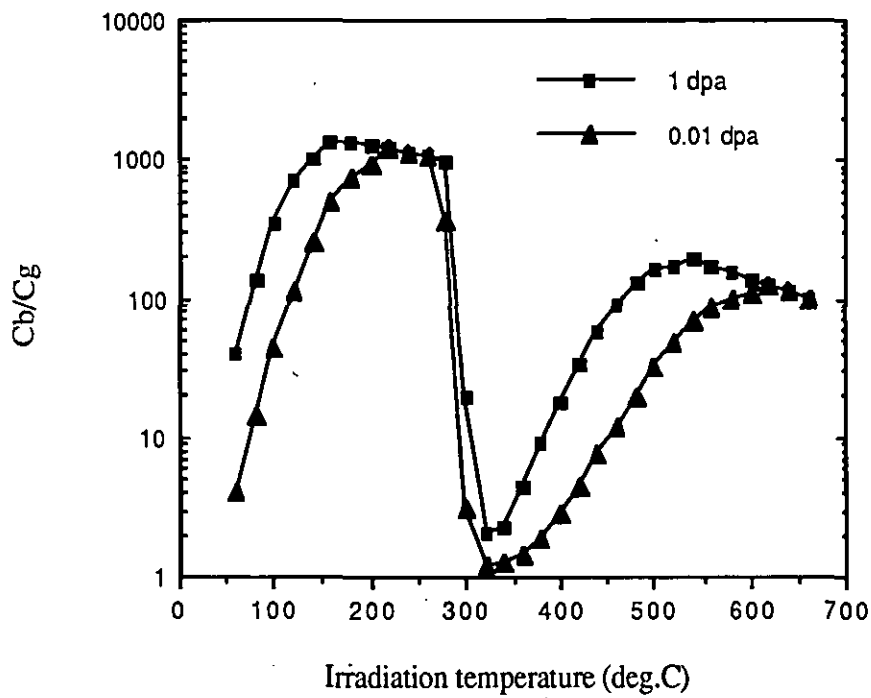


Fig. 7.3. Temperature dependences of equilibrium phosphorus segregation in α -Fe at different neutron doses (Dose rate = 10^{-6} dpa/s, $\rho_o = 10^{18} \text{ m}^{-2}$, $R = 20 \text{ }\mu\text{m}$).

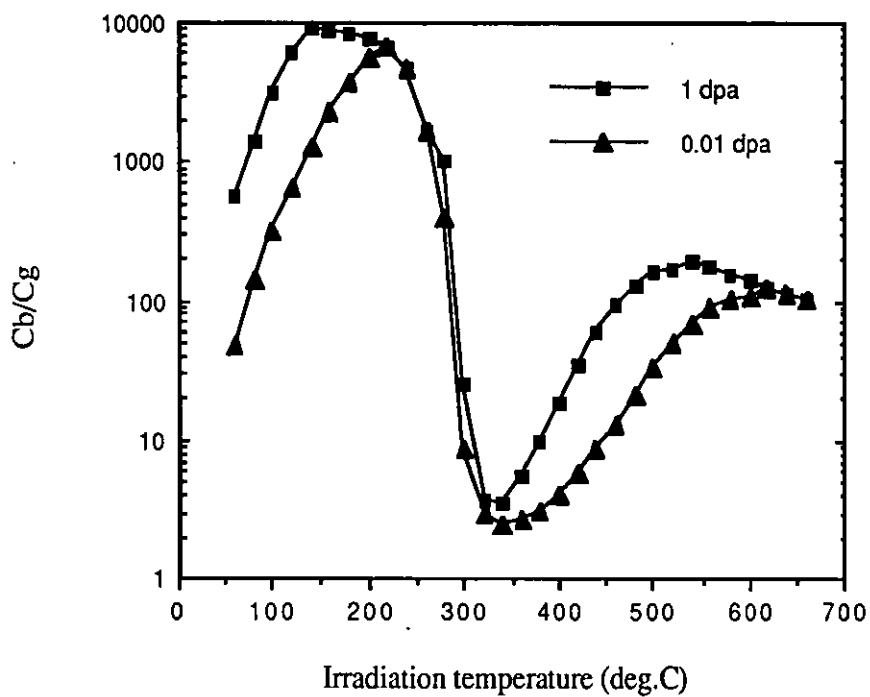


Fig. 7.4. Temperature dependences of total phosphorus segregation in α -Fe at different neutron doses (Dose rate = 10^{-6} dpa/s, $\rho_0 = 10^{18} \text{ m}^{-2}$, $R = 20 \text{ }\mu\text{m}$).

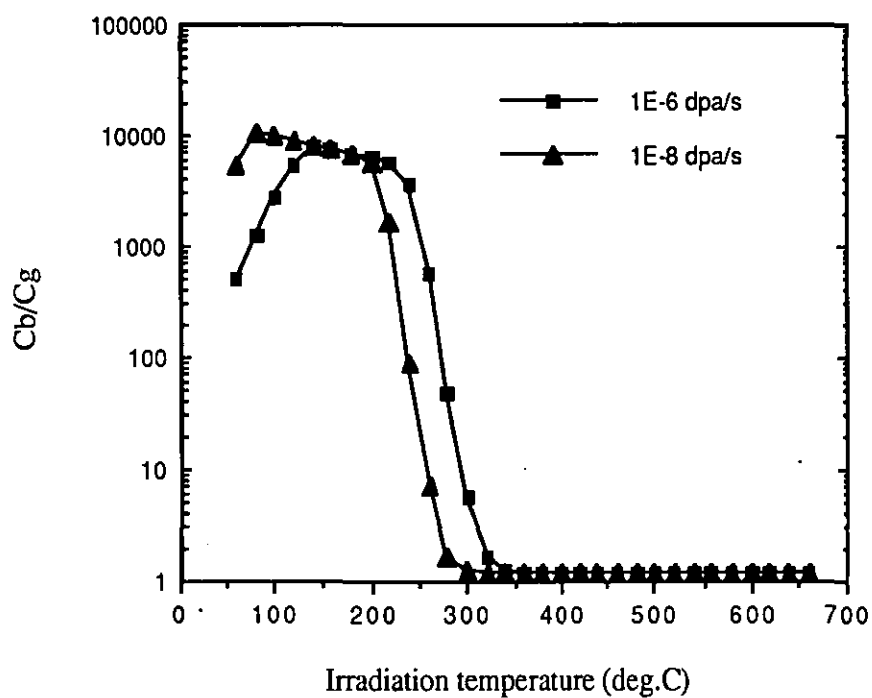


Fig. 7.5. Temperature dependences of radiation-induced phosphorus segregation in α -Fe at different neutron dose rates (Dose = 1 dpa, $\rho_o = 10^{18} \text{ m}^{-2}$, $R = 20 \mu\text{m}$).

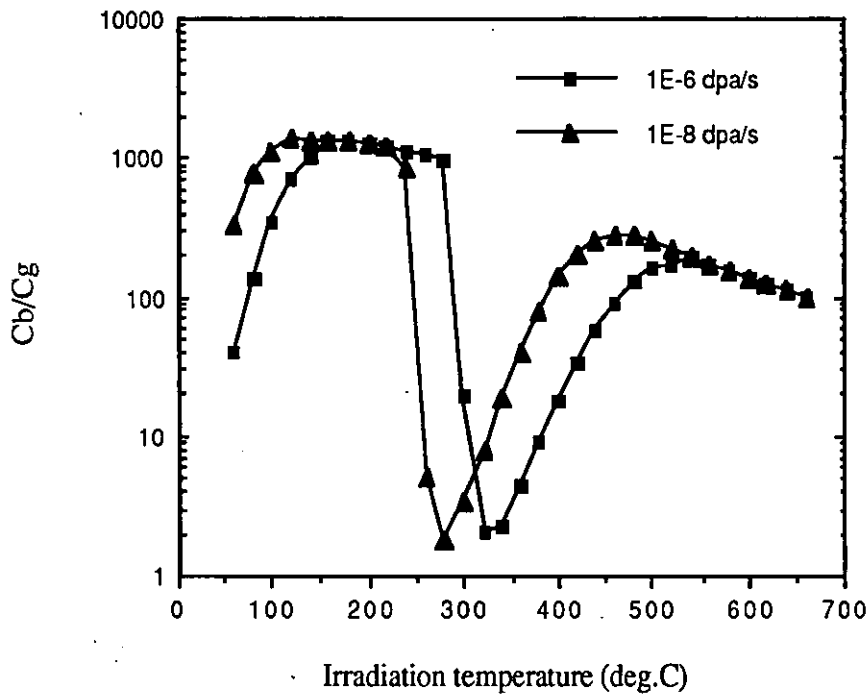


Fig. 7.6. Temperature dependences of equilibrium phosphorus segregation in α -Fe at different neutron dose rates (Dose = 1 dpa, $\rho_o = 10^{18} \text{ m}^{-2}$, $R = 20 \text{ }\mu\text{m}$).

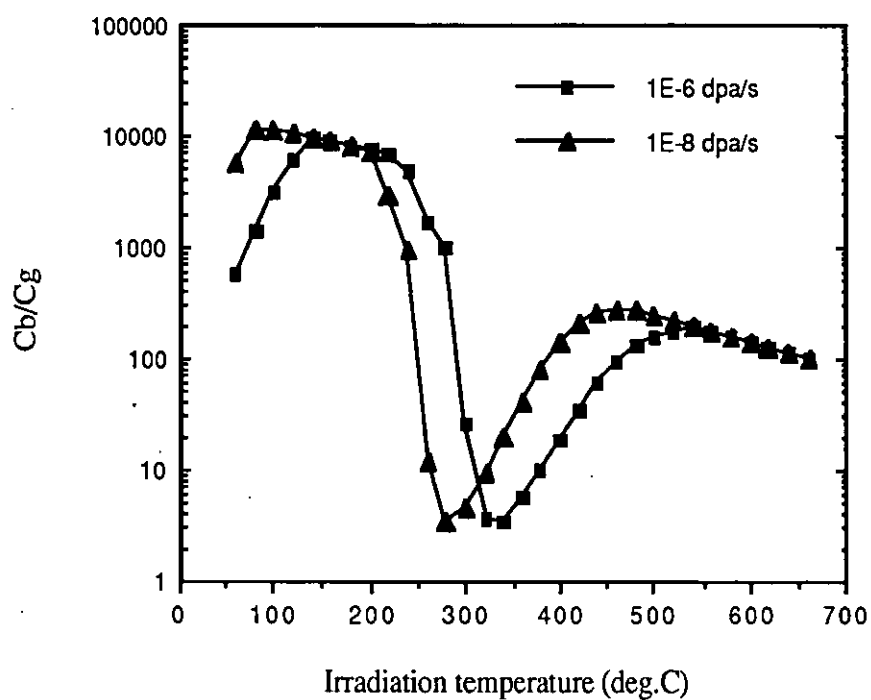


Fig. 7.7. Temperature dependences of total phosphorus segregation in α -Fe at different neutron dose rates (Dose = 1 dpa, $\rho_o = 10^{18} \text{ m}^{-2}$, $R = 20 \text{ }\mu\text{m}$).

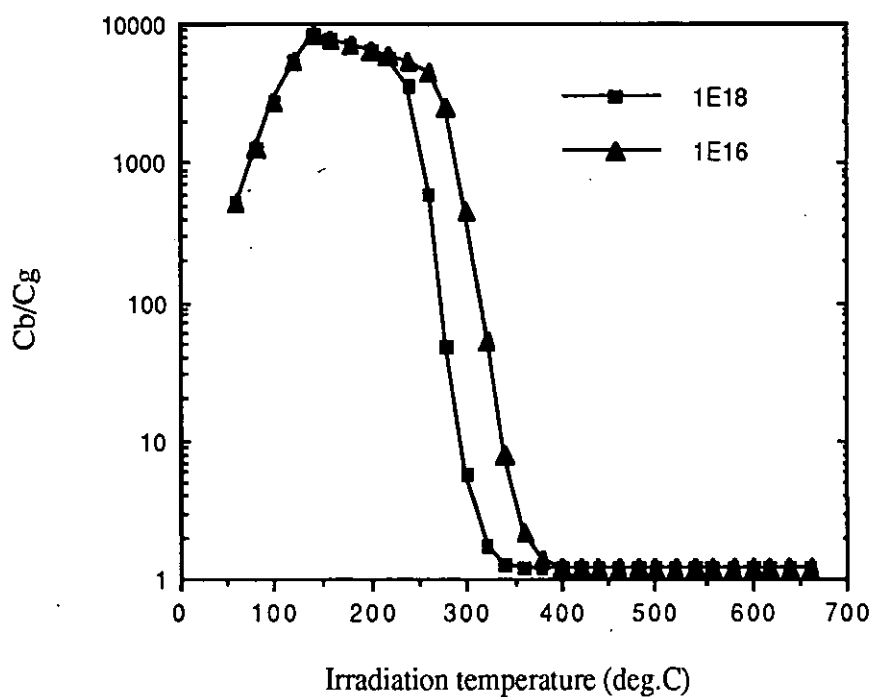


Fig. 7.8. Temperature dependences of radiation-induced phosphorus segregation in α -Fe at different dislocation density constants (m^{-2}) (Dose rate = 10^{-6} dpa/s, Dose = 1 dpa, $R = 20 \mu m$).

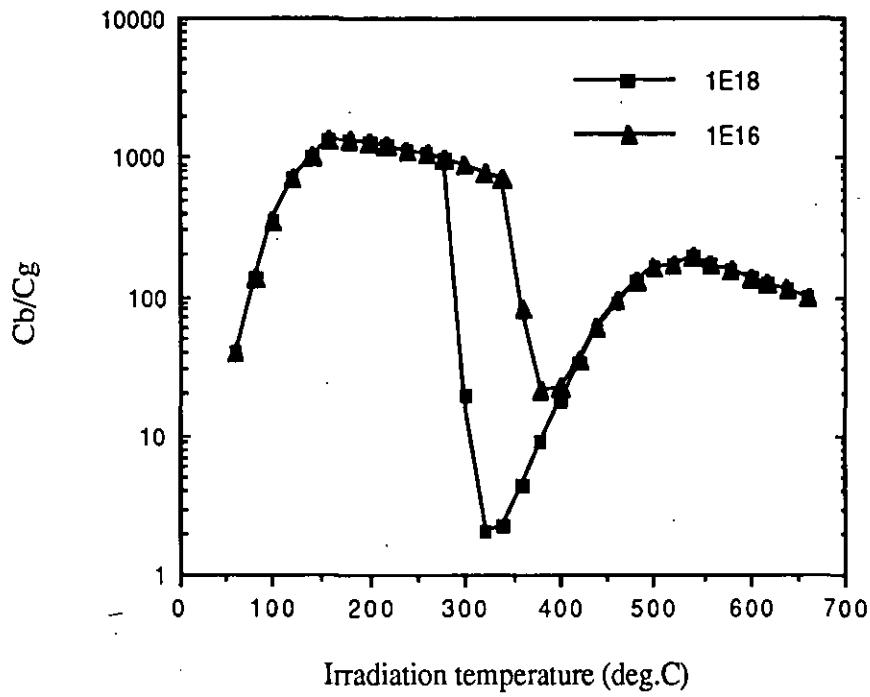


Fig. 7.9. Temperature dependences of equilibrium phosphorus segregation in α -Fe at different dislocation density constants (m^{-2}) (Dose rate = 10^{-6} dpa/s, Dose = 1 dpa, $R = 20 \mu m$).

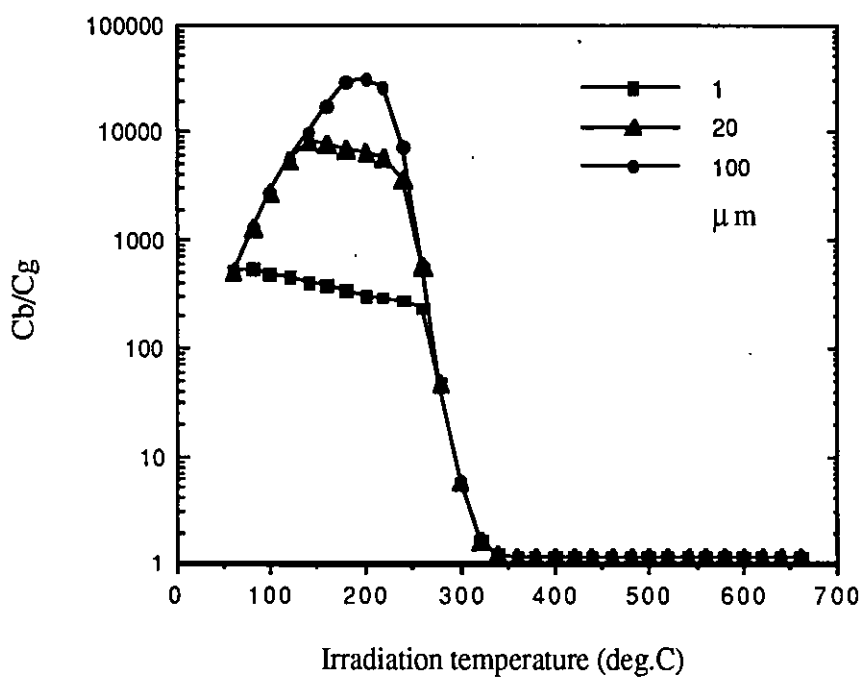


Fig. 7.10. Temperature dependences of radiation-induced phosphorus segregation in α -Fe at different grain sizes (Dose rate = 10^{-6} dpa/s, Dose = 1 dpa, $\rho_0 = 10^{18} \text{ m}^{-2}$).

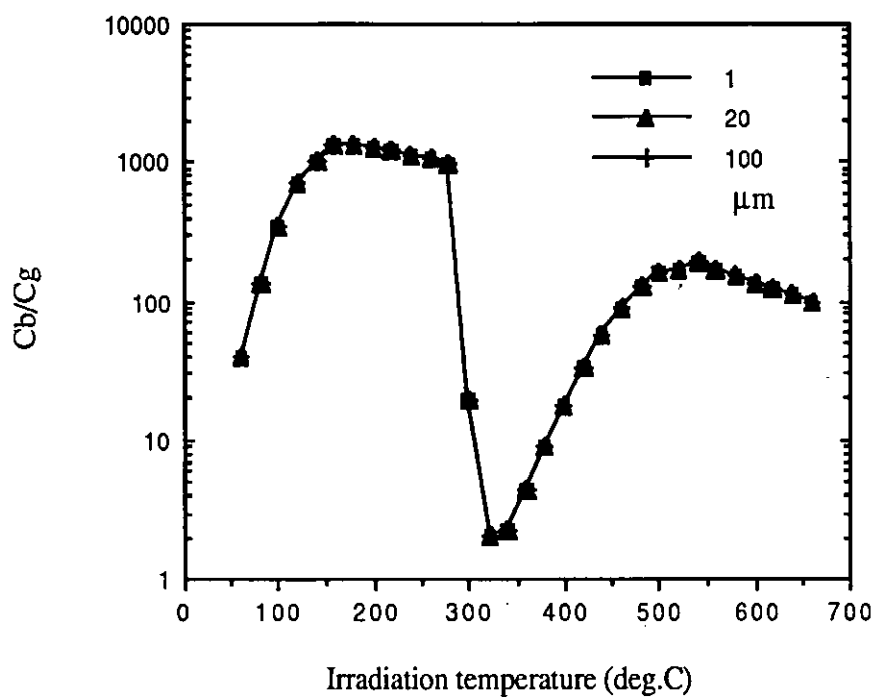


Fig. 7.11. Temperature dependences of equilibrium phosphorus segregation in α -Fe at different grain sizes (Dose rate = 10^{-6} dpa/s, Dose = 1 dpa, $\rho_o = 10^{18} \text{ m}^{-2}$).

Chapter Eight

Experimental Studies

Obviously no model is defensible unless it may be tested experimentally. In order to corroborate the theoretical predictions, detailed in Chapter Seven, it is indispensable to observe segregation levels for some impurity and solute elements in irradiated dilute alloys. We have experimentally investigated radiation-induced segregation in 2.25Cr-1Mo steels by means of analytical field emission gun scanning transmission electron microscopy (FEGSTEM). In this chapter, the experimental details will be presented.

8.1. Experimental alloys

Nominal 2.25Cr1Mo steels doped with 0.077 wt%P and 0.077 wt%Sn were prepared by induction melting of the base elements under an argon atmosphere. The resulting ingots were hot rolled to 10 mm diameter rods and they were then austenitised for two hours at 1150 °C, furnace cooled to an intermediate temperature of 950 °C, held there for half an hour and then air cooled to room temperature. All the rod samples pre-treated above were finally austenitised for two hours at 1050 °C and then water quenched. The chemical composition of the steels is shown in Table 8.1.

8.2. Specimen preparation

Because of the problems associated with active material handling, before irradiation the specimens were quasi-prepared TEM discs. In order to reduce γ -ray emission from radioactive specimens which affects energy dispersive X-ray microanalysis, the 2 mm dia. discs were cut and trepanned by a Spark erosion machine and then mechanically polished to about 0.1 mm thick. In order to have identical specimen size conditions the thermal control specimens are the same as those for irradiation.

8.3. Irradiation

Material irradiation was performed in a thermal, light water, open pool type research reactor, named SAPHIR, operated by the Swiss Federal Institute for Reactor Research at Villigen in Switzerland. This reactor operates at a thermal power of 10 MW. The thermal neutron flux is $8 \times 10^{13} \text{ n} \cdot \text{cm}^{-2} \text{ s}^{-1}$ at the core surface, and up to $1.2 \times 10^{14} \text{ n} \cdot \text{cm}^{-2} \text{ s}^{-1}$ in the central irradiation positions.

The reactor building contains the reactor and experimental halls, control room and all rooms for the necessary auxiliary equipment such as work shops, water

purification, electricity distribution and offices. The core is assembled with standard 23 plate material test reactor fuel elements. Presently there are two type of element in use, a high enriched (93%) with 280g U-235 and a medium enriched with 320g U-235 for the standard element. A detailed description of the reactor may be found in Appendix 8.3. In this work, the irradiation dose and dose rate are about 0.042 dpa [fast neutron fluence (>1 MeV): $\sim 2.65 \times 10^{19} \text{ n} \cdot \text{cm}^{-2}$] and 1.05×10^{-8} dpa/s [fast neutron flux (>1 MeV): $\sim 6.67 \times 10^{12} \text{ n} \cdot \text{cm}^{-2} \text{ s}^{-1}$]; and the nominal irradiation temperature is 250 °C. However, owing to the limited colling capability of the system the irradiation temperature has some fluctuations during irradiation. The irradiation temperature is illustrated as a function of irradiation time in Fig. 8.1.

8.4. Thermal ageing

To enable radiation effects to be distinguished from any purely thermal effects generated from time spent during irradiation, thermal control specimens were produced and aged by simulating the irradiation process (see Fig. 8.1). Henceforth, thermal-aged samples are called unirradiated samples.

8.5. Thin foil preparation

Irradiated and thermally-aged 2 mm dia. discs were slightly polished on fine grade silicon carbide paper to clean the specimen surfaces and then electropolished by using a Struers Tenupol dual-jet electropolishing machine to achieve thin foil regions that are electron-transparent. Good thin foils were found to be consistently produced by employing an electrolyte of 5% perchloric acid and 95% methanol, cooled by liquid nitrogen to -60 °C. The operating voltage used was about 25 V. The electrolyte flow was set to maximum for the first minute of electropolishing to dimple the disc, and then reduced to a lower rate till perforation took place. The thin foils were then cleaned in acetone and stored under absolute alcohol.

8.6. Transmission electron microscopy (TEM)

The thin foils were examined in a Philips EM 400 TEM equipped with a LaB₆ source, operating at 120 KV. Ten foils prepared for each material condition were initially assessed according to their suitability for subsequent segregation analysis. With regard to the presence of the desired sink types within the thin area. The three best foils for each material condition were selected for further analysis using the FEGSTEM.

8.7. Microchemical analysis

The instrument used to determine spatial chemical composition distributions was the Vacuum Generators HB501 field emission gun scanning transmission electron microscope (FEGSTEM). It offers advantages over conventionally illuminated STEMs for high resolution microanalysis. Here a brief description of this technique is supplied and more detailed description may be seen in Refs. [178,179].

8.7.1. VG HB501 FEGSTEM

In the FEGSTEM, the electron source, the field emission gun uses a fine needle of single crystal tungsten with a $\langle 310 \rangle$ zone axis. The emission of electrons, under the application of a strong electric field, from a very localised region of the tip, results in a very high value of brightness. From the analytical standpoint alone, an FEG is an ideal electron source giving a very large electron beam current in a very small probe (it may be less than 1 nm in diameter with an energy spread of ~ 0.5 eV [180]).

A first anode held at 3-4 KV positioned close to the tip extracts electrons by tunnelling through the crystal surface potential barrier. The second anode accelerates the electrons to 100 KV. For stable electron emission a gun chamber vacuum of better than 10^{-10} torr is required; the HB501 has a guaranteed gun chamber pressure of better than 5×10^{-11} torr. Even so, focussing of contaminant gas ions can cause tip instabilities. To overcome this, the tip extraction voltage is periodically switched off and a heating current passed to drive off adsorbed gas atoms.

Working up the optical system, the gun lens initially focuses the beam producing a crossover near the plane of the differential pumping aperture. The gun lens is not beneficial for the finest probes, since its function is to increase beam current in probe sizes greater than 3 nm diameter. The differential pumping aperture can maintain a pressure difference of 10^3 between the gun chamber and the rest of the microscope which typically has a vacuum of 10^{-9} to 10^{-8} torr.

A double condenser lens system is utilised to transfer the image of the source to the plane of the selected area diffraction aperture (SADA). The double condenser allows in principle the variation of any two of the three parameters of beam current, probe size and convergence angle, while keeping the third constant. In practice the fixed parameter is governed by the field limiting aperture. If the objective aperture (OA) is chosen then the convergence angle is fixed, whereas the beam current is constant if the virtual objective aperture (VOA). Use of the OA brings about a spurious X-ray signal. Hence for EDX work a VOA and a small SADA are used.

For aberration-free imaging of the electron source, the probe current is given by [172]

$$i = \frac{\pi^2 \alpha_c^2 d_p^2 B_s}{4} \quad (8.1)$$

where α_c is the convergence angle, d_p is the probe diameter and B_s is the source brightness. Thus under conditions for EDX work, where a VOA is applied to fixing the beam current, the probe diameter is inversely proportional to the convergence angle:

$$d_p = \frac{2}{\pi \alpha_c} \sqrt{\frac{i}{B_s}} \quad (8.2)$$

Spherical aberration limits the minimum attainable beam diameter at high convergence angles, obeying the following relation:

$$d_s = \frac{1}{2} C_s \alpha_c^3 \quad (8.3)$$

where C_s is the coefficient of spherical aberration. Diffraction effects also limits the minimum beam diameter according to the following relation:

$$d_d = \frac{1.22\lambda}{\alpha_c} \quad (8.4)$$

where λ is the wavelength of the electron beam. These three criteria can jointly affect the probe size to a theoretical variation of probe size with convergence angle. Under conditions typical for EDX analysis, the minimum attainable probe diameter is ~2.3 nm for a current of 1 nA. For the same convergence angle and beam current, the aberration-free Gaussian probe diameter will be greater by a factor of 14 for a LaB6 source and by a factor of 45 for a thermionic tungsten filament (assuming brightnesses of 10^7 , 5×10^4 and 5×10^3 A/mm²/sr for cold field emission, LaB6 and tungsten sources, respectively [181]). This increase in brightness is the key to the FEGSTEM's ability to produce extremely fine probes, yet which contain sufficient current for statistically significant X-ray generation in reasonable collection times.

The specimen holder is fitted into a top entry stage, immersing the foil in the high excitation objective lens field. A special single tilt holder is necessary for the examination of ferritic foils, since the very strong interaction between the objective lens field and the ferromagnetic specimen has been found to damage the gimbal mechanism in a conventional double tilt holder. The specimen holder gimbal assemblage is of beryllium construction to minimise background X-ray generation.

The absence of post-specimen lenses results in space for a variety of detectors. The first of these is a retractable fluorescent screen angled at 45° , used to view the diffraction pattern. The annular dark field detector is linked with a photomultiplier and the visual display units of the microscope. This collects electrons scattering from the incident electron beam to quite high angles and is useful for imaging precipitates. The bright field detector and the electron spectrometer collect electrons close to the optic axis for bright field imaging and electron energy loss spectroscopy. The original electron energy loss spectrometer was a serial device and is currently being replaced by a parallel collection device offers significant benefits for high resolution microanalysis.

In the present work, the energy dispersive X-ray (EDX) microanalysis system were used. The X-ray detector is a Link systems LZ-5 retractable windowless Si(Li) crystal subtending a high solid collection angle of 0.181 sr. The absence of a beryllium window allows detection of all elements in periodic table down to boron (atomic no. 5). It is of the very low column pressure in the HB501 that allows the use of a windowless detector without contamination of the crystal rapidly deteriorating performance. Typically the detector may be employed for about twelve months before decontaminating by a crystal warm-up procedure. The detector has good resolution for an energy dispersive system.

The data analysing system is the Link systems AN10000 X-ray microanalysis system. Apart from straightforward collection of X-ray spectra, the system may be used to drive the electron probe to generate linescans or acquire elemental X-ray maps and digital electron image. These may subsequently be manipulated by a digital image processing and displaying package which allows image analysis to generate, for example, histograms and line profiles.

8.7.2. Procedure

The specimen under examination was, whenever possible, taken from storage under absolute ethanol, mounted in the holder and inserted into the specimen stage of the

microscope at the night before intended analysis. This may allow the specimen to settle and minimise drift at the start of analysis at the following day. For analysis a suitable interface of the desired type was selected and oriented so that its plane was parallel to the incident electron beam.

If there exists precipitation at the boundary or within the grain, a precipitate-free section must be nearly aligned to the beam prior to tilting it exactly parallel, since there is only a limited angle of tilt available to work with for EDX analysis, defined by line-of-sight between the analysis point and detector. For ferritic foils, tilting range is also constrained by the range over which objective astigmatism can fully be corrected. The use of the single tilt holder also needs the boundary section to be roughly parallel- or at least not perpendicular- to the tilt axis so that the boundary may be tilted successfully to be parallel to the electron beam. The boundary section should also ideally lie in a thin region of the foil to minimise beam broadening effects which degrade the spatial resolution of the analysis.

For each grain boundary, three positions were analysed and the arithmetic mean of data obtained was taken as the measured value. Four grain boundaries were analysed for each kind of sample. Spatial compositional data across an interface were obtained by placing the stationary electron probe at the required analysis point and collecting an EDX spectrum for proper time (usually ~100 seconds). Spectra were achieved for points on the boundary and at distances of 1.25, 2.5, 5 and 10 nm on either side of the boundary. Two or three profiles were determined for each kind of sample.

7.7.3. Specimen analysis considerations

7.7.3.1. Drift

Specimen drift may arise from fluctuations in cooling water temperature, specimen holder instability, beam heating, stray electromagnetic fields and others. The drift was corrected by periodically halting data acquisition to examine the beam position relative to a reference point and repositioning if necessary. The drift was kept to within about 0.5 nm when analysing compositions between 5 nm on either side of the interface. If the specimen was found to have drifted by more than this between successive checks, the spectrum was discarded and started afresh.

8.7.3.2. Contamination

Contamination is a further barrier to good microanalysis. Adsorbed hydrocarbon molecules on the specimen surface leads to a carbon-rich cross-linked structure

under the electron beam. This contamination becomes particularly evident if using very fine probes, when a contamination needle is produced. Surface diffusion of hydrocarbons allows the needle to continue to grow under the electron probe. The effect can be deliberately used to advantage in foil thickness measurements. However, for microanalysis the presence of such contamination needles is deleterious. The contamination needle may easily more than double the effective specimen thickness under the electron probe. Elastic scattering can therefore broaden the beam before it even reaches the specimen surface and its exit diameter will be further increased, resulting in a loss of spatial resolution. In addition, the growth of contamination peaks eventually obscures image details, which may be a particular problem when analysing the composition at closely spaced points near to the interface.

Fortunately, the windowless X-ray detector is capable of measuring carbon K-line X-rays and the height of this peak allows the extent of carbon build-up to be monitored before it actually becomes visible in the image. To minimise contamination the specimen is 'flooded' with electrons before analysis of an interface begins and also once the carbon K_{α} peak is observed to be increasing significantly. The apertures are removed and the magnification reduced so that an intense beam of electrons sweeps across a large portion of the foil.

8.7.3.3. Specimen thickness

The specimen thickness at the point of analysis is primarily determined by the location of a suitable boundary section, rather than by the operator. However, some considerations must be given to the local specimen thickness. Thick regions give rise to considerable broadening of the incident electron beam as it travels through the foil. As a consequence, there is a degradation of spatial resolution and sensitivity to equilibrium segregation where the width of the segregated layer is less than the diameter of the probe trying to determine its extent.

Under ideal conditions the thinnest regions of the foil will lead to the best resolution and sensitivity for microanalysis; in reality, counting times, surface artefacts and background radiation for active foils become dominant factors. For very thin specimens, the X-ray generation rate is low and data acquisition must be performed for longer times to improve counting statistics. Apart from the inconvenience of slower analysis, longer counting times also give more opportunity for specimen drift.

A related effect of a constant background 'noise' peculiar to the active material is the X-ray count generated by the specimen-induced radioactivity. This is dealt with further in relation to spectrum quantification. It is clear that the lower the rate of electron-beam-induced X-ray generation, the greater the effect.

Hence the optimum specimen thickness is a compromise, so that the electron-generated X-ray count is as high as possible without significant beam broadening. It is found from experience that the choice of suitable foil thicknesses is largely intuitive. Some measurements were made for local foil thicknesses by electron energy loss spectroscopy (EELS). The thicknesses measured were less than 50 nm, with 40 nm being typical.

8.7.3.4. Boundary tilt

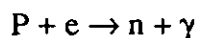
Owing to the fine electron probe used in this work, boundary misorientation is also of importance to microanalytical resolution. For a larger probe size, say, 15 to 20 nm, as with thermionic sourced instruments, substantial boundary orientation misalignment would be required for the boundary to fall outside the analysed volume through the thickness of the foil. A simple calculation of electron probe/boundary geometry reveals that misorientations of greater than 11° for a 20 nm diameter probe, but only 1.1° for a 3 nm diameter probe, are necessary for part of the boundary to lie outside the analysed volume. This calculation assumes a foil thickness of 50 nm and a planar boundary of width 2 nm centred under the incident beam, and neglects beam broadening effects.

Vatter and Titchmarsh [182] have performed Monte-Carlo calculations to predict the influence of boundary misorientation on measured EDX compositional profiles. Fig. 8.2 shows the variation in phosphorus concentration detected at the boundary as a function of boundary tilt.

8.7.4. Spectrum quantification

Spectrum quantification involves spectrum treatment to extract elemental peak intensities and then conversion of these intensities to yield elemental concentration. The Link analytical quantification package RTS2/FLS (Ratio Thin Section, Filtered Least Squares) was applied to this work with the AN10000 microanalysis system. However, For active (irradiated) foils, Spectra obtained have to be corrected for their intrinsic 'spectra' originating from the specimen-induced radioactivity. The major peak in the 'no-beam' spectrum corresponds to that of Mn K_α with its accompanying K_β .

The capture of an extra neutron by ^{54}Fe forms an unstable ^{55}Fe nucleide. This decays by electron capture to ^{55}Mn , whereby a K-shell electron combines with a proton in the unstable nucleus forming a neutron via the reaction



The resulting hole in the K-shell is filled by electronic transition with the simultaneous generation of characteristic Mn K-line X-rays. These in turn may fluoresce the chromium present in the specimen to generate Cr K-line X-rays. Furthermore, there is an increase in low energy background levels, which makes quantification of elements with characteristic X-ray energies more subjected to error. This 'no-beam' spectrum will be superimposed on any electron-beam-generated X-ray spectrum collected. In order to eliminate the effect of 'no-beam count' spectrum on the measured results in quantification the characteristic Mn X-ray intensity was not collected. In consideration of the low concentration of chromium in specimens concerned in this work, the Cr X-ray contribution to the 'no-beam count' spectrum should be very small.

8.7.5. Error estimation of the analysed results

Actually ascertained (collected, measured, observed) values are usually called observations. In a particular situation, they are certain numbers x_1, x_2, \dots, x_n , and in theoretical consideration they are regarded as random variables x_1, x_2, \dots, x_n , which can assume various values in terms of a certain probability distribution. Values computed from the given observations for purposes of their statistical analysis are termed statistics; every statistic is a certain function $s = s(x_1, x_2, \dots, x_n)$ of the observations x_1, x_2, \dots, x_n .

The working premises respecting an unknown probability distribution of the given observations are called a model. For this, the most important example is a random sample, which is defined as a family of n independent observations x_1, x_2, \dots, x_n , all with the same distribution, or a family of pairs $(x_1, y_1), (x_2, y_2), \dots, (x_n, y_n)$, or of still larger groups of observations in the light of the character of the problem. In other words, a random sample is formed by observations on one or more variables through n independent repetitions under the same conditions. In a random sample consisting of n independent observations x_1, x_2, \dots, x_n , the most common statistic employed to account for the extent of the instability of the observations is the sample standard deviation, which is given by [183]

$$s = \sqrt{\frac{1}{n-1} \sum_{i=1}^n (x_i - \bar{x})^2} \quad (8.5)$$

where \bar{x} is the sample mean, which is given by

$$\bar{x} = \frac{1}{n} \sum_{i=1}^n x_i \quad (8.6)$$

In this work, the sample standard deviation has been adopted to account for the extent of the stability of the measured results.

8.8. Results and discussion

8.8.1. Microstructure

Optical metallography showed that all the 2.25Cr-1Mo steel samples in the water quenched condition, following the austenitising heat treatment, had a lath martensite microstructure, with prior austenite grain size of $\sim 100 \mu\text{m}$ (mean linear intercept, see Ref. [184]). Fig. 8.3 represents TEM images of the martensite microstructure for water-quenched (a) P-doped 2.25Cr1Mo steel and (b) Sn-doped 2.25Cr1Mo steel. TEM micrographs for the irradiated and unirradiated samples are shown in Figs. 8.4 (P-doped 2.25Cr1Mo steel) and 8.5 (Sn-doped 2.25Cr1Mo steel), indicating that no apparent difference of microstructure between them. The microstructure of the irradiated and unirradiated samples is characterised by the tempered martensite. FEGSTEM images of the typical grain boundary analysed are shown in Fig. 8.6 (P-doped 2.25Cr1Mo steel) and 8.7 (Sn-doped 2.25Cr1Mo steel), demonstrating that no precipitate appears along the grain boundary and that the grain boundary is well parallel to the electron beam, which is necessary for FEGSTEM microanalysis.

8.8.2. Measured results

The results of the FEGSTEM grain boundary microanalysis are presented clearly in Table 8.2 and more clearly in Figs. 8.8-8.13. For P, Sn and Cr, there appear no apparent radiation effects. Their boundary concentrations have not obviously changed under irradiation. For the P-doped 2.25Cr1Mo steel, the boundary levels of P and Cr are about 2.0 and 3.6 at%, respectively. For the Sn-doped 2.25Cr1Mo steel, the boundary levels of Sn and Cr are about 0.2 and 3.6 at%, respectively. For Mo, there is a certain radiation effect. Its boundary concentration has, to some extent, reduced under irradiation. The boundary concentrations of Mo are about 2.0 and 3.2 at% respectively for the irradiated and unirradiated P-doped 2.25Cr1Mo

steel samples, and about 1.9 and 2.6 at% respectively for the irradiated and unirradiated Sn-doped 2.25Cr1Mo steel samples. In addition, no noticeable segregation of silicon and nickel was observed in the present work.

Therefore, for oversized solutes Sn, Mo, and Cr (here impurity is also called solute), there are no apparent radiation effects except for Mo. Mo has some radiation effect with a decrease in segregation level under irradiation. As reviewed above, the grain boundary is depleted in most of oversized solutes under irradiation. However, this depletion phenomenon was not clearly seen in the present work. This may be because the neutron dose used here is not high enough, i.e. the irradiation time is not long enough, to result in significant radiation effects. For undersized solute P, in terms of previous work there should be a considerable radiation effect. Nevertheless this was also not found in this work. The phenomenon may also be believed to be due to not high enough neutron doses. Furthermore, it may be seen from the predictions in Chapter Seven that for radiation-induced phosphorus segregation, the segregation transition temperature is in the range of 250-300 °C. In the present work, the irradiation temperature (see Fig. 8.1) is just in this range. This could give some interpretation for the experimental results presented above. More discussion on this will be given in Section 7.8.4. The measured profiles for P, Sn Mo and Cr are illustrated in Figs. 8.14-8.25, showing the same segregation trends as those presented above. The segregation levels exhibited for P, Sn and Cr may be believed to be caused mainly by quenching because at temperatures below 300 °C thermal segregation magnitude is very low.

It should be recognised that the value of the experimental measurement for the grain boundary segregation using the X-ray microanalysis technique is determined by the following factors: (i) the probe size; (ii) the grain boundary orientation; (iii) the overall stability and accuracy of the location of the analysing electron beam; and (iv) the magnitude and spatial extent of the segregant profile. Nevertheless, apart from these parameters there is a variability of segregation concentration due to the specific orientation of the particular grain boundary selected for microanalysis. this has been thought of recently by Laws and Goodhew [185] with respect to chromium depletions observed in a sensitised austenitic stainless steel. The concentration at a given grain boundary will depend on the overall misorientation but there is clearly an enhancement for specific orientations that result in those termed, special grain boundaries. In microanalysis, grain boundaries were selected that had the capability to be oriented parallel to the analysing electron beam combined with that to produce larger X-ray signal with respect to elements of

interest. As a consequence, for this particular microanalysis technique the selection of the grain boundaries is limited. This may affect the measured results.

8.8.3. Correction of the measured results

The widths of the segregated layers as measured by the widths at half maximum of the profiles acquired by the FEGSTEM are 3-4 nm. Although narrow, this width is still clearly greater than that of the actual enrichment layer (~ 1 nm). This arises due to the finite size of the incident electron probe. The use of a finite size probe smooths out a discontinuous solute distribution. The greater the probe diameter, the more smoothed the true distribution becomes.

Faulkner et al. [186] established an analytical convolution method to quantify the true solute grainboundary segregation. The application of it in Ref. [186] demonstrated that it worked very well. This approach is to convolute an assumed incident electron probe current distribution with an assumed segregant distribution and neglect beam-broadening effects produced by high-angle elastic scattering of electrons as they negotiate the thin foil. Consequently, it may provide a measure of the best profile which could be generated by the geometric interaction of the electron probe and segregant distributions. The interfaces analysed in this work were chosen as being sited at very thin regions of the foil, where beam-broadening effects could not be significant. Hence this approach may be applied to model analytically the interaction; if beam-broadening is significant, it will show up in comparison of the measured results with the modelling.

The electron probe current is assumed to be radially normally distributed, with a mean of zero [i.e. centred at (0,0)] and a variance represented by σ^2 . For a solute distribution of concentration C_b in the segregated layer and C_o in the adjacent matrix, the derived concentration, C , generated from an electron probe incident at a distance x_d from the centre of a segregated layer of width d_o (see Fig. 8.26), is given by [186]

$$C = C_o + \frac{1}{2}(C_b - C_o) \times \left[\operatorname{erf}\left(\frac{x_d + \frac{1}{2}d_o}{\sigma\sqrt{2}}\right) - \operatorname{erf}\left(\frac{x_d - \frac{1}{2}d_o}{\sigma\sqrt{2}}\right) \right] \quad (8.7)$$

For a fixed width of segregated layer, the derived concentration profile is determined by the standard deviation of the probe distribution, σ . The probe diameter is usually defined by a diameter containing 80% of the total probe current. The relationship between the standard deviation of the normal approximation to the

electron distribution (s) and the beam diameter containing 80% of the current (ϕ_{80}) is given by [186]

$$s = 0.279\phi_{80} \quad (8.8)$$

Equation (8.7) may be used in conjunction with Equation (8.8) to determine the true grain boundary concentration of the solute.

To obtain the true segregation level of the solute, it is necessary to determine a series of the derived concentration profiles across the boundary at a series of different C_b and ϕ_{80} (see Ref. [186]). When the derived concentration profile is well consistent with the measured one, the corresponding C_b should be the true grain boundary concentration of the solute. In this work, the concentration of the adjacent matrix of the segregated layer, C_o , was taken to be the bulk concentration.

The analytically derived concentration profiles for phosphorus for a series of different C_b and ϕ_{80} at a segregated layer thickness of 1 nm are shown in Fig. 8.27 for the irradiated P-doped 2.25Cr1Mo steel. The mean data obtained experimentally from either side of the prior austenite grain boundary are also plotted for comparison. It may be seen that the boundary concentration (C_b) and the probe size (ϕ_{80}) at which the derived concentration profile is best coincident with the measured result are about 4.0 at% and 3 nm, respectively. As a consequence, the true grain boundary concentration of phosphorus in the irradiated P-doped 2.25Cr1Mo steel sample should be about 4.0 at%, respectively, instead of the value acquired by FEGSTEM microanalysis. It is clear here that the effective probe size is greater than the nominal incident beam diameter of approximately 1 nm. This arises mainly from beam spreading in the thin foil.

There is a limit to the distance apart that two microanalysis readings can be taken before one reading overlaps the adjacent one. This is generally the concept of the spatial resolution for microanalysis. The value is substantially less than the 1-2 μm figure that is routinely expected for bulk microanalysis in scanning electron microscopy [187]. The commonly accepted spatial resolution in thin foil microanalysis is the initial probe size plus the amount of beam-spreading in the thin foil. The beam-spreading usually depends on the specimen thickness (t_s) that controls the amount of elastic scatter, the specimen density (ρ_s), the atomic weight (A) and the atomic number (Z) of the atoms in the interaction volume.

The simplest model developed by Reed in the classical paper by Goldstein et al. [188] assumes that from an infinitely small probe each electron undergoes a single elastic (Rutherford-type) interaction at the foil centre and it emerges over a distance b defined as the beam-spreading amount. The expression for b in cm is

$$b = 625 \cdot \left(\frac{\rho_s}{A}\right)^{1/2} \cdot \left(\frac{Z}{E_o}\right) \cdot t_s^{3/2} \quad (8.9)$$

where E_o is the operating voltage in KV, ρ_s is in $\text{g} \cdot \text{cm}^{-3}$, and t_s is in cm. Arbitrarily this distance is taken to encompass 90% of the scattered electron trajectories and therefore 90% of the generated X-rays. It has been shown [187] that Equation (8.9) is as good an estimate of beam-spreading as any other.

It has been experimentally demonstrated [184] that at very thin regions of the specimen the thickness is about 30 nm. as a result, the beam-spreading amount in the iron matrix may be obtained as ~ 3.1 nm for the operating voltage of 100 KV. It may be believed from the above discussion that the corrected results on the grain boundary concentration are reasonable.

The analytically derived concentration profiles for molybdenum and chromium that fit best with the experimental results for the effective probe size of 3 nm are illustrated in Figs. 8.28 and 8.29 respectively for the irradiated P-doped 2.25Cr1Mo steel sample. It is demonstrated that there appears a general agreement between the experimental and derived results. The true grain boundary concentrations of molybdenum and chromium could be about 3.0 and 5.2 at%, respectively.

In addition to beam-broadening, the assumption of a top-hat function of width 1 nm to approximate the segregated layer thickness may be not strictly valid. It is generally believed [51] that the grain boundary thickness is 2-3 atom layer thickness which may be up to a maximum of 1 nm. Actually, the thickness of the grain boundary depends on the misorientation between two grains on both sides of it and is in the range of 0.5~1 nm [189]. The maximum value of 1nm was adopted in the present work.

In order to further demonstrate that the segregation levels exhibited for P, Sn and Cr may be believed to be caused mainly by quenching, we have predicted the phosphorus segregation level during quenching by using the model developed by Xu and Song [69]. Data used in the theoretical calculation are listed in Table 8.3. The determination procedure of some data is discussed as follows.

The formation of a vacancy-solute complex is accomplished by bringing together an isolated vacancy and solute atom to nearest neighbour sites. The binding energy for the complex is the free energy difference of the lattice between the two states. The complex binding energy has been evaluated in Chapter Six and the predicted value has been employed in calculations.

The coefficient for diffusion of vacancy-solute complexes in the matrix is generally unavailable and need to be evaluated. As discussed in Section 5.4.1, there are two ways for migration of vacancy-solute complexes, namely the dissociation mechanism and the non-dissociation mechanism. The former is a more plausible mechanism for migration of the complexes because the latter requires to overcome a high potential barrier. The migration energy is given by the vacancy migration energy plus the vacancy-solute binding energy. This energy has been employed in the present work (see Table 8.3). It is assumed here that the diffusion coefficient of P-vacancy complexes in the matrix is given by the product of the pre-exponential constant for P diffusion and the exponential term containing the complex migration energy defined above.

The theoretical treatment for segregation during quenching requires the quenching rate. This value is also unavailable. For Newtonian conditions, the temperature as a function of cooling time, is approximately given by [191]

$$T = (T_o - T_q)\exp(-\phi t) + T_q \quad (8.10)$$

where T_o is the quenching temperature, T_q is the temperature of quenching medium and ϕ is the cooling rate parameter, which is about 1 s^{-1} for water-quenching for the small sample [191].

The predicted value is ~3.6 at%. This is in reasonable agreement with the corrected value (~4.0 at%). This indicates that the segregation level exhibited for phosphorus is caused mainly by quenching indeed.

8.8.4. Comparison of the theoretical and experimental results

The predictions has been made for radiation-induced phosphorus segregation to grain boundaries. Here the predicted temperature dependence of phosphorus segregation is illustrated in Fig. 8.30 for the neutron dose rate of $1.05 \times 10^{-8} \text{ dpa/s}$ and the neutron dose of 0.042 dpa. Little segregation has been predicted in the

range of 250-300 °C. The experimental results presented above indicate that little segregation can be induced by irradiation under these irradiation conditions. As a consequence, there is a good fit between the experimental and predicted results.

In order to further demonstrate an agreement between the experimental and predicted results, some experimental results for a C-Mn steel from the Berkeley Technology Centre of the Nuclear Electric [192] have been used here. The predicted results have been compared with these observed data, which is shown in Table 8.4. The observed values were obtained from two weld metals with field emission gun scanning transmission electron microscopy (FEGSTEM) or Auger electron spectroscopy (AES). Table 8.4 indicates that the predictions are generally consistent with the experimental values. For the dose rate correction factor B , a value of 0.01 was utilised for 198 and 292 °C irradiation, and 0.02 for 260 °C irradiation. This is reasonable because recent studies [162] indicate that the value of B is in the range of 0.01-0.05, and it could be slightly temperature-dependent.

8.9. Summary

Grain boundary segregation of solutes in the neutron-irradiated and unirradiated (thermally aged) 2.25Cr1Mo steels doped with P and Sn was examined by means of field emission gun scanning transmission electron microscopy (FEGSTEM). Under irradiation conditions employed in the present work, radiation effects were not clearly observed for P, Sn, Cr, Si and Ni. The boundary concentrations for these elements did not clearly vary after irradiation. There appears a certain radiation effect for Mo. The boundary concentration of Mo, to some extent, reduced after irradiation.

Comparison of the experimental and predicted results was performed. A good fit was obtained between them. The predictions for phosphorus segregation during neutron irradiation indicate that there is indeed no apparent radiation effect in the range of 250-300 °C. Some experimental results from the Berkeley Technology Centre of the Nuclear Electric were also compared with the predictions. There is also a good agreement between them.

Owing to insufficiently high resolution of the technique for grain boundary composition analysis, the measured result was corrected by means of an analytical convolution method developed by Faulkner et al. [186]. The corrected phosphorus segregation level may be up to ~4.0 at% for the irradiated P-doped 2.25Cr1Mo steel. This value is nearly the same as that (~3.6 at%) predicted by the model

developed by Xu and Song [69] for quenching-induced phosphorus segregation to grain boundaries.

Appendix 8.1
Tables for Chapter Eight

Table 8.1. Chemical compositions of experimental steels.

	C	Mn	S	P	Si	Cr	Ni	Mo	Sn	As	Sb
P-doped 2.25Cr1Mo steel (wt%)	0.086	0.46	0.009	0.077	0.29	2.28	0.15	1.00	0.011	0.005	0.021
P-doped 2.25Cr1Mo steel (at%)	0.40	0.47	0.016	0.14	0.57	2.44	0.14	0.58	0.005	0.004	0.010
Sn-doped 2.25Cr1Mo steel (wt%)	0.081	0.45	0.01	0.007	0.28	2.27	0.15	1.00	0.077	0.006	0.020
Sn-doped 2.25Cr1Mo steel (at%)	0.38	0.46	0.017	0.013	0.56	2.43	0.14	0.58	0.036	0.004	0.009

**Table 8.2. Results of the FEGSTEM grain boundary microanalysis in atomic percent.
Errors are given by the standard deviation.**

	P	Sn	Mo	Cr
Unirrad. P-doped 2.25Cr1Mo steel	2.01±0.66		3.17±0.99	3.70±0.56
Irrad. P-doped 2.25Cr1Mo steel	1.98±0.44		2.00±0.78	3.64±0.42
Unirrad. Sn-doped 2.25Cr1Mo steel		0.19±0.06	2.57±0.55	3.94±0.42
Irrad. Sn-doped 2.25Cr1Mo steel		0.21±0.03	1.92±0.67	3.46±0.30

Table 8.3. Data used in predictions of P grain boundary segregation during quenching

P diffusivity, D_i (m^2s^{-1})	$2.83 \times 10^{-3} \exp(-3.03 / kT)$	[190]
P-vacancy complex diffusivity, D_c (m^2s^{-1})	$2.83 \times 10^{-3} \exp(-1.65 / kT)$	
Vacancy formation energy, E_f (eV)	1.4	[166]
Vacancy migration energy, E_m (eV)	1.24	[168]
P-vacancy binding energy, E_b (eV)	0.41	
P bulk concentration, C_g (at%)	0.14	
Grain size, R (μm)	100	
Critical time constant, δ	0.05	[67]
Quenching medium temperature ($^{\circ}\text{C}$)	20	
Grain boundary enriched layer thickness (nm)	1	

Table 8.4. Comparison of the experimental and predicted results

Material	Irradiation temp. (°C)	Bulk P content (wt%)	Irradiation condition	Observed value (at%)	Predicted value (at)
1	198	0.039	$\sim 2 \times 10^{-12}$ dpa/s 9.4×10^{-4} dpa	20	22
1	260	0.039	$\sim 2 \times 10^{-9}$ dpa/s 9.2×10^{-3} dpa	37	35
2*	292	0.040	$\sim 2 \times 10^{-9}$ dpa/s 9.5×10^{-3} dpa	42	43

* AES results; All the others obtained by FEGSTEM.

Dislocation density constant: $\rho_0 = 5.5 \times 10^{16} \text{ m}^{-2}$ for Material 1 and $1.4 \times 10^{15} \text{ m}^{-2}$ for Material 2;

Dose rate correction factor: $B = 0.01$ for 198 and 292 °C irradiation and $B = 0.02$ for 260 °C irradiation;

Vacancy concentration correction factor: $\epsilon = 0.1$;

Interstitial formation energy: $E_f^I = 3.0 \text{ eV}$;

Grain size: $R = 20 \text{ }\mu\text{m}$.

It is assumed in the calculation that the Bulk P concentration is 0.072 at%.

Appendix 8.2
Figures for Chapter Eight

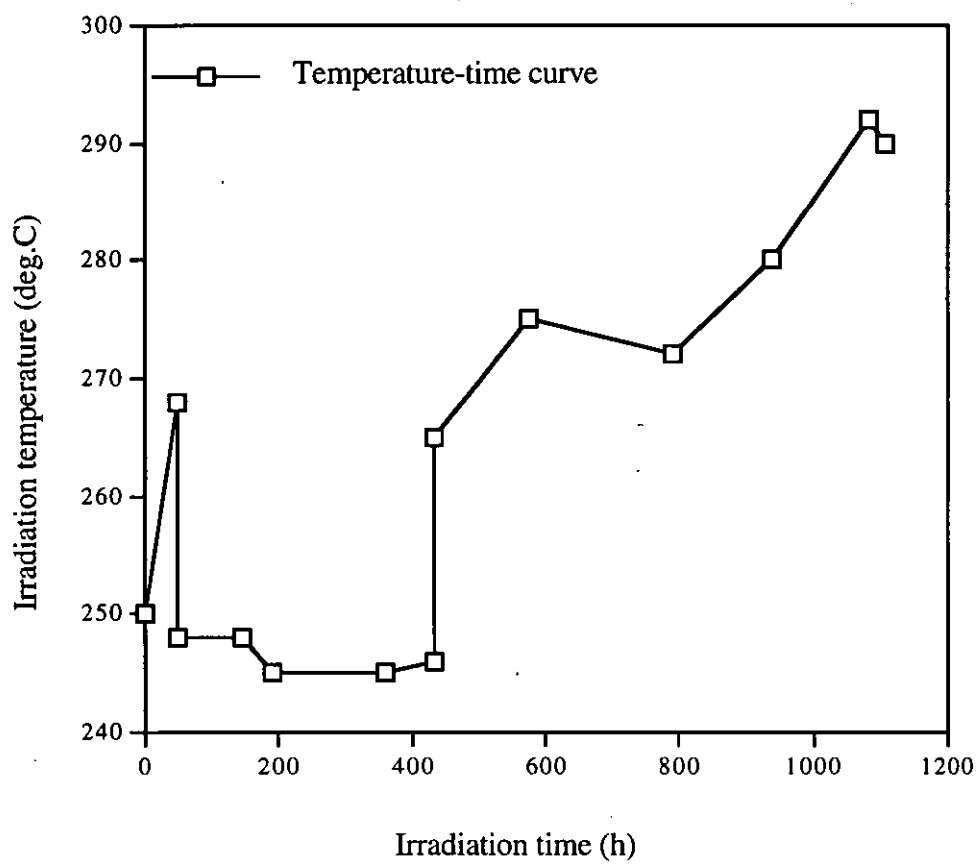


Fig. 8.1. Irradiation temperature as a function of irradiation time.

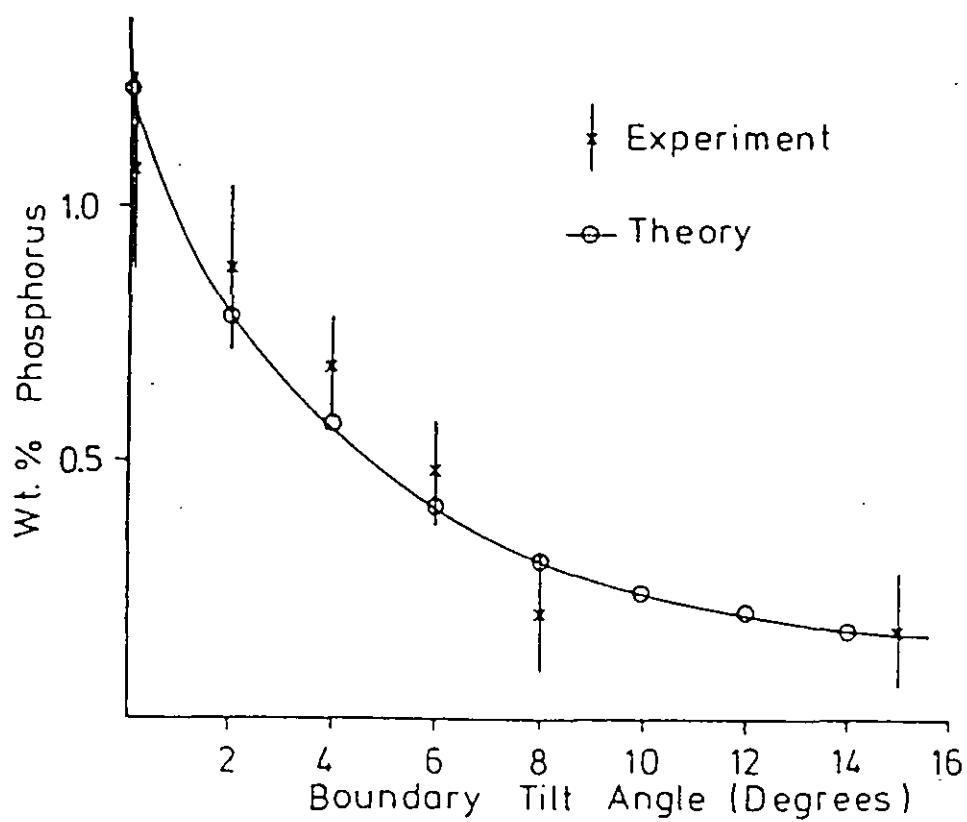


Fig. 8.2. Effect of boundary tilt on the predicted and experimental phosphorus concentrations determined at the boundary in a 2.25Cr1Mo steel [182].

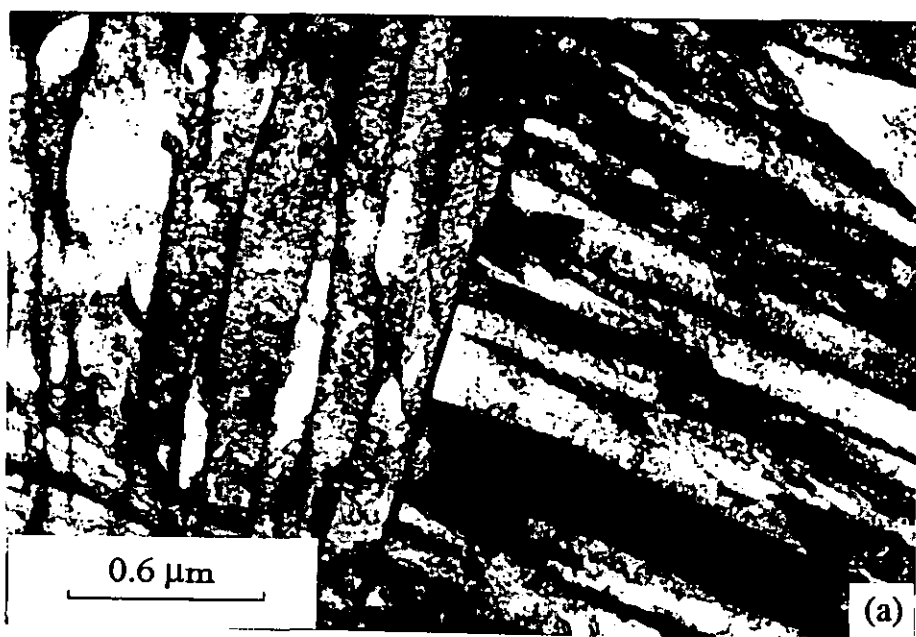


Fig. 8.3. TEM images of the martensite microstructure for water-quenched (a) P-doped 2.25Cr1Mo steel and (b) Sn-doped 2.25Cr1Mo steel.

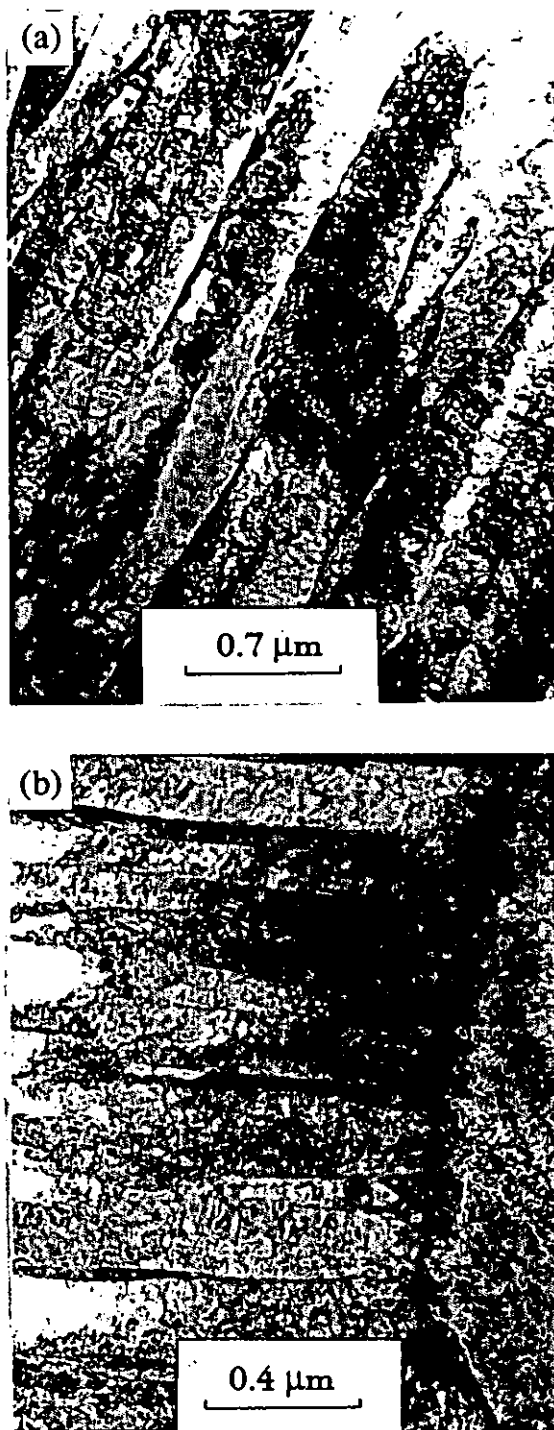


Fig. 8.4. TEM micrographs for the (a) irradiated and (b) unirradiated P-doped 2.25Cr1Mo steel samples, showing the tempered martensite microstructure.

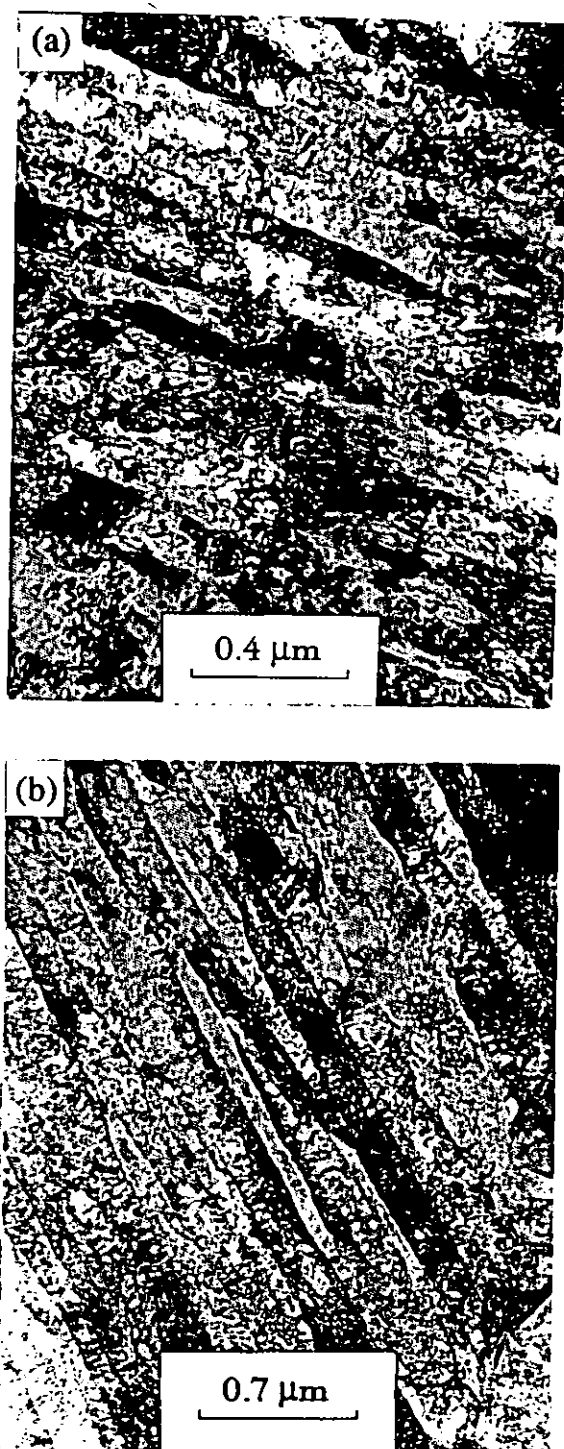


Fig. 8.5. TEM micrographs for the (a) irradiated and (b) unirradiated Sn-doped 2.25Cr1Mo steel samples, showing the tempered martensite microstructure.

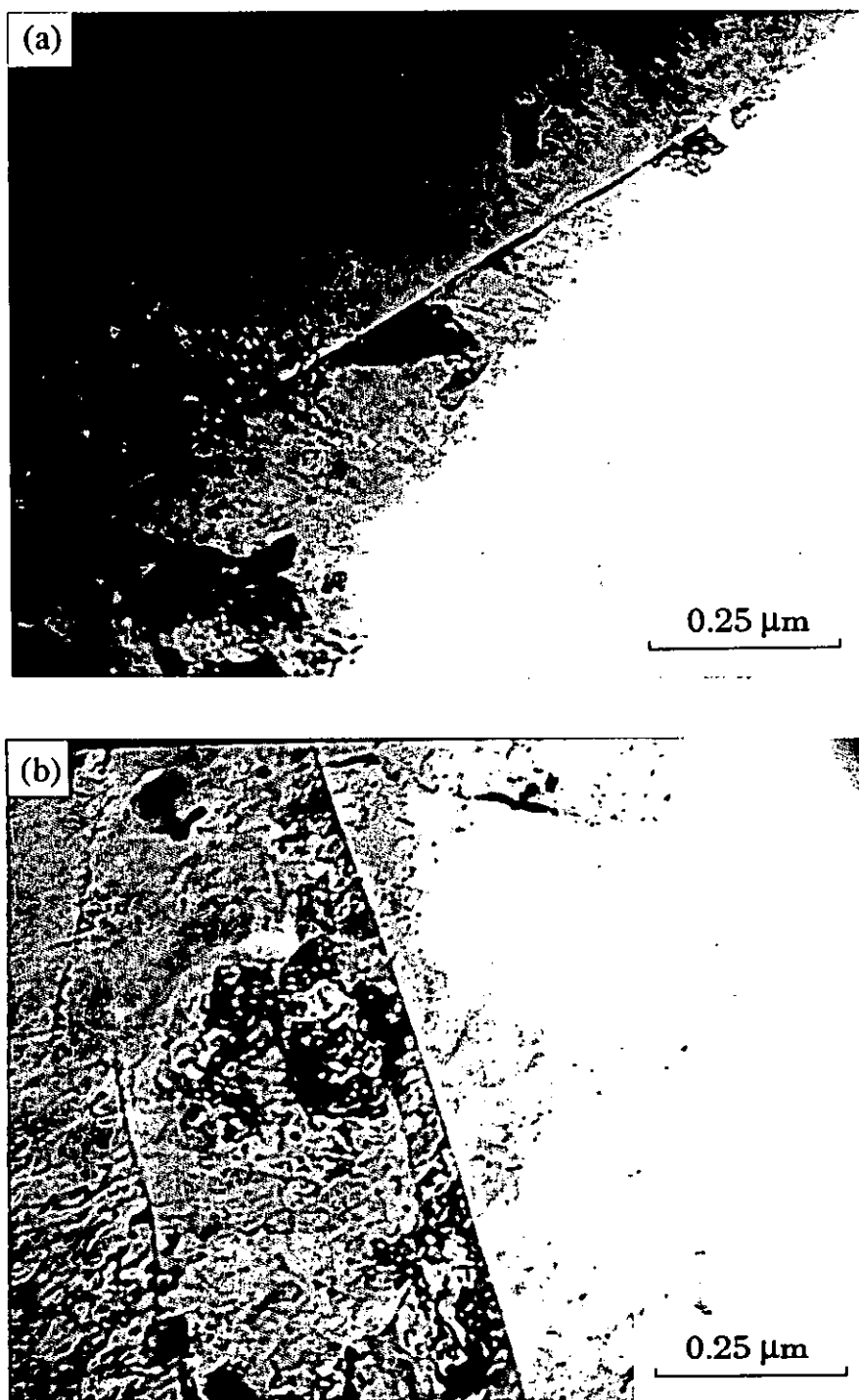


Fig. 8.6. FEGSTEM images of the typical grain boundary analysed for the (a) irradiated and (b) unirradiated P-doped 2.25Cr1Mo steel samples.

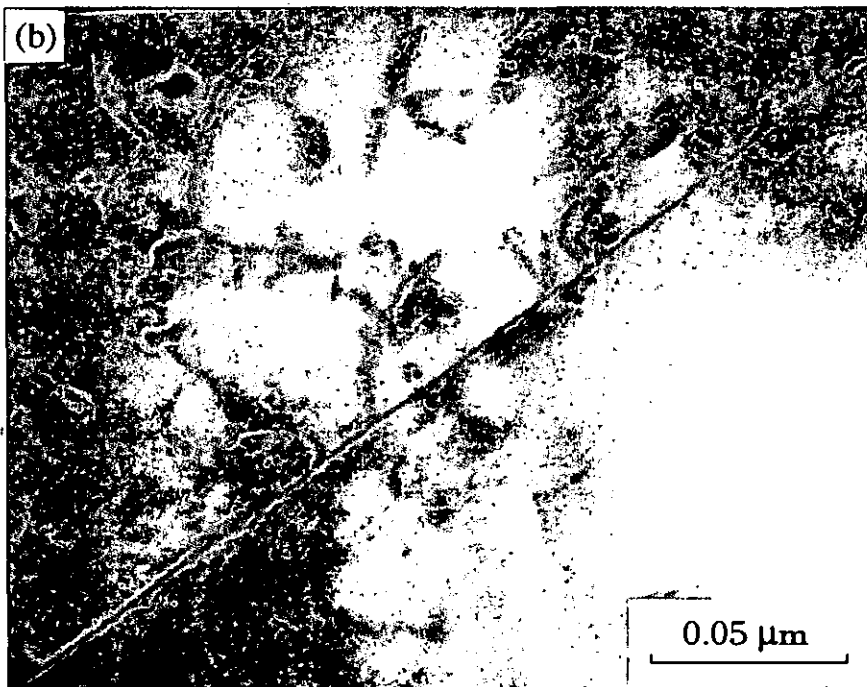
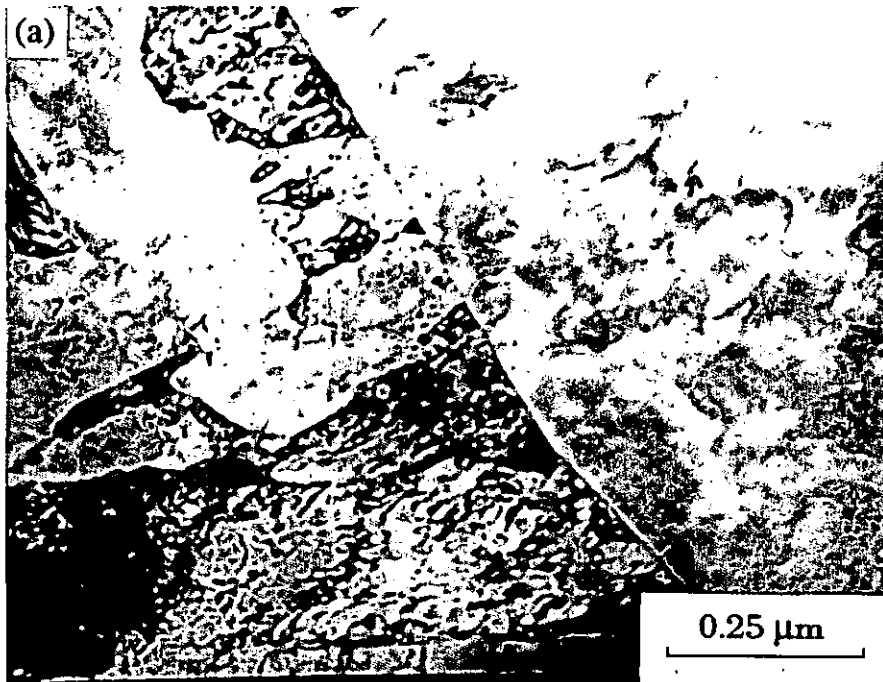


Fig. 8.7. FEGSTEM images of the typical grain boundary analysed for the (a) irradiated and (b) unirradiated Sn-doped 2.25Cr1Mo steel samples.

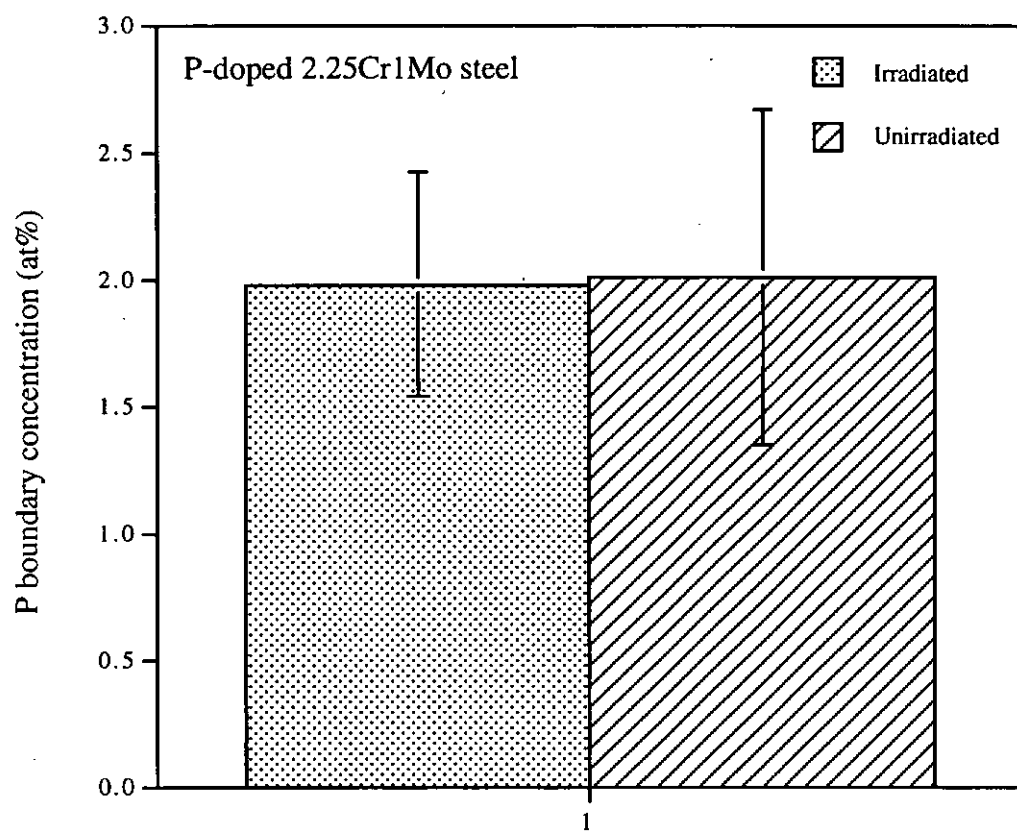


Fig. 8.8. Grain boundary P concentrations for the irradiated and unirradiated P-doped 2.25Cr1Mo steel samples, determined by FEGSTEM microanalysis.

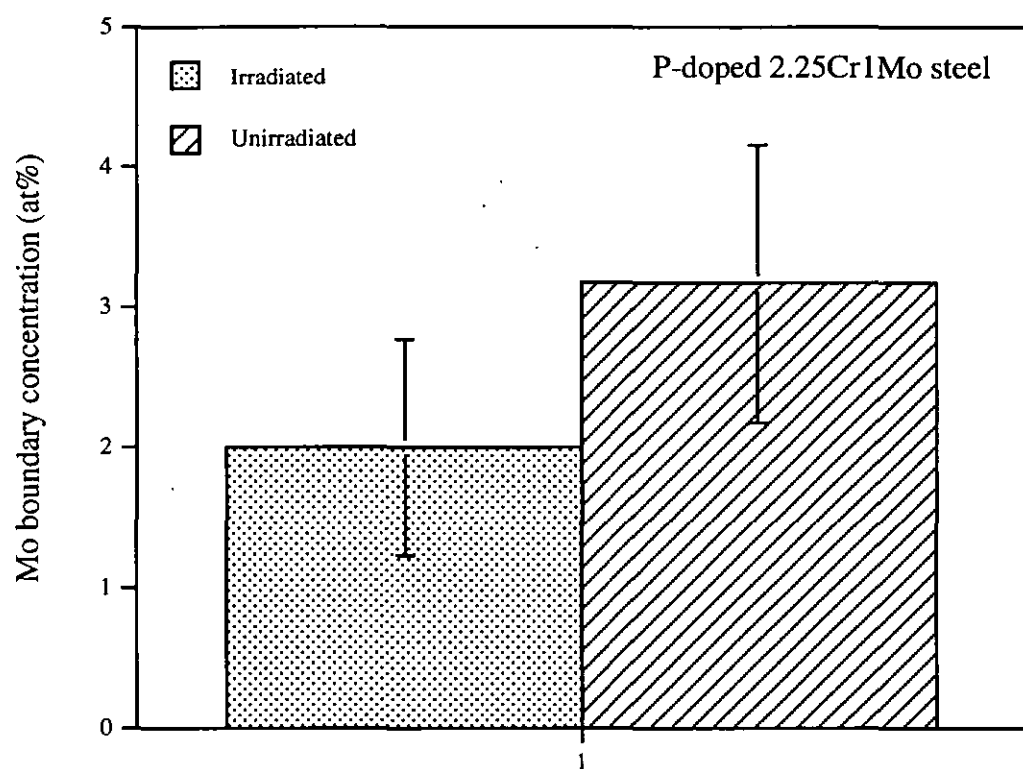


Fig. 8.9. Grain boundary Mo concentrations for the irradiated and unirradiated P-doped 2.25Cr1Mo steel samples, determined by FEGSTEM microanalysis.

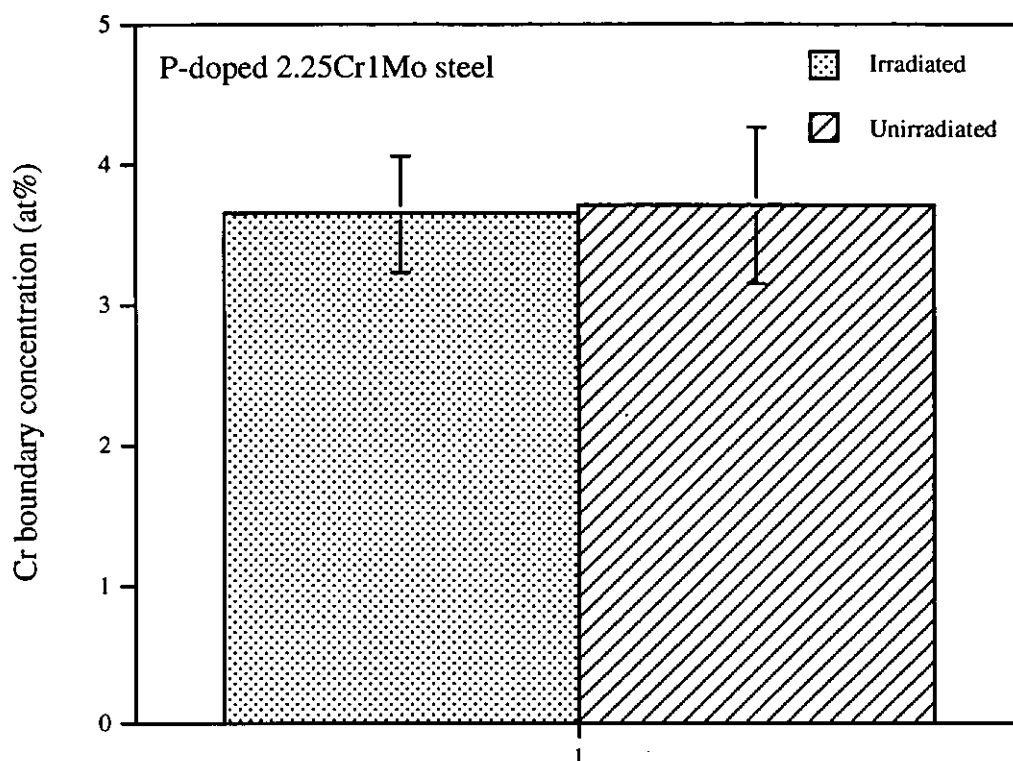


Fig. 8.10. Grain boundary Cr concentrations for the irradiated and unirradiated P-doped 2.25Cr1Mo steel samples, determined by FEGSTEM microanalysis.

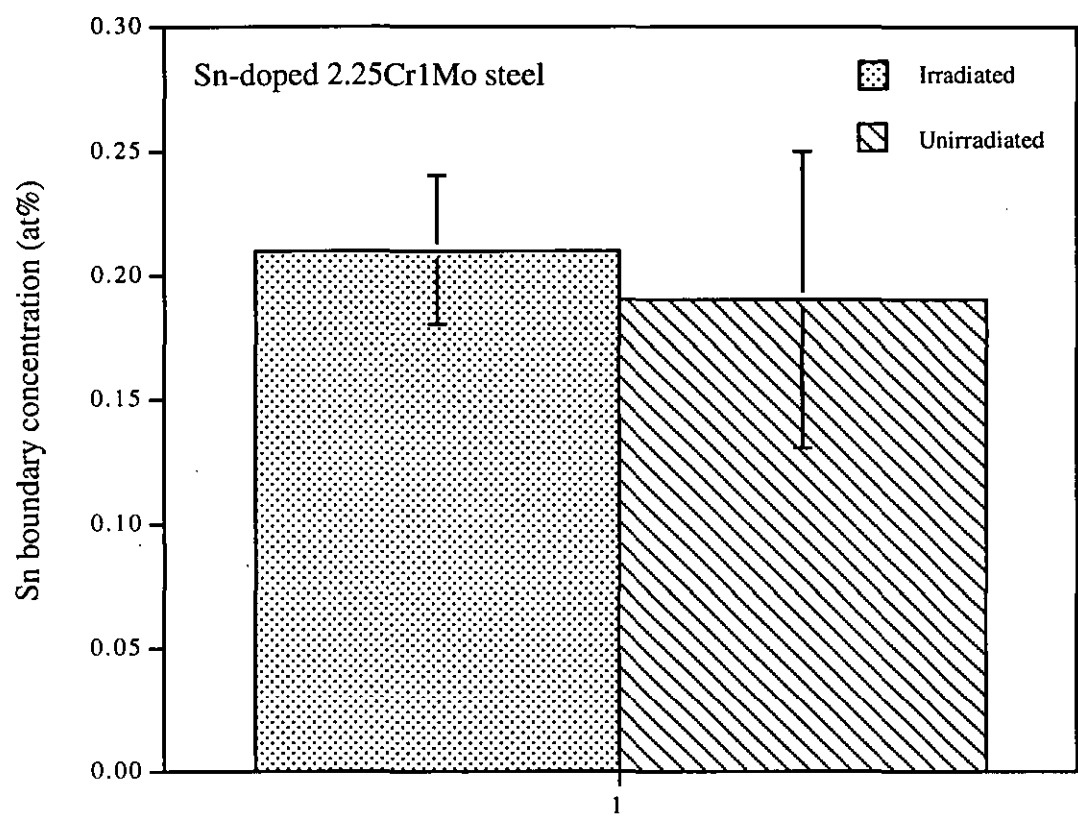


Fig. 8.11. Grain boundary Sn concentrations for the irradiated and unirradiated Sn-doped 2.25Cr1Mo steel samples, determined by FEGSTEM microanalysis.

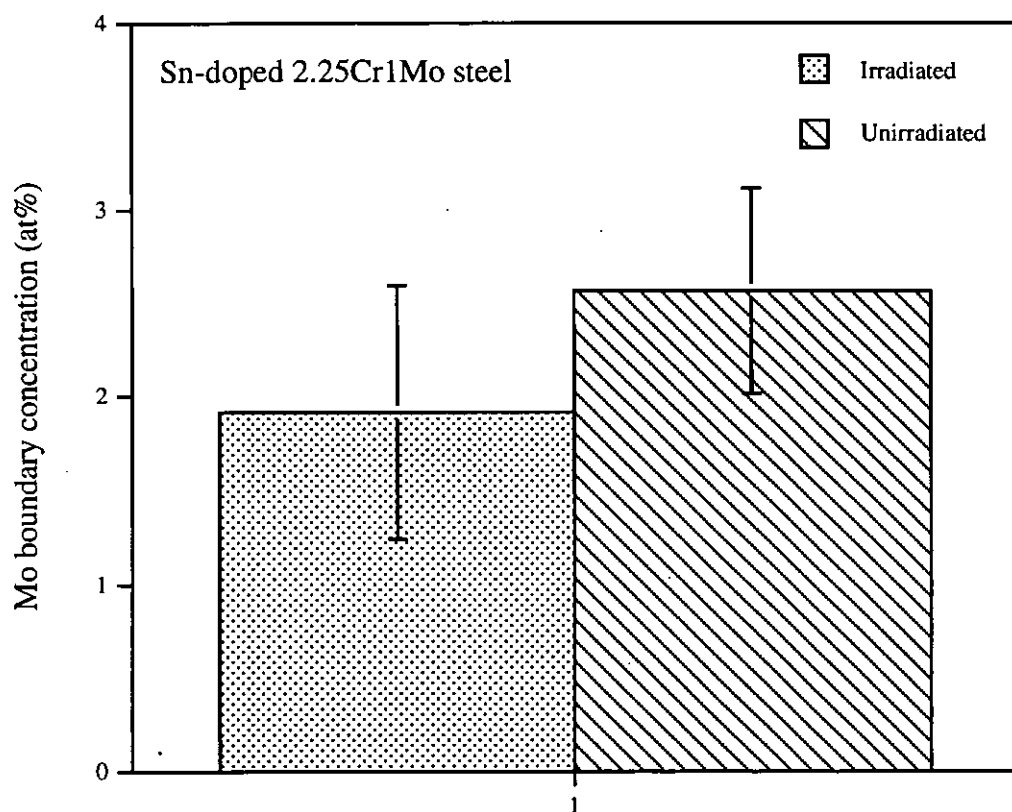


Fig. 8:12. Grain boundary Mo concentrations for the irradiated and unirradiated Sn-doped 2.25Cr1Mo steel samples, determined by FEGSTEM microanalysis.

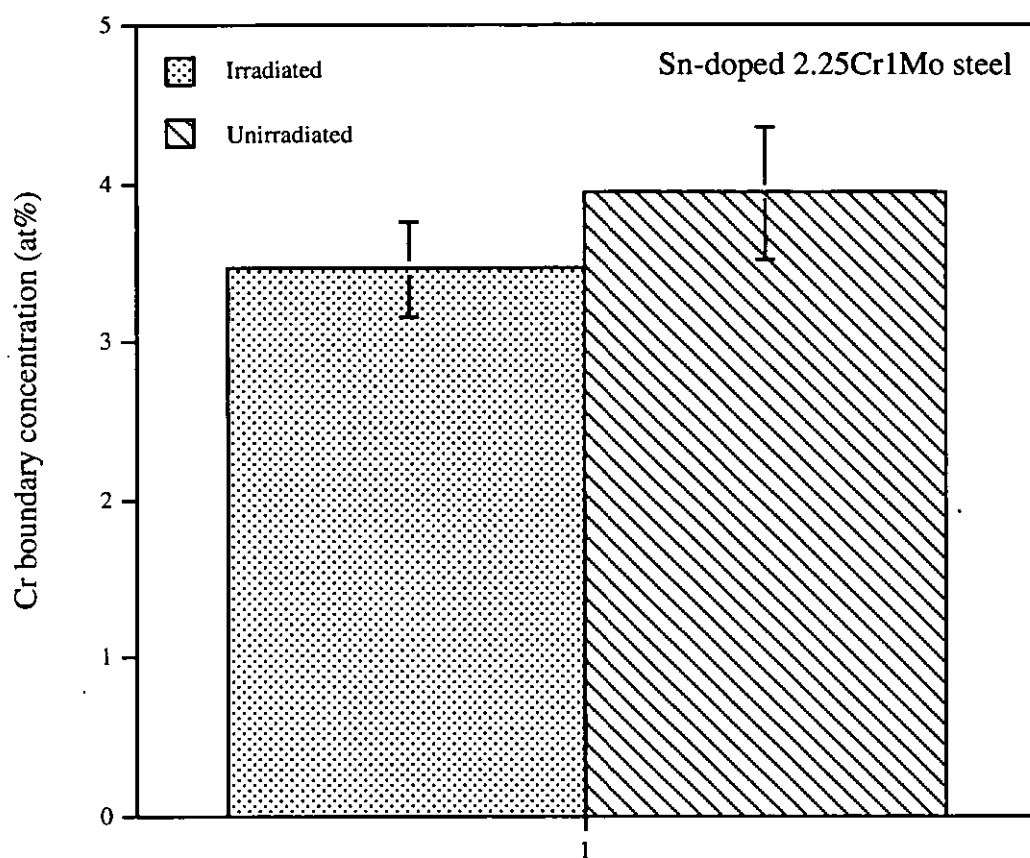


Fig. 8.13. Grain boundary Cr concentrations for the irradiated and unirradiated Sn-doped 2.25Cr1Mo steel samples, determined by FEGSTEM microanalysis.

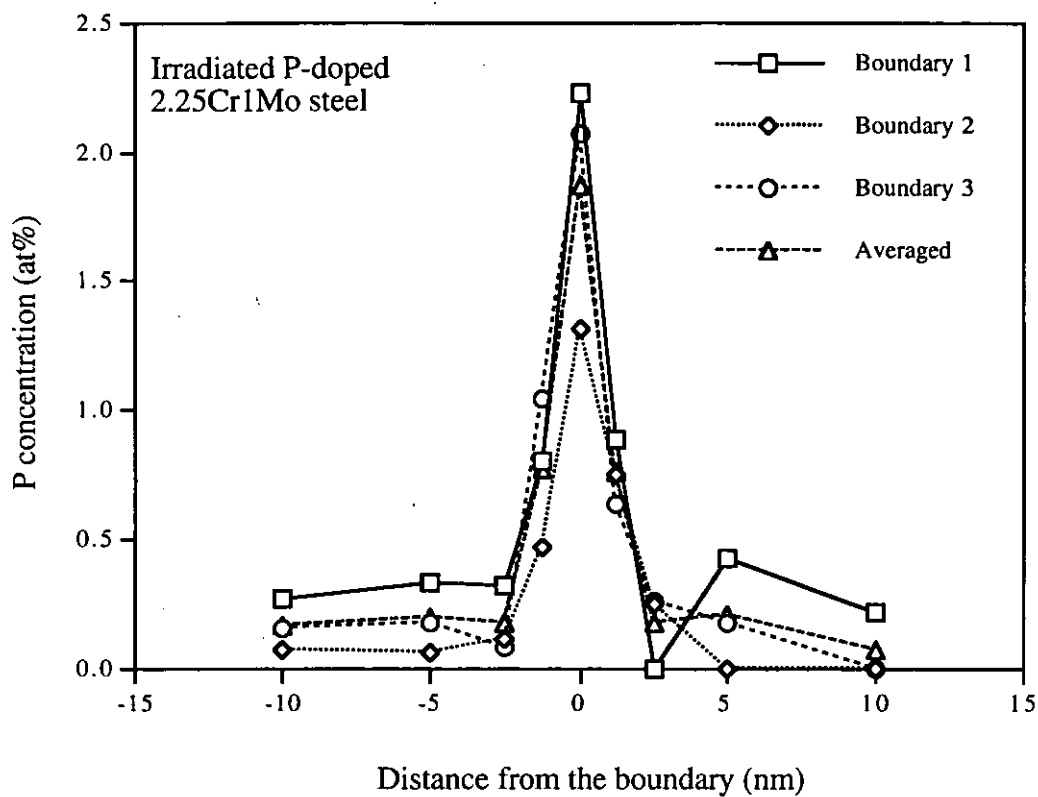


Fig. 8.14. The P profile around the grain boundary for the irradiated P-doped 2.25Cr1Mo steel sample, determined by FEGSTEM microanalysis.

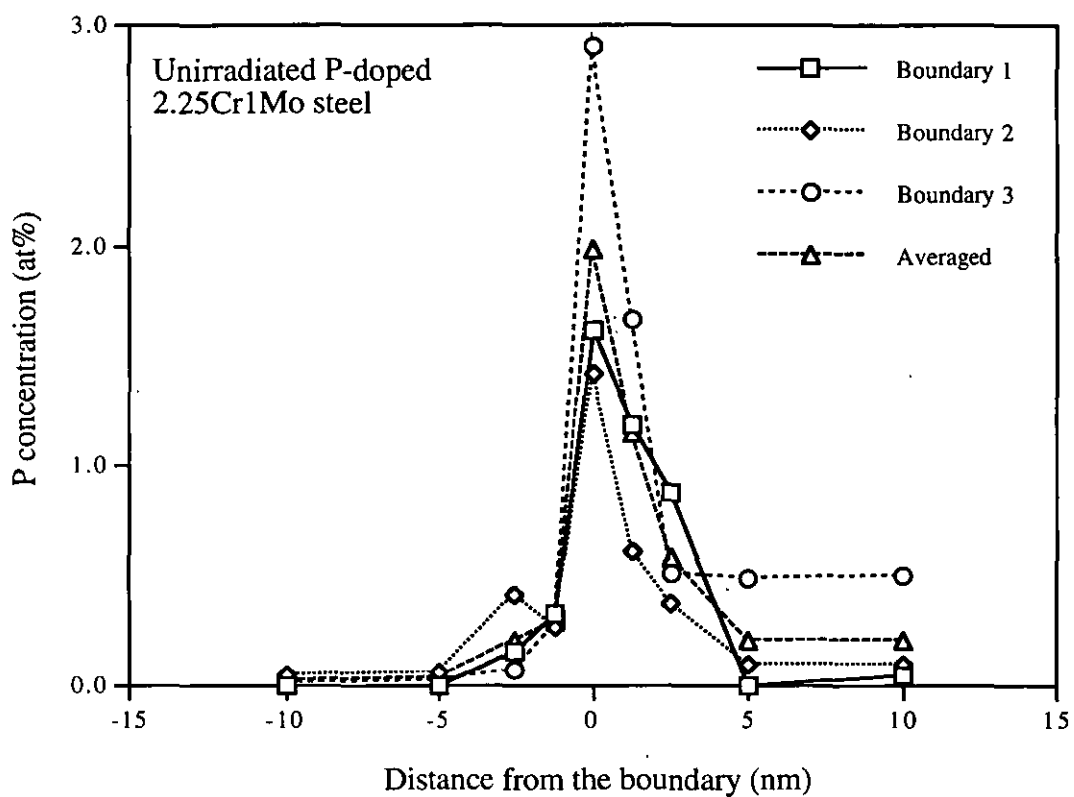


Fig. 8.15. The P profile around the grain boundary for the unirradiated P-doped 2.25Cr1Mo steel sample, determined by FEGSTEM microanalysis.

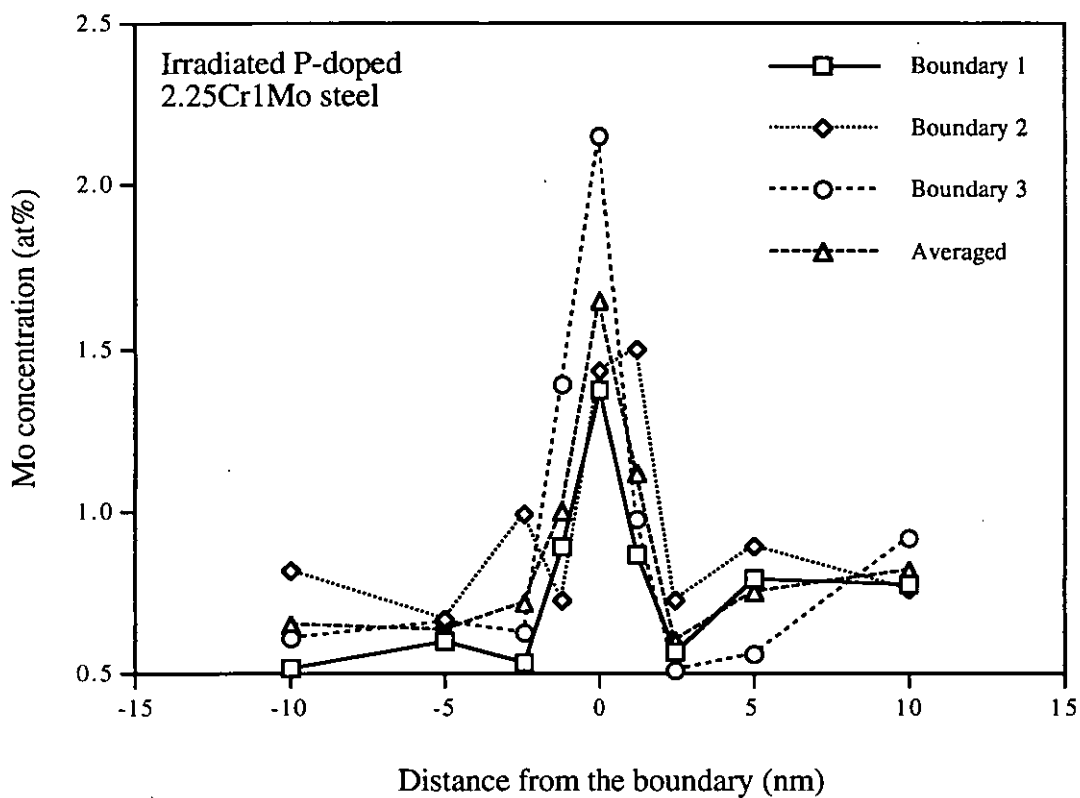


Fig. 8.16. The Mo profile around the grain boundary for the irradiated P-doped 2.25Cr1Mo steel sample, determined by FEGSTEM microanalysis.

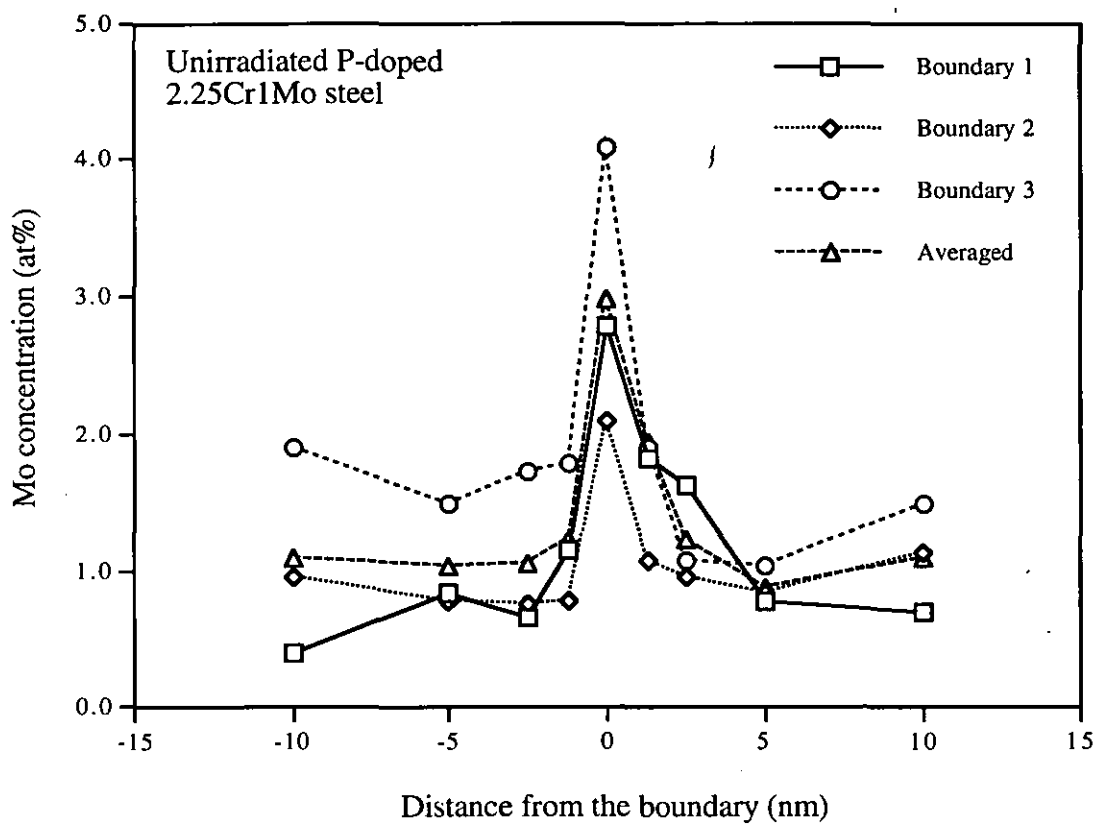


Fig. 8.17. The Mo profile around the grain boundary for the unirradiated P-doped 2.25Cr1Mo steel sample, determined by FEGSTEM microanalysis.

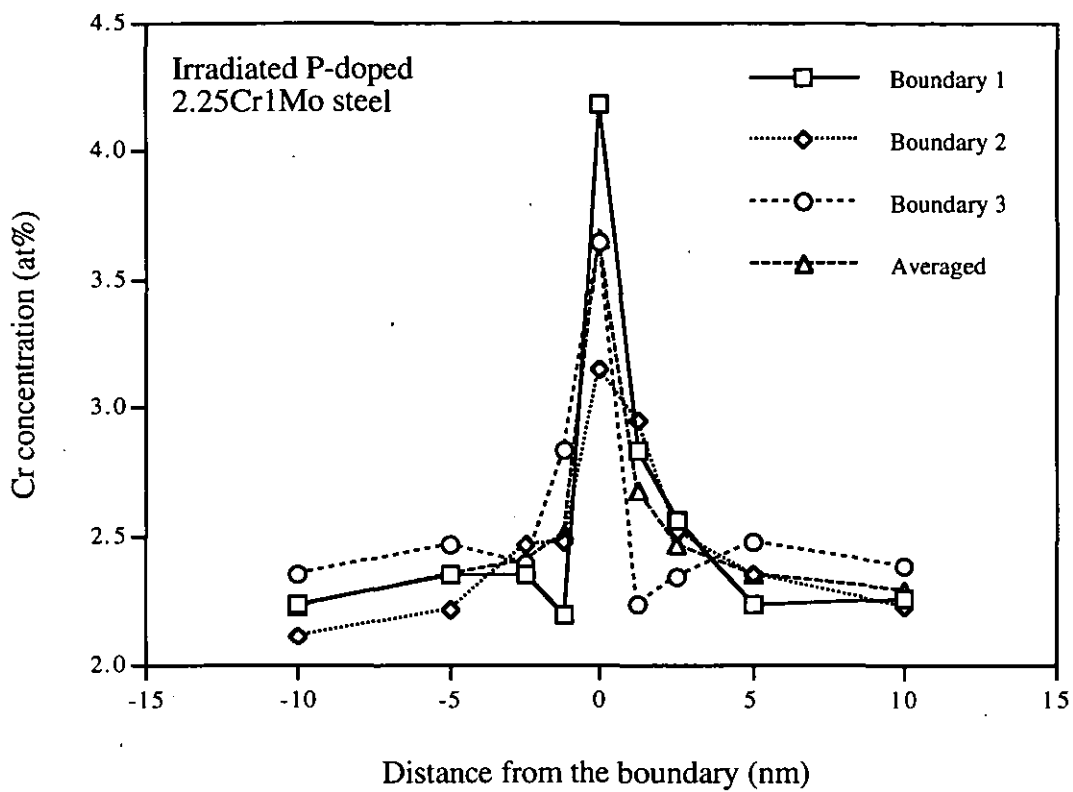


Fig. 8.18. The Cr profile around the grain boundary for the irradiated P-doped 2.25Cr1Mo steel sample, determined by FEGSTEM microanalysis.

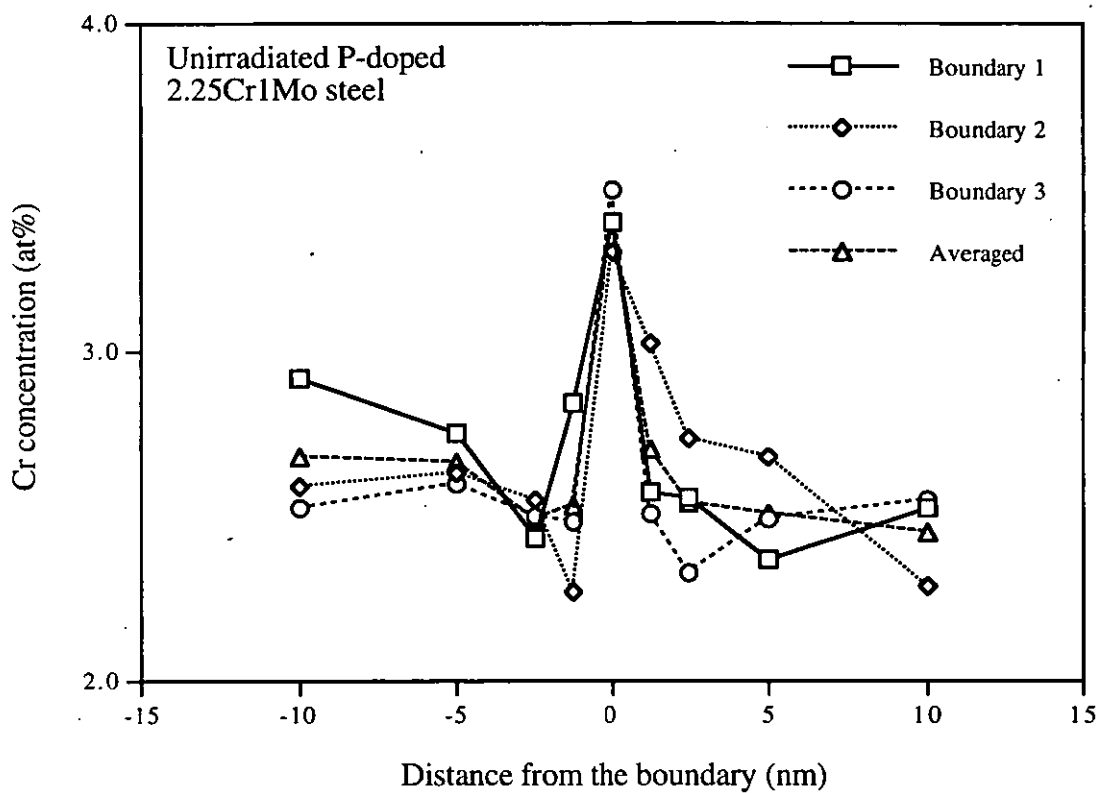


Fig. 8.19. The Cr profile around the grain boundary for the unirradiated P-doped 2.25Cr1Mo steel sample, determined by FEGSTEM microanalysis.

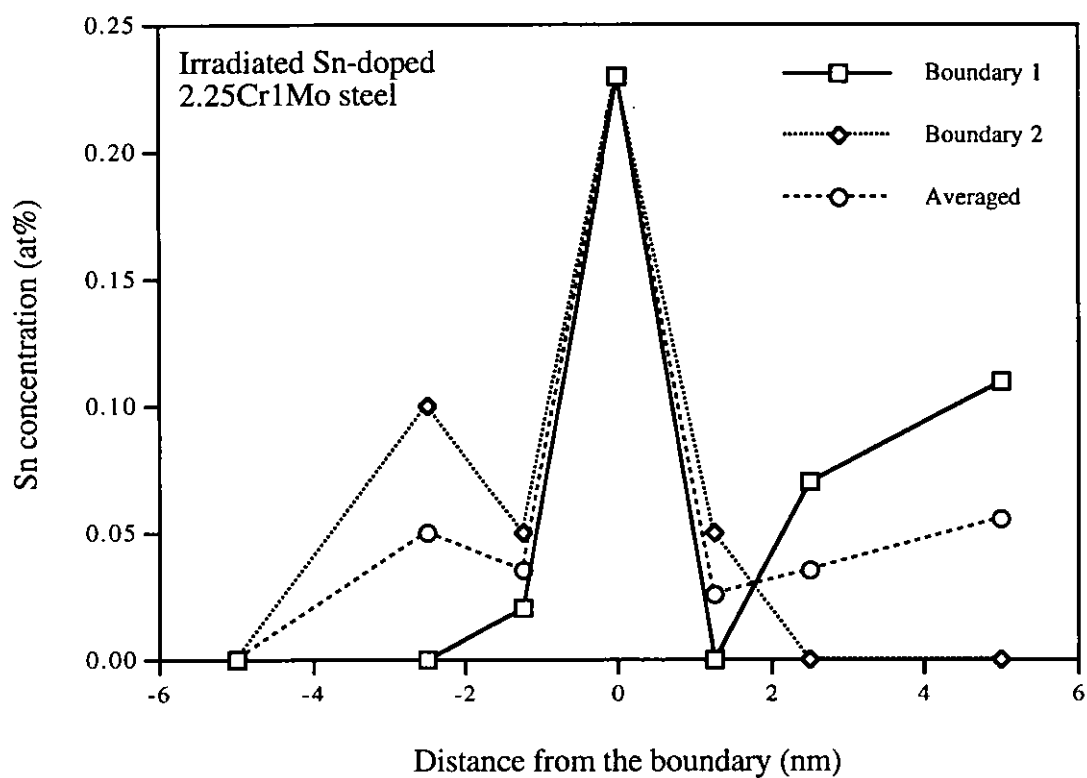


Fig. 8.20. The Sn profile around the grain boundary for the irradiated Sn-doped 2.25Cr1Mo steel sample, determined by FEGSTEM microanalysis.

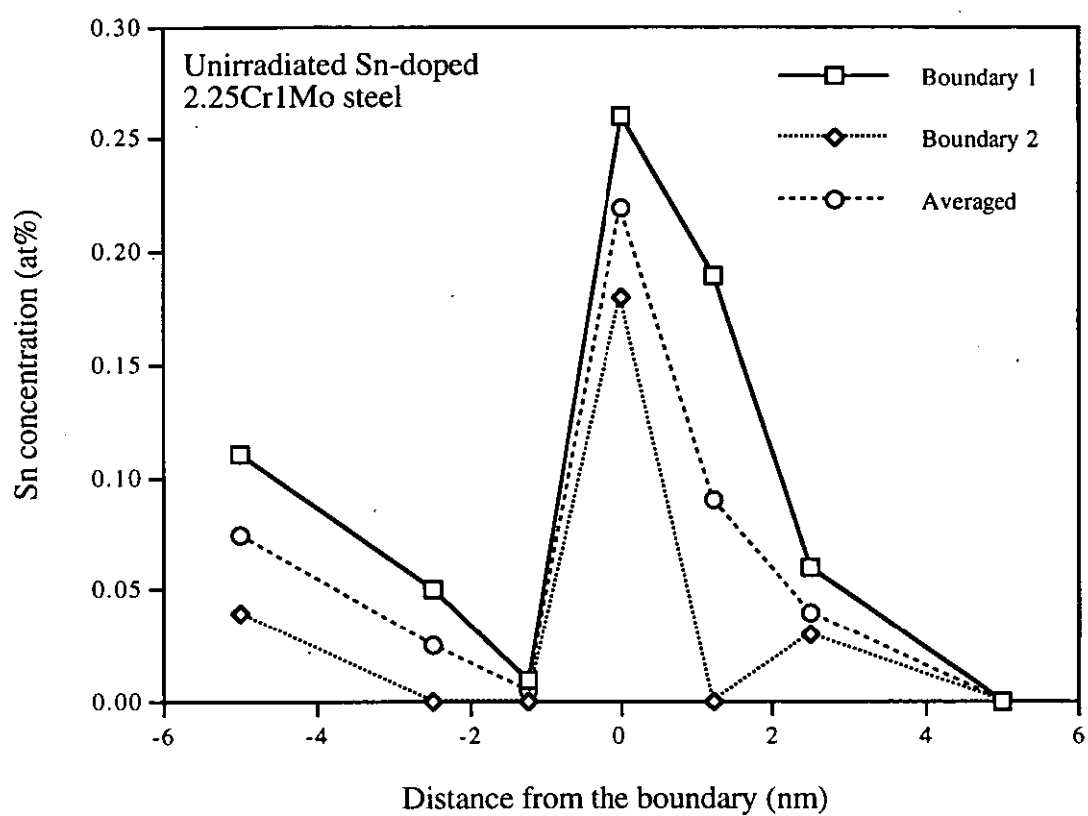


Fig. 8.21. The Sn profile around the grain boundary for the unirradiated Sn-doped 2.25Cr1Mo steel sample, determined by FEGSTEM microanalysis.

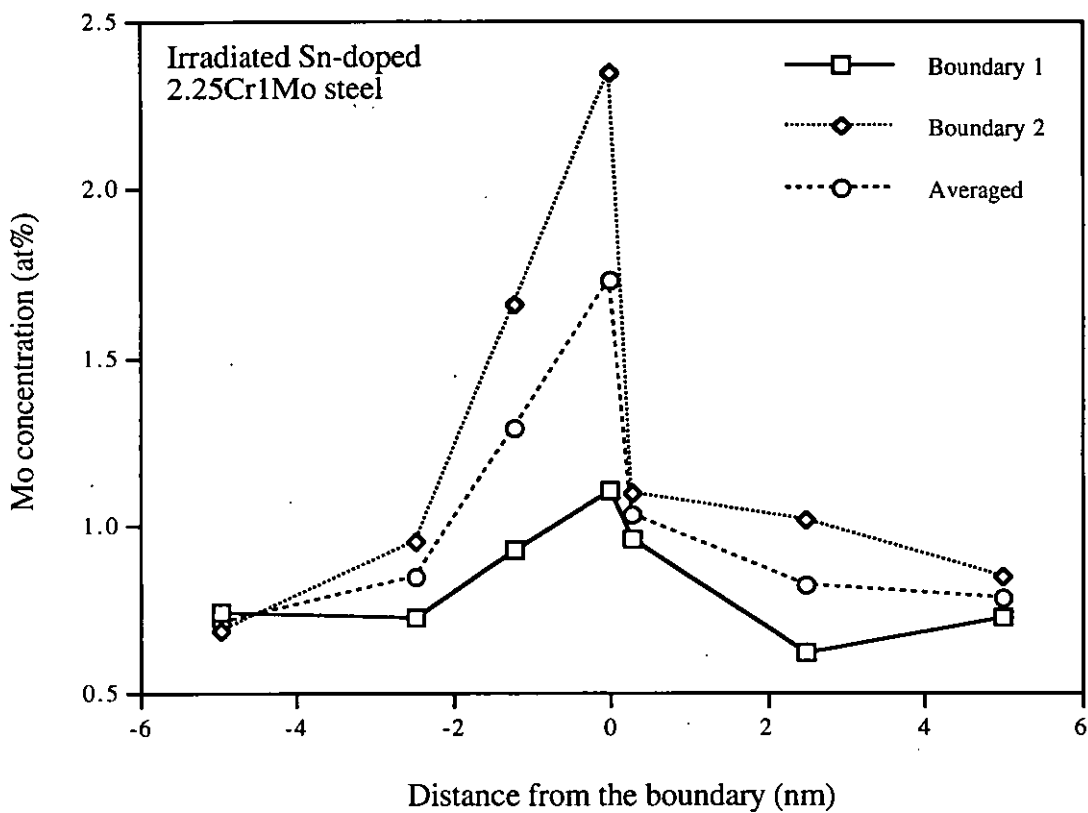


Fig. 8.22. The Mo profile around the grain boundary for the irradiated Sn-doped 2.25Cr1Mo steel sample, determined by FEGSTEM microanalysis.

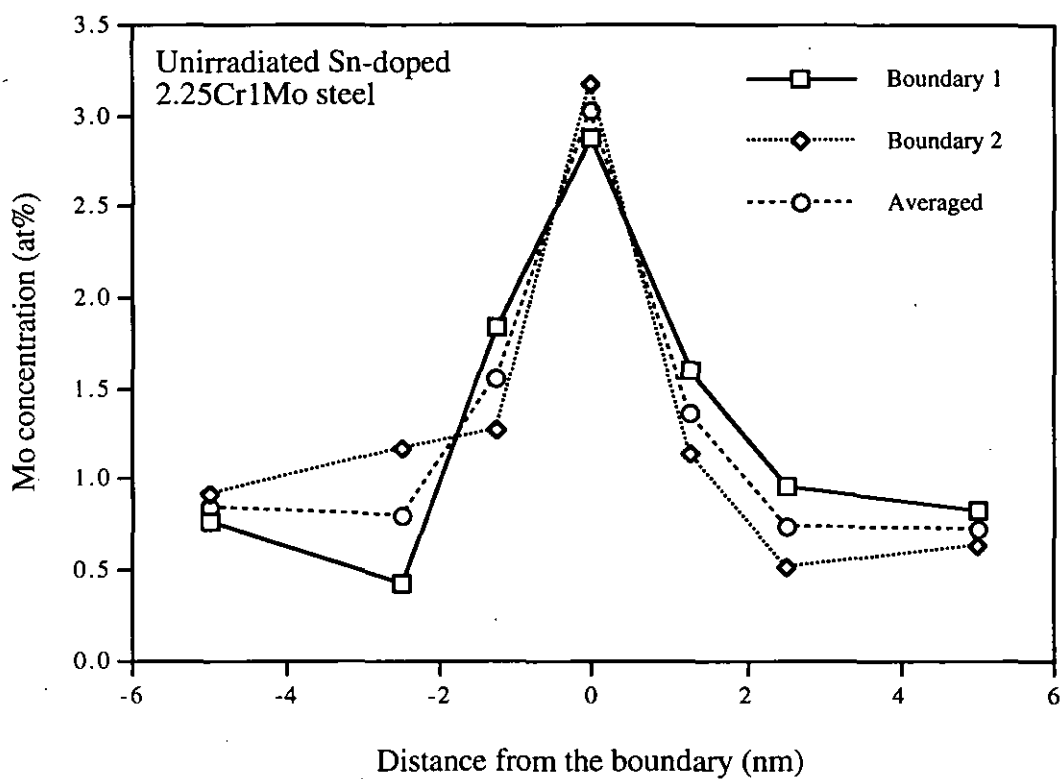


Fig. 8.23. The Mo profile around the grain boundary for the unirradiated Sn-doped 2.25Cr1Mo steel sample, determined by FEGSTEM microanalysis.

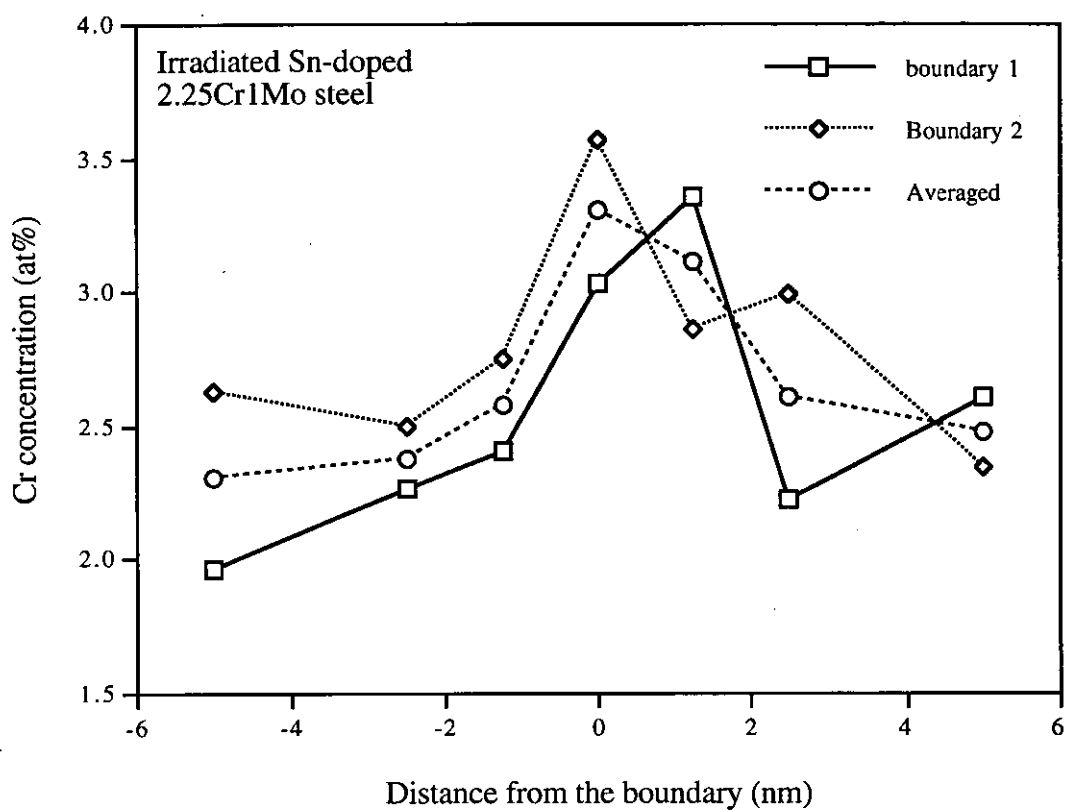


Fig. 8.24. The Cr profile around the grain boundary for the irradiated Sn-doped 2.25Cr1Mo steel sample, determined by FEGSTEM microanalysis.

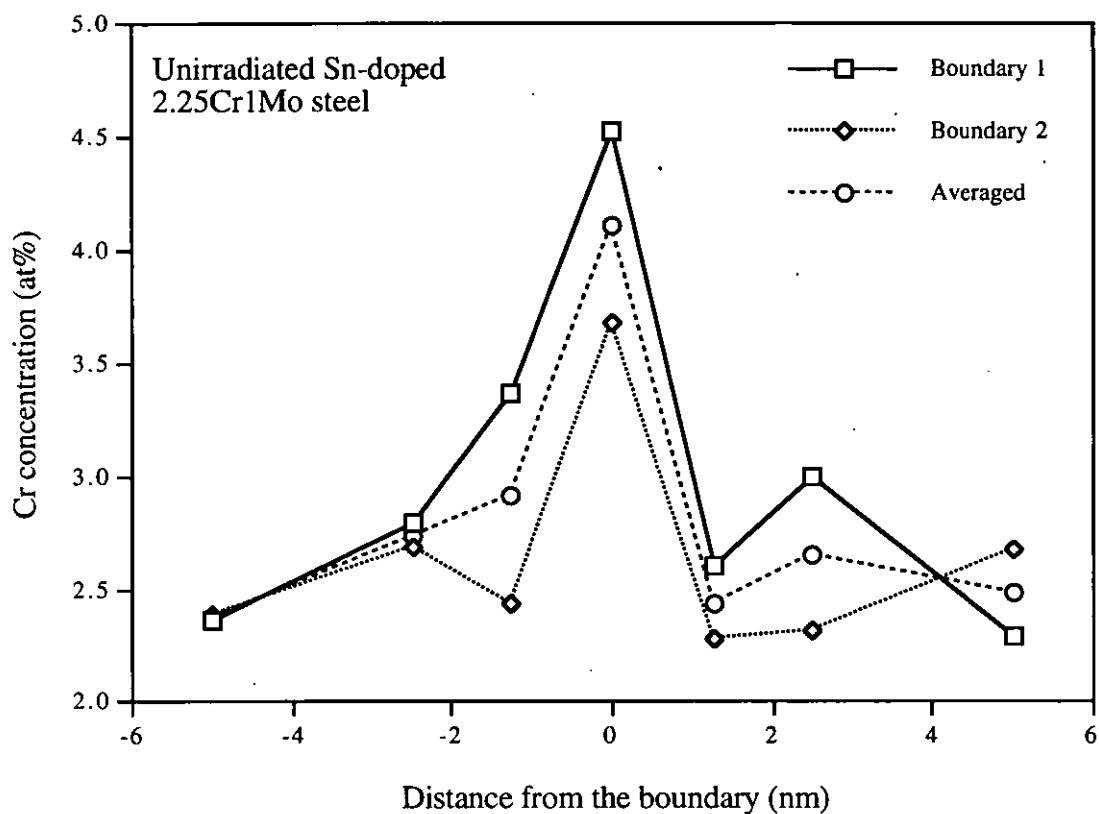


Fig. 8.25. The Cr profile around the grain boundary for the unirradiated Sn-doped 2.25Cr1Mo steel sample, determined by FEGSTEM microanalysis.

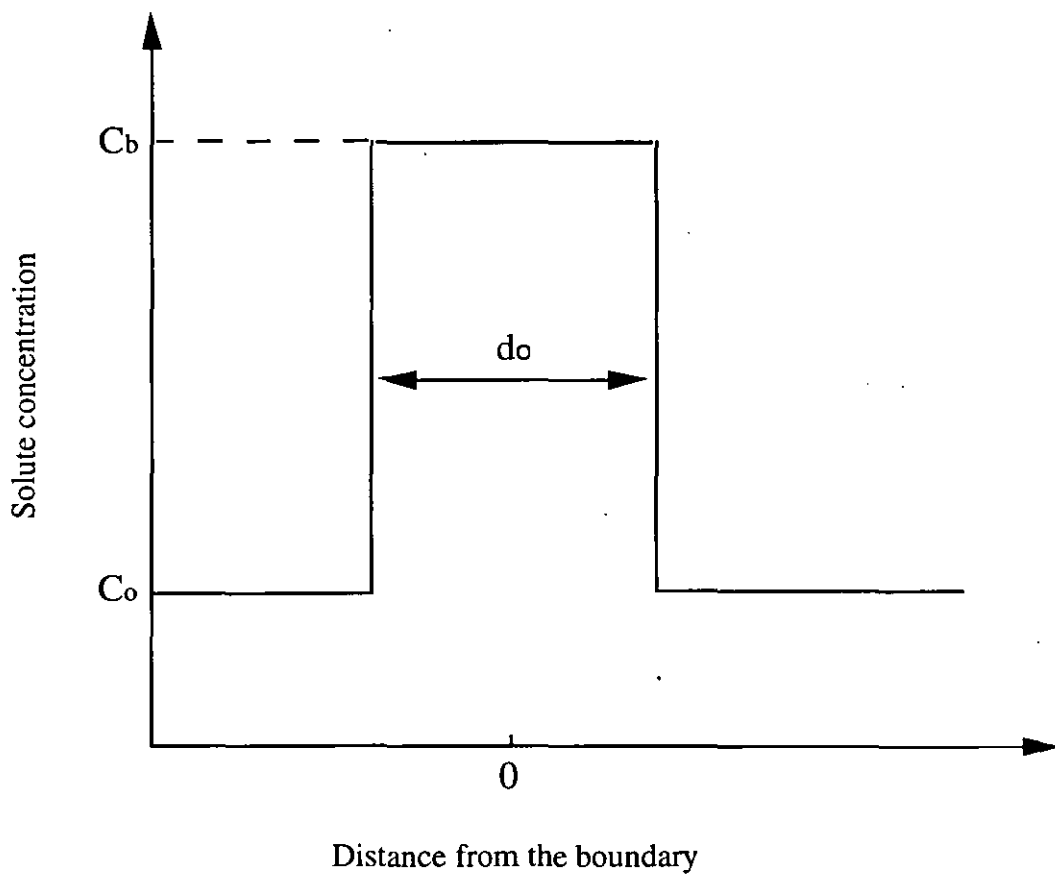


Fig. 8.26. The assumed solute distribution around the grain boundary (C_b is the solute concentration in the segregated layer; C_o is the solute concentration in the adjacent matrix; d_o is the width of the segregated layer).

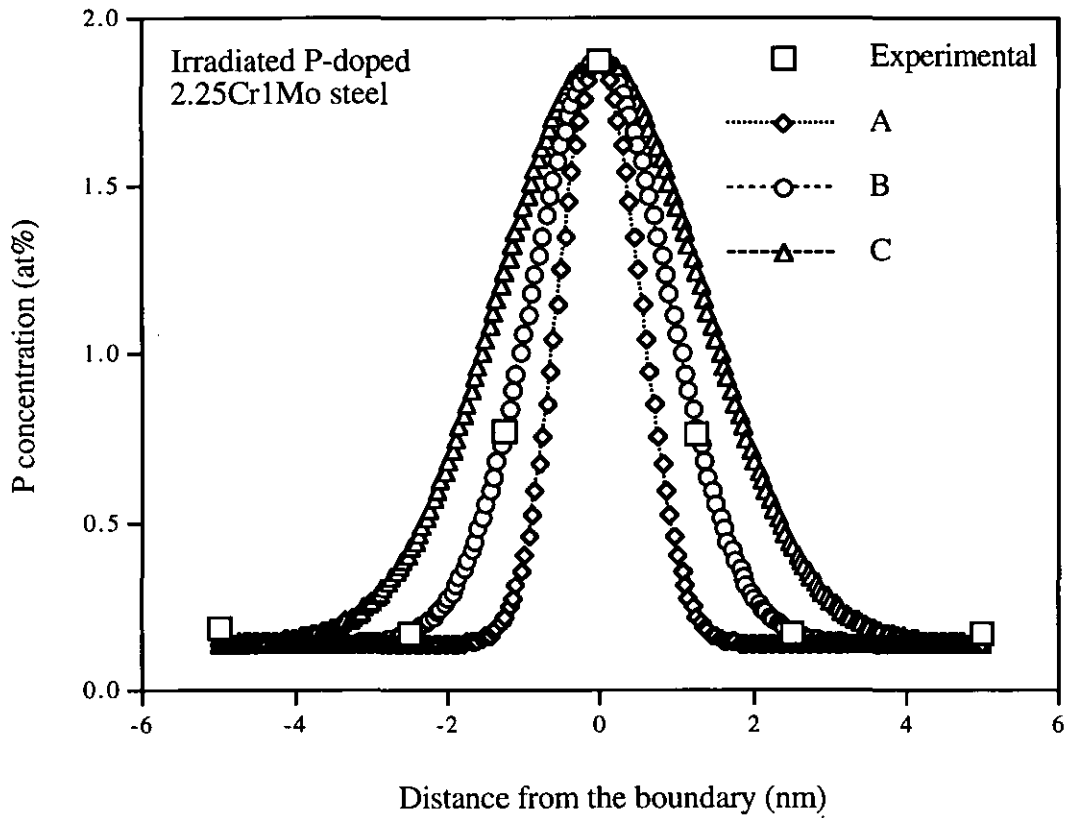


Fig. 8.27. Analytically derived concentration profiles of phosphorus for different boundary concentrations (C_b) and probe sizes (ϕ_{80}) at a segregated layer thickness of 1 nm for the irradiated P-doped 2.25Cr1Mo steel (A: $C_b = 2.4$ at% and $\phi_{80} = 1.5$ nm; B: $C_b = 4.0$ at% and $\phi_{80} = 3$ nm; C: $C_b = 5.8$ at% and $\phi_{80} = 4.6$ nm).

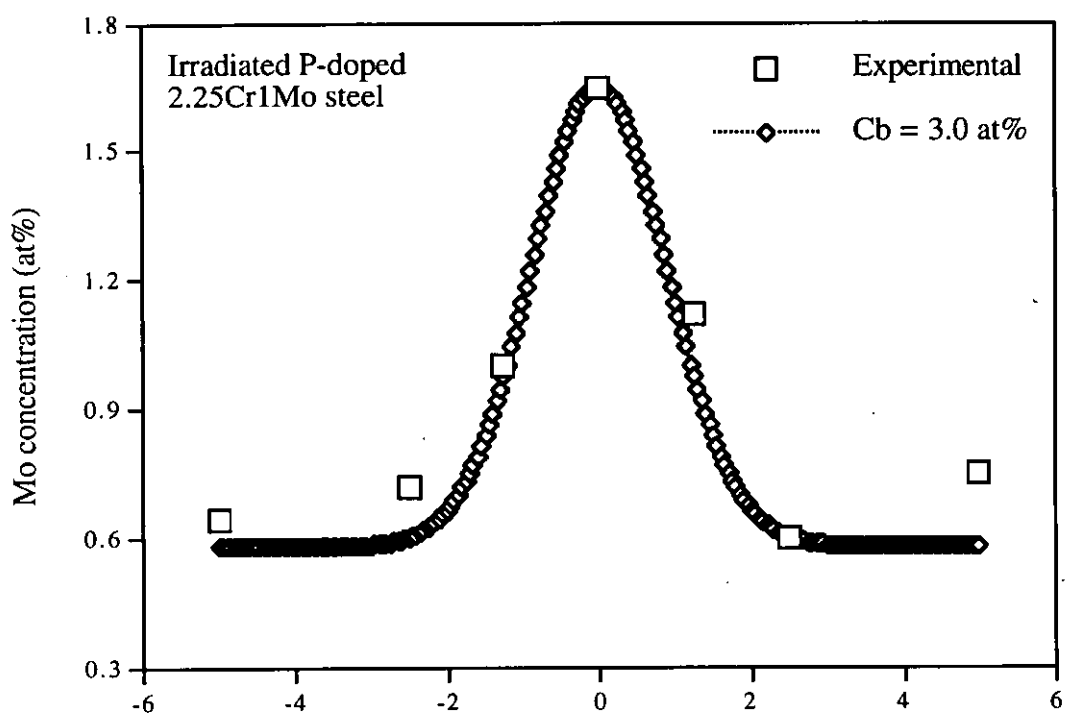


Fig. 8.28. Analytically derived concentration profile of molybdenum which fits best with the experimental result for the effective probe size of 3 nm at a segregated layer thickness of 1 nm for the irradiated P-doped 2.25Cr1Mo steel.

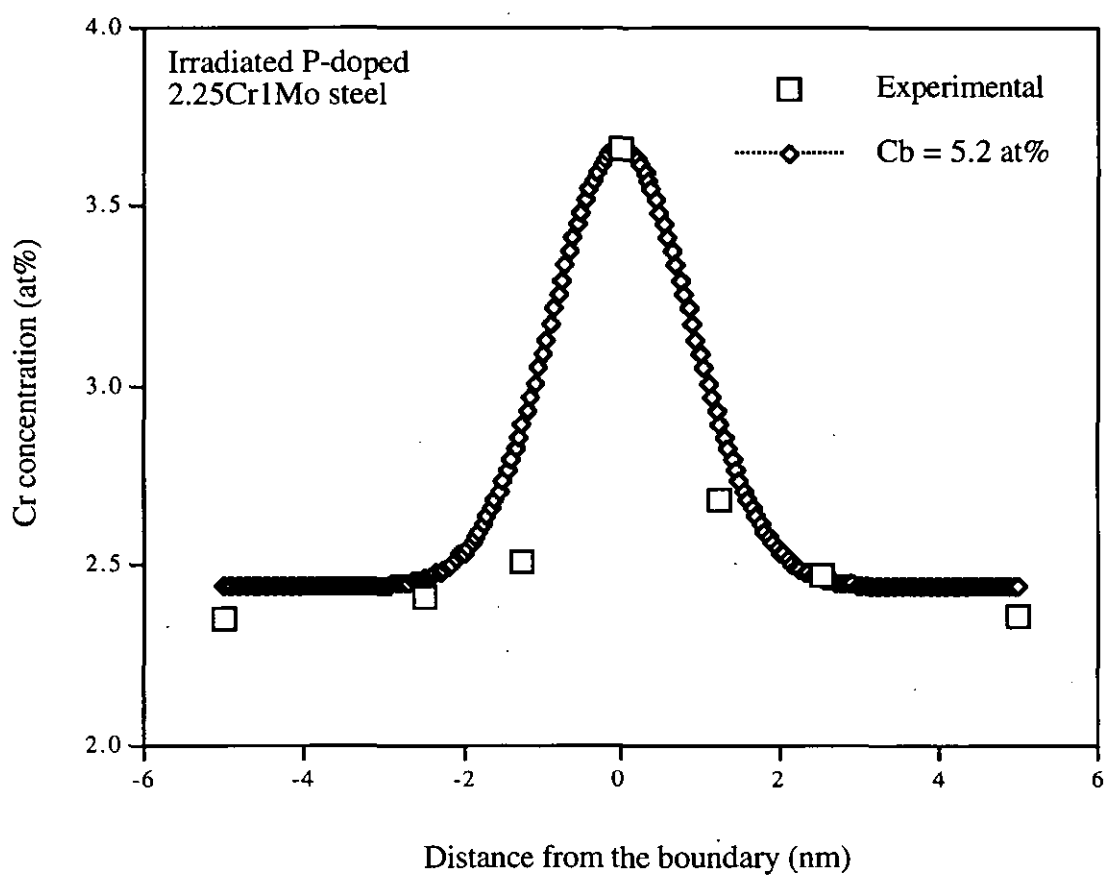


Fig. 8.29. Analytically derived concentration profile of chromium which fits best with the experimental result for the effective probe size of 3 nm at a segregated layer thickness of 1 nm for the irradiated P-doped 2.25Cr1Mo steel.

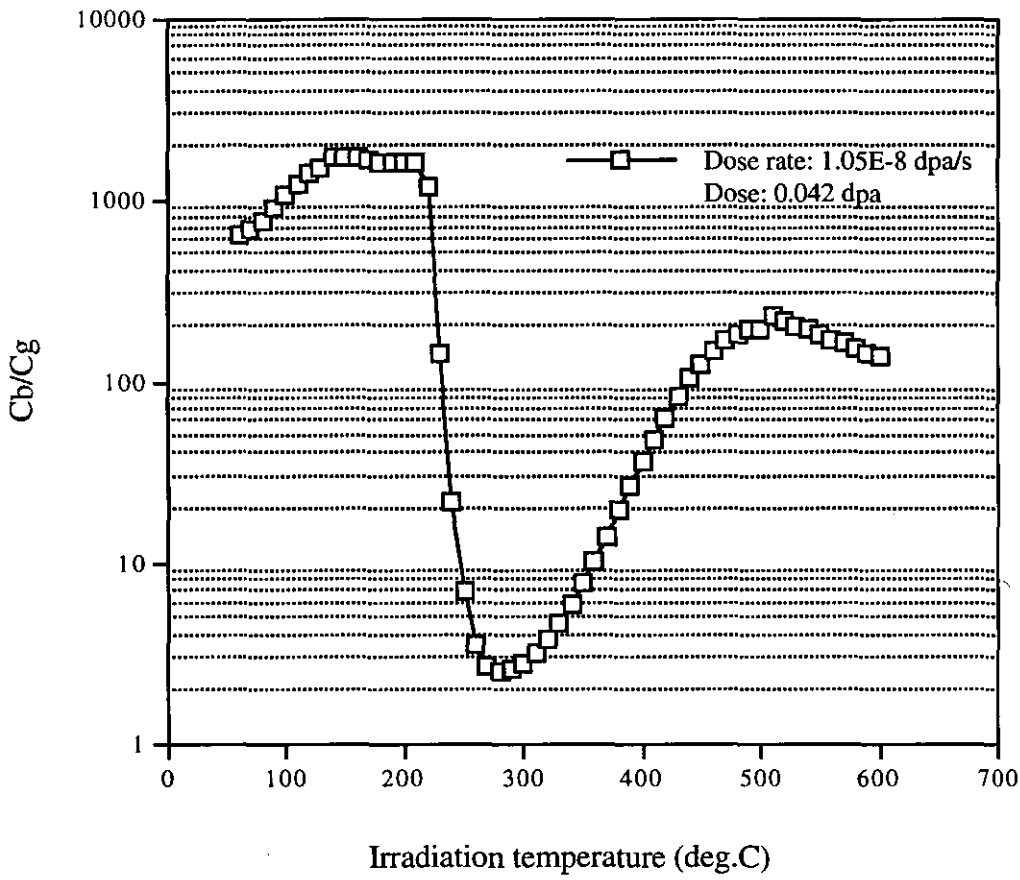


Fig. 8.30. The predicted temperature dependence of phosphorus segregation in the irradiated a-Fe for neutron dose rate = 1.05×10^{-8} dpa/s and neutron dose = 0.042 dpa ($B = 0.01$, $\epsilon = 0.1$, $R = 1 \mu\text{m}$, $\rho_o = 5 \times 10^{18} \text{ m}^{-2}$)

Appendix 8.3

Description of the Reactor SAPHIR

SAPHIR is a light water moderated open pool reactor which operates at a thermal power of 10 MW. The thermal neutron flux is $8 \times 10^{13} \text{ n} \cdot \text{cm}^{-2} \text{s}^{-1}$ at the core surface, up to $1.2 \times 10^{14} \text{ n} \cdot \text{cm}^{-2} \text{s}^{-1}$ in the central irradiation positions and $1 \times 10^{14} \text{ n} \cdot \text{cm}^{-2} \text{s}^{-1}$ at the beam hole nose behind a beryllium reflector.

The reactor building contains the reactor and experimental halls, control room and all rooms for the necessary auxiliary equipment such as work shops, water purification, electricity distribution and offices. A cross section view of the reactor building is given in Fig. A8.3.1.

The core is assembled by standard 23 plate MTR (materials testing reactor) fuel elements. At present, there are two types of element in use: a high enriched (93%) with 280g U-235 and a medium enriched (45%) with 320g U-235 for the standard element.

A standard core configuration consists of 30-32 elements and 15 beryllium reflector elements. The mean burn-up of such a reactor is about 30% (maximum burn-up, 65%) at the beginning of cycle. Two incore irradiation positions serve for isotope production and other high flux irradiations.

Four fork type control rods (Ag-In-Cd) serve as shim and safety rods and a stainless steel rod as the regulating rod.

The pool $9\text{m} \times 2.9\text{m} \times 8.4\text{m}$ in size (see Fig. A8.3.2) comprises about 210 m^3 demineralised water. The reactor bridge is movable along the pool. The reactor can operate at any position up to 100 kW but only in the zero-position at full power. This feature has mainly been employed in the past for shielding experiments and maintenance in the beam hole.

Five radial and two tangential beam holes, all equipped with specially developed shutter-plugs serve mainly for neutron scattering experiments. The arrangement of the beam ports is illustrated in Fig. A8.3.3.

The reactor is operated in three shifts at a four-week cycle, three weeks continuously at full power followed by one week for maintenance and low power operation. Therefore a total of about 270 days of full power operation and 60 days of low power operation could be achieved per year.

Figures for Appendix 8.3

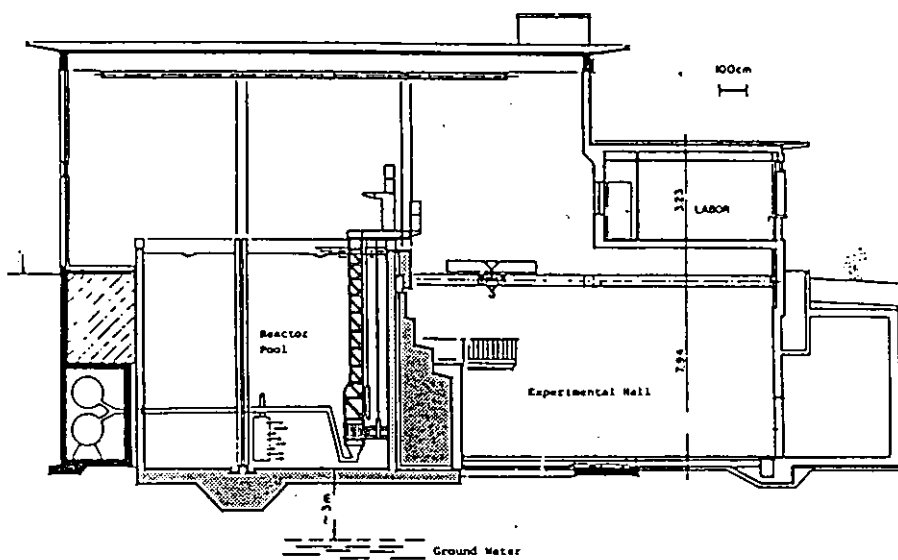


Fig. A8.3.1. A cross section view of the reactor building.

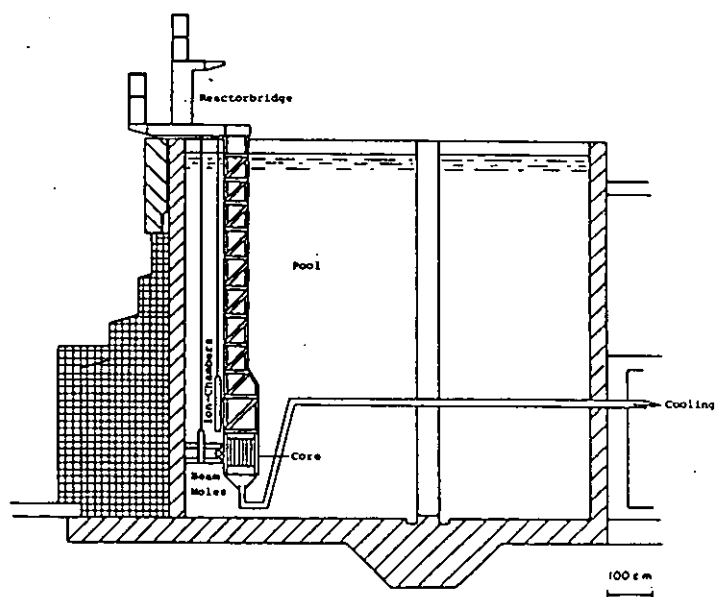


Fig. A8.3.2. Diagram showing the reactor pool.

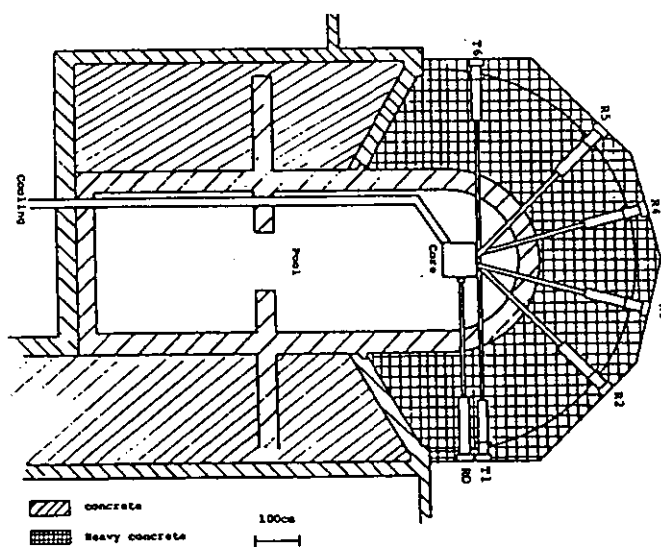


Fig. A8.3.3. Diagram showing the arrangement of the beam holes (there are five radial beam tubes and two tangential beam tubes).

Chapter Nine

Conclusions

9.1. Impurity-point defect binding energies

Modelling of irradiation-induced segregation or thermal non-equilibrium segregation needs data on the impurity-point defect binding energy. These values are generally unavailable. Faulkner and Chapman [52,53] have reasonably predicted impurity-vacancy binding energies, but their model requires to be slightly modified for more accurate calculations of oversized impurity-vacancy binding energies. In this work, an initial approach to determining impurity-interstitial binding energies in metals was established with some success on the basis of strain field arguments and the earlier work of Faulkner and Chapman was slightly modified for the evaluation of oversized impurity-vacancy binding energies. The method was applied to predictions of various impurity-point defect binding energies in several transition metal matrices.

Predicted results of binding energies for ferritic steel, austenitic stainless steel and nickel alloy matrices demonstrate that (i) the binding energies of the undersized impurity-interstitial complex, the undersized and oversized impurity-vacancy complexes increase with increasing difference between the impurity and matrix atom sizes; (ii) the binding energies of the oversized impurity-interstitial complexes decrease with increasing the difference between the impurity and matrix atom sizes and excepting nickel in α -Fe and chromium in nickel, which are marginally oversized impurities, oversized impurity elements have negative binding energies with the interstitial; (iii) the binding energy of the oversized impurity-vacancy complex is greater than that of the undersized impurity-vacancy complex as the size difference between the oversized impurity and matrix atoms is the same as that between the undersized impurity and matrix atoms; and (iv) the interaction of the undersized impurity and the interstitial is stronger than that of it and the vacancy.

With the aid of these predictions, some experimental results on radiation-induced segregation were reasonably satisfactorily interpreted.

9.2. Modelling of radiation-induced grain boundary segregation

A combined equilibrium and radiation-induced non-equilibrium grain boundary segregation model was established for dilute alloys on the basis of the complex mechanism. In the treatment of equilibrium segregation, radiation-enhanced solute diffusion was taken into account. The analysis was applied to predictions of

phosphorus grain boundary segregation in the α -Fe matrix under neutron irradiation. The predicted results are summarised as follows.

There exists a segregation transition temperature below which combined irradiation-induced non-equilibrium and irradiation-enhanced equilibrium segregation is dominant, and above which thermal equilibrium segregation is dominant; peaks in the temperature dependence of segregation shift to lower temperatures with decreasing neutron dose rate and/or increasing neutron dose; the combined radiation-induced non-equilibrium and radiation-enhanced equilibrium peak segregation temperature and thermal equilibrium peak segregation temperature are about 150 and 550 °C, respectively, for phosphorus grain boundary segregation in the α -Fe matrix at neutron dose rate = 10^{-6} dpa/s and neutron dose = 1 dpa.

The dislocation density has an effect on both radiation-induced segregation and equilibrium segregation. The grain size strongly influences radiation-induced segregation.

9.3. Experimental studies

Grain boundary segregation of solutes in the neutron-irradiated and unirradiated (thermally aged) 2.25Cr1Mo steels doped with P and Sn was examined by means of field emission gun scanning transmission electron microscopy (FEGSTEM). Under irradiation conditions employed in the present work, radiation effects were not clearly observed for P, Sn, Cr, Si and Ni. The boundary concentrations for these elements did not clearly vary after irradiation. There appears a certain radiation effect for Mo. The boundary concentration of Mo, to some extent, reduced after irradiation.

In recognition of insufficiently high resolution of the technique for grain boundary composition analysis, the measured result was corrected by means of an analytical convolution method developed by Faulkner et al. [177]. The corrected phosphorus segregation level may be up to ~4.0 at% for the irradiated P-doped 2.25Cr1Mo steel. This value is nearly the same as that (~3.6 at%) predicted by the model developed by Xu and Song [69] for quenching-induced phosphorus segregation to grain boundaries.

Comparison of the experimental and predicted results was performed. A good fit was obtained between them. The predictions for phosphorus segregation during neutron irradiation indicate that there is indeed no apparent radiation effect in the

range of 250-300 °C. Some experimental results from the Berkeley Technology Centre of the Nuclear Electric were also compared with the predictions. A good agreement was also acquired between them.

Chapter Ten

Future Work

There is great interest in ferritic steels for nuclear reactor applications in plant components such as pressure vessels, fuel canning and wrappers. Although there are several advantages to the steels in that they possess low void swelling and good thermal fatigue resistance, there is a limitation in that they suffer from considerable shifts in ductile-brittle transition temperature (DBTT) after neutron irradiation.

The future work is recommended to seek to identify, through a detailed mechanical testing programme, the key mechanisms of radiation-induced intergranular (IG) failure in common ferritic steels employed in the power industry such as 2.25Cr-1Mo steel and Fe-12Cr steel. It is anticipated that microstructural and microcompositional changes will be at the heart of the mechanisms mentioned. Hence a lot of work is recommended to be done by using the latest high resolution electron microscopy techniques.

10.1. Irradiation and testing

Mini-Charpy specimens and 2 mm diameter TEM discs are recommended to be prepared and to be neutron-irradiated at several different temperatures up to at least 0.1 dpa neutron dose. The small diameter for TEM discs is to minimise the gamma emission accompanying the Mn K_{α} X-rays, caused by the specimen-induced radioactivity.

The irradiated mini-Charpy specimens are to be tested in mini-Charpy testing facilities in the hot cells at temperatures over the range where the DBTT is expected. Meanwhile, the thermal-control specimens are to be tested so as to be compared with the irradiated specimens.

10.2. Electron microscopy

The irradiated TEM samples are to be examined for microstructural damage effects and for grain boundary and lath boundary segregation effects in conventional and FEGSTEM machines. Simultaneously, the thermal-control TEM samples are to be examined so as to be compared to the irradiated samples.

SEM studies of the fracture surfaces on selected samples are to be carried out in the hot cells.

10.3. Grain and lath boundary segregation modelling during neutron irradiation

Considerable expertise in radiation-induced segregation (RIS) has been developed during projects between Loughborough University and Nuclear Electric Berkeley Technology Centre over the last few years. The further work is recommended to take account of the following effects.

- 1) Pre-irradiation effects.
- 2) Effects of neutron energy spectrum.
- 3) Dose rate dependence of RIS.
- 4) Associated depletion effects of major alloying elements around grain and lath boundaries as a consequence of RIS. This is of particular relevance to Cr behaviour around boundaries and resulting IG corrosion effects which are prevalent in high-alloy steels.

10.4. Relation of IG fracture processes in ferritic steels to segregation

Many pointers exist in the literature on how to relate intergranular fracture to grain boundary structure and composition. Lim and Watanabe [193] have shown that the detailed grain boundary structure affects crack propagation paths. McMahon and Vitek [194] have given an elegant analysis on how to relate small changes in grain boundary energy brought about by impurity segregation to fracture toughness. A unified theory of grain boundary fracture strength has been developed by Shvindlerman and Faulkner [195]. This theory is associated with impurity segregation to grain boundaries.

The information generated in the experimental work mentioned above may be utilised to support and probably modify the unified model for intergranular fracture strength as applied to ferritic steels. It is anticipated that it is possible to show the reasons for the DBTT shifts in these steels as a function of neutron irradiation parameters.

10.5. Summary

The future work has been recommended aimed at understanding the mechanisms underlying irradiation-induced DBTT shifts in ferritic steels. The unique features of the work are as follows.

- 1) The creation of new information about microcompositional and microstructural changes occurring at grain boundaries during neutron irradiation.
- 2) The production of irradiation-induced DBTT shift experimental data from an original and specifically dedicated testing programme .
- 3) New modelling approaches to enabling more accurate forecasting of RIS and IG fracture behaviour in ferritic steels.

References

1. P.R. Okamoto and H. Wiedersich, *J. Nucl. Mater.* **53** (1974) 336.
2. P.R. Okamoto, A.T. Santhanam, H. Wiedersich and A. Taylor, *Nucl. Technol.* **22** (1974) 45.
3. A. Barbu and A.J. Ardell, *Scripta Metall.* **9** (1975) 1233.
4. A. Barbu and G. Martin, *Scripta Metall.* **11** (1977) 771.
5. G. Silvestre, A. Silvent, C. Regnard and G. Sainfort, *J. Nucl. Mater.* **57** (1975) 125.
6. L.E. Rehn, P.R. Okamoto, D.I. Potter and H. Wiedersich, *J. Nucl. Mater.* **74** (1978) 242.
7. L.E. Rehn, P.R. Okamoto and H. Wiedersich, *J. Nucl. Mater.* **80** (1979) 172.
8. D.I. Potter, L.E. Rehn, P.R. Okamoto and H. Wiedersich, *Scripta Metall.* **11** (1977) 1095.
9. D.I. Potter and D.G. Ryding, *J. Nucl. Mater.* **71** (1977) 14.
10. D.I. Potter and H. Wiedersich, *J. Nucl. Mater.* **83** (1979) 208.
11. A.D. Marwick and R.C. Piller, *Radiation Effects* **33** (1977) 245.
12. R.C. Piller and A.D. Marwick, *J. Nucl. Mater.* **71** (1978) 309.
13. A.D. Marwick, R.C. Piller and P.M. Siveil, *J. Nucl. Mater.* **83** (1979) 35.
14. A. Kenik, *Scripta Metall.* **10** (1976) 733.
15. K. Farrell, J. Bently and N.D. Braski, *Scripta Metall.* **11** (1977) 243.
16. R.A. Erck, D.I. Potter and H. Wiedersich, *J. Nucl. Mater.* **80** (1979) 120.

17. J. Kameda and A.J. Bevolo, *Acta Metall.* **37** (1989) 3283.
18. C.M. Shepherd and T.M. Williams, *J. Nucl. Mater.* **168** (1989) 337.
19. F.A. Garner, H.R. Brager and J.M. McCarthy, in *Radiation-induced changes in microstructure: 13th Int. Symp.*, ASTM STP 955, eds. F.A. Garner, N.H. Packan and A.S. Kumar (ASTM, Philadelphia, 1987) p. 775.
20. P. Jung and H. Klein, *J. Nucl. Mater.* **182** (1991) 1.
21. E.A. Kenik, T. Inazumi and G.E.C. Bell, *J. Nucl. Mater.* **183** (1991) 145.
22. T.S. Morgan, E.A. Little, R.G. Faulkner and T.M. Titchmarsh, in *Effects of Radiation on Materials: 15th Int. Symp.* ASTM STP 1125, eds. R.E. Stoller, A.S. Kumar and D.S. Gelles (ASTM, Philadelphia, 1992) p. 633.
23. R.E. Clausing, L. Heatherly, R.G. Faulkner, A.F. Rowcliffe and K. Farrell, *J. Nucl. Mater.* **141-143** (1986) 978.
24. E.A. Little, T.S. Morgan and R.G. Faulkner, *Mater. Sci. Forum* **97-99** (1992) 323.
25. M.K. Miller and M.G. Burke, *J. Nucl. Mater.* **195** (1992) 68.
26. J.M. Cookson, R.D. Carter, D.L. Damcott, M. Atzmon and G.S. Was, *J. Nucl. Mater.* **202** (1993) 104.
27. R.D. Carter, D.L. Damcott, M. Atzmon, G.S. Was and E.A. Kenik, *J. Nucl. Mater.* **205** (1993) 361.
28. R.A. Johnson and N.Q. Lam, *Phys. Rev.* **B13** (1976) 4364.
29. R.A. Johnson and N.Q. Lam, *Phys. Rev.* **B15** (1977) 1794.
30. R.A. Johnson and N.Q. Lam, *J. Nucl. Mater.* **69-70** (1978) 424.
31. N.Q. Lam, P.R. Okamoto, H. Wiedersich and A. Taylor, *Metall. Trans.*

9A (1978) 1707.

32. H. Wiedersich, P.R. Okamoto and N.Q. Lam, *J. Nucl. Mater.* **83** (1979) 98.
33. J.R. Manning, *Phys. Rev.* **B4** (1971) 1111.
34. A.D. Marwick, *J. Phys. F: Metal Phys.* **8** (1978) 1849.
35. J.M. Perks and S.M. Murphy, in *Materials for Nuclear Reactor Core Applications* (British Nuclear energy Society, London, 1987) Vol. 1, p.165.
36. S.M. Murphy, *Phil. Mag.* **A59** (1989) 953.
37. S.M. Murphy and J.M. Perks, *J. Nucl. Mater.* **171** (1990) 360.
38. R.G. Faulkner, N.C. Waite, E.A. Little and T.S. Morgan, *Mater. Sci. Eng.* **A171** (1993) 241.
39. R.G. Faulkner, S. Song and P.E.J. Flewitt, *J. Nucl. Mater.* **212-215** (1994) 608.
40. P.R. Okamoto and L.E. Rehn, *J. Nucl. Mater.* **83** (1979) 2.
41. R.G. Faulkner, S. Song and P.E.J. Flewitt, *Phil. Mag. A*, To be published.
42. N.Q. Lam and G.K. Leaf, *J. Mater. Res.* **1**(2) (1986) 251.
43. L.E. Rehn and P.R. Okamoto, in *Phase Transformations during Irradiation*, ed. F.V. Nolfi (Applied Science Publishers, London, 1983), Chap. 1, pp. 274-290.
44. A.R. Allnatt, A. Barbu, A.D. Franklin and A.B. Lidiard, *Acta Metall.* **31** (1983) 1307.
45. A.R. Allnatt and A.B. Lidiard, *Rep. Prog. Phys.* **50** (1987) 373.
46. S.G. Druce, C.A. English, A.J.E. Foreman, R.J. McElroy, I.A. Vatter,

- C.J. Bolton, J.T. Buswell and R.B. Jones, "The Modelling of Irradiation-Enhanced Phosphorus Segregation in Neutron Irradiated RPV Submerged-Arc Welds", in *Effects of Radiation on Materials: 17th Int. Symp.*, ASTM STP 12xx, eds. D.Gelles, R.K. Nanstead, A.S. Kumar and E.A. Little (American Society of Testing and Materials, Philadelphia, 1995), in press.
47. J.R. Hawthorne, J.J. Koziol and R.C. Groescher, in *Properties of Reactor Structural Alloys after Neutron or Particle Irradiation*, ASTM STP 570, eds. C.J. Baroch and F.R. Shober (ASTM, Philadelphia, 1975) p. 83.
 48. C. Guionnet, B. Houssin, D. Brasseur, A. Lefort, D. Gros and R. Perdreau, in *Proceedings of the Symposium on the Effects of Radiation on Materials*, ASTM STP 782, eds. H.R. Brager and J.S. Perrin (ASTM, Philadelphia, 1982) p. 392.
 49. W. J. Phythian and C.A. English, *J. Nucl. Mater.* **205** (1993) 162.
 50. E.A. Little and G Gage, *Nucl. Energy* **33** (1994) 163.
 51. D. McLean, "*Grain Boundaries in Metals*" (Oxford University Press, London, 1957).
 52. M.A.V. Chapman and R.G. Faulkner, *Acta Metall.* **31** (1983) 677.
 53. R.G. Faulkner, *Mater. Sci. Technol.* **1** (1985) 442.
 54. D. McLean and L. Northcott, *J. Iron Steel Inst.* **158** (1948) 169.
 55. J.M. Gibbs, "*The Collected works of J. Willard Gibbs*", Vol. 1, p. 230.
 56. M. Guttman, *Surf. Sci.* **53** (1975) 213.
 57. M.P. Seah, *Acta Metall.* **25** (1977) 345.
 58. J.W. Cahn and J.E. Hilliard, *Acta Metall.* **7** (1959) 219.
 59. E.D. Hondros, "*Interfaces*", ed. R.C. Gifkins (Butterworths, London 1969) p. 77.

60. E.D. Hondros and D. McLean, "*Surface Phenomena of Metals*" (Society of Chemical Industry, London, 1968) p. 39.
61. J.R. Low, *Trans. AIME*, **245** (1969) 2481.
62. K.T. Aust, S.J. Armijo, E.F. Koch and J.A. Westbrook, *Trans. Amer. Soc. Met.* **60** (1967) 360.
63. T.R. Anthony, *Acta Metall.* **17** (1969) 603.
64. Xu Tingdong, *J. Mater. Sci. Lett.* **7** (1988) 241.
65. Song Shenhua, Xu Tingdong and Yuan Zhexi, *Acta Metall.* **37**(1989)319.
66. Xu Tingdong, Song Shenhua, Shi Huazhong, W. Gust and Yuan Zhexi, *Acta Metall. Mater.* **39** (1991) 3119.
67. R.G. Faulkner, *J. Mater. Sci.* **16** (1981) 373.
68. P. Doig and P.E.J. Flewitt, *Acta Metall.* **29** (1981) 1831.
69. Xu Tingdong and Song Shenhua, *Acta Metall.* **37** (1989) 2499.
70. M.L. Swanson and L.M. Howe, *J. Nucl. Mater.* **69-70** (1978) 372.
71. L.E. Rehn, K-H. Robrok and H. Jacques, *J. Phys. F: Metal Phys.* **8** (1978) 1835.
72. P.H. Dederichs, C. Lehman, H.R. Schober, A. Scholz and R. Zeller, *J. Nucl. Mater.* **69-70** (1978) 176.
73. H. Wiedersich, P.R. Okamoto and N.Q. Lam, in *Radiation Effects in Breeder Reactor structural Materials*, eds. M.L. Bleiberg and J.W. Bennett (AIME, New York, 1977) p.801.
74. R.G. Faulkner, E.A. Little and T.S. Morgan, *J. Nucl. Mater.* **191-194** (1992) 858.

75. D.I.R. Norris, C. Baker and J.M. Titchmarsh, in *Radiation-induced Sensitisation of Stainless Steels*, ed. D.I.R. Norris (CEGB, 1986) p. 86.
76. J.M. Titchmarsh and I.A. Vatter, in *Radiation-induced Sensitisation of Stainless Steels*, ed. D.I.R. Norris (CEGB, 1986) p. 74.
77. M. Ashworth, I.P. Jones and D.I.R. Norris, in *Materials for Nuclear Reactor Core Applications* (British Nuclear Energy Society, London, 1987), Vol. 2 p. 9.
78. Y.G. Zhang and I.P. Jones, *Mater. Sci. Forum*, **15-18** (1987) 499.
79. G.J. Mahon, A.W. Nicholls, I.P. Jones, C.A. English and T.M. Williams, in *Radiation-Induced Sensitisation of Stainless Steels*, ed. D.I.R. Norris (CEGB, London, 1987) p. 99.
80. H. Wiedersich and N.Q. Lam, in *Phase Transformations during Irradiation*, ed. F.V. Nolfi (Applied Science Publishers, London, 1983), Chap. 1, pp. 1-46.
81. H.M. Chung, W.E. Ruther, J.E. Sanecki and T.F. Kassner, in *Proc. Fifth Int. Symp. Environmental Degradation of Materials in Nuclear Power Systems - Water Reactors*, eds. D. Cubicciotti, E.P. Simonen and R. Gold (American Nuclear Society, La Grange, IL, 1992) p.795.
82. A.J. Jacobs, R.E. Clausen, M.K. Miller and C.M. Shepherd, in *Proc. 4th Int. Symp. Environmental Degradation of Materials in Nuclear Power Systems - Water Reactors*, ed. D. Cubicciotti (National Association of Corrosion Engineers, 1990) p. 14.
83. S.B. Fisher, C. Baker, R. Scowen, B. Lee, J. Walmsley and S. Mowles, IASCC Grain Boundary Analysis, ABB Atom AB Reference L841 11865, Nuclear Electric Berkeley Technology Centre, 1994.
84. S.M. Bruemmer and E.P. Simonen, *Corrosion '93, Paper no. 616* (National Association of Corrosion Engineers, Houston, TX 1993).
85. E.A. Kenik, *J. Nucl. Mater.* **205** (1993) 317.

86. E.A. Kenik, *Metall. Trans.* **22A** (1991) 253.
87. H. Takahashi, S. Ohnuki and T. Takeyama, *J. Nucl. Mater.* **103-104** (1981) 1415.
88. J.L. Brimhall, D.R. Baer and R.H. Jones, *J. Nucl. Mater.* **117** (1983) 218.
89. J.L. Brimhall, D.R. Baer and R.H. Jones, *J. Nucl. Mater.* **122-123** (1984) 196.
90. H. Takahashi, *J. Nucl. Mater.* **155-157** (1988) 908.
91. R.E. Clausen, L. Heatherly, R.G. Faulkner, A.F. Rowcliffe and K. Farrell, *J. Nucl. Mater.* **141-143** (1988) 978.
92. T.S. Morgan, *PhD thesis*, Loughborough University of Technology, 1992.
93. E.A. Little and D.A. Stow, *Metal Sci.* **14** (1980) 89.
94. D.S. Gelles, *J. Nucl. Mater.* **103-104** (1981) 975.
95. P.J. Maziasz, R.L. Klueh and J.M. Vitek, *J. Nucl. Mater.* **141-143** (1986) 929.
96. P.J. Maziasz, *J. Nucl. Mater.* **169** (1989) 95.
97. N.Q. Lam, P.R. Okamoto and H. Wiedersich, *J. Nucl. Mater.* **74** (1978) 101.
98. W.G. Johnson, T. Lauritzen, J.H. Rosolowski and A.M. Turkalo, in *Radiation Damage in Metals*, American Society of Metals, Metals Park, OH, 1976, p. 227.
99. J.F. Bates and W.G. Johnston, in *Proceedings of the International Conference on Radiation Effects in Breeder Reactor Structural Materials*, Scottsdale, AZ, June 19-23, 1977, Metallurgical Society of American Institute of Mining, Metallurgical and Petroleum Engineers, New York, 1977, p. 625.

100. P.J. Maziasz, *J. Nucl. Mater.* **133-134** (1985) 134.
101. E.H. Lee, N.H. Packan and L.K. Mansur, *J. Nucl. Mater.* **117** (1983) 123.
102. J.R. Hawthorne and F.A. Smidt, Jr., *J. Nucl. Mater.* **103-104** (1981) 883.
103. C. Wassilev and K. Ehrlich, *J. Nucl. Mater.* **191-194** (1992) 850.
104. R.L. Klueh and D.J. Alexander, *J. Nucl. Mater.* **191-194** (1992) 896.
105. P.L. Andresen, F.P. Ford, S.M. Murphy and J.M. Perks, in *Proc. 4th Int. Symp. on Environmental Degradation of Materials in Nuclear Power Systems - Water Reactors*, ed. D. Cubicciotti (National Association of Corrosion Engineers, 1990) p. 83.
106. G.S. Was and P.L. Andresen, *J. Metals* **44** (1992) 8.
107. P.L. Andresen, in *Proc. 5th Int. Symp. on Environmental Degradation of Materials in Nuclear power Systems - Water Reactors*, Monterey, CA, eds. D. Cubicciotti, E.P. Simonen and R.E. Gold (American Nuclear Society, 1992) p. 209.
108. P.L. Andresen and C.L. Briant, *Corrosion* **45** (1989) 448.
109. C.L. Briant and P.L. Andresen, *Metall. Trans.* **19A** (1988) 495.
110. J.M. Cookson, R.D. Carter, D.L. Damcott, M. Atzmon, G.S. Was and P.L. Andresen, in *Proc. 5th Int. Symp. On Environmental Degradation of Materials in Nuclear Power Systems - Water Reactors*, Monterey, CA, eds. D. Cubicciotti, E.P. Simonen and R.E. Gold (American Nuclear Society, 1992) p. 806.
111. J.M. Cookson, R.D. Carter, D.L. Damcott, M. Atzmon and G.S. Was, *J. Nucl. Mater.* **202** (1993) 104.
112. J.M. Cookson, D.L. Damcott, G.S. Was and P.L. Andresen, "The Role of Microchemical and Microstructural Effects in The IASCC of High Purity Austenitic Stainless Steels" in *Proc. 6th Int. Symp. On Environmental*

Degradation of Materials in Nuclear Power Systems - Water Reactors,
eds. R.E. Gold and E.P. Simonen (American Nuclear Society, 1993) p.573.

113. S.M. Bruemmer and G.S. Was, *J. Nucl. Mater.* **216** (1994) 348.
114. G.P. Airey, *Metallography* **13** (1980) 21.
115. Xu Tingdong, Song Shenhua, Yuan Zhexi and Yu Zongsen, *J. Mater. Sci.* **25** (1990) 1739.
116. Song Shenhua, Xu Tingdong, Yuan Zhexi and Yu Zongsen, *Acta Metall. Mater.* **39** (1991) 909.
117. T.M. Williams, A.M. Stoneham and D.R. Harries, *Metal Sci.* **10** (1976) 14.
118. R.H. Jones and S.M. Bruemmer, in *Proc. Environment-Induced Cracking of Metals*, eds. R. Gangloff and M.B. Ives (National Association of Corrosion Engineers, 1989) p. 287.
119. M.T. Robinson, in *Radiation Damage in Metals*, eds. S.D. Harkness and N.L. Peterson (American Society of Metals, Metals Park, OH, 1976) p. 1.
120. J. Lindhard, M. Scharff and H.E. Schiott, *Mat. Fys. Medd. Dan. Vid. Selsk.* **33** (1963) 14.
121. G.H. Kinchin and R.S. Pease, *Rep. Prog. Phys.* **18** (1955) 1.
122. P. Sigmund, *Appl. Phys. Lett.* **14** (1969) 114.
123. L.K. Mansur, "Mechanisms and Kinetics of Radiation Effects in Metals and Alloys", in *Kinetics of Nonhomogeneous Processes*, ed. G.R. Freeman (John Wiley and Sons, New York, 1987) pp. 377-463.
124. M.J. Norgett, M.T. Robinson and I.M. Torrens, *Nucl. Eng. Des.* **33** (1974) 50.

125. J.F. Ziegler, J.P. Biersack and U. Littmark, "*Stopping and Range of Ions in Solids*", Vol. 1 (Pergamon, New York, 1985).
126. A.F. Calder and D.J. Bacon, *J. Nucl. Mater.* **207** (1993) 25.
127. K.L. Merkle, in *Radiation Damage in Metals*, eds. S.D. Harkness and N.L. Peterson (American Society of Metals, Metals Park, OH, 1976) p. 58.
128. B.L. Eyre, in *Fundamental Aspects of Radiation Damage In Metals*, eds. M.T. Robinson and F.W. Young (U.S. Energy Research and Development Admin., CONF-751006, Gatlinbury, TN, 1975) p. 729.
129. M. Kiritani, in *Proceedings of Yamada Conference V on Point Defects and Defect Interactions in Metals*, eds. J.-I. Takamura, M. Doyama and M. Kiritani (Tokyo University Press, Tokyo) 1982.
130. S. Ishino, K. Fukuya, T. Muroga, N. Sekimura and H. Kawanishi, *J. Nucl. Mater.* **122-123**(1984)597.
131. J.B. Mitchell, R.A. Konynenberg, M.W. Guinan and C.J. Echer, *Phil. Mag.* **31** (1975) 919.
132. M.L. Jenkins, K.H. Katerban and M. Wilkens, *Phil. Mag.* **34** (1976) 1155.
133. J. Narayan and S.M. Ohr, *J. Nucl. Mater.* **63** (1976) 454.
134. P. Moser, C. Corbel, P. Lucasson and P. Hautojarvi, *Mater. Sci. Forum* **15-18** (1987) 925.
135. M. Doyama, *J. Nucl. Mater.* **69-70** (1978) 350.
136. N.H. March, *J. Nucl. Mater.* **69-70** (1978) 490.
137. O. Takai, R. Yamamoto, M. Doyama and Y. Hisamatsu, *Phys. Rev.* **B10** (1974) 3113.
138. H. Wollenberger, *J. Nucl. mater.* **69-70** (1978) 362.

139. F.W. Young, *J. Nucl. Mater.* **69-70** (1978) 310.
140. W. Schilling, *J. Nucl. Mater.* **69-79** (1978) 465.
141. R.A. Johnson, *Phys. Rev.* **A134** (1964) 1329.
142. R.A. Johnson, *J. Phys. F: Metal Phys.* **3** (1973) 295.
143. K.H. Robrock, *Mater. Sci. Forum* **15-18** (1987) 537.
144. H. Jacques and K.H. Robrock, in *Proceedings of the Yamada conf. on point defects and defect interactions in metals*, eds. J. Takamura, M. Doyama and M. Kiritani (Tokyo University Press, 1982) p. 159.
145. R.A. Johnson, *J. Nucl Mater.* **135** (1985) 283.
146. J.H. Evans, *J Nucl Mater.* **119** (1983) 180.
147. P. Lucasson, F. Maury and A. Lucasson, *Rad. Eff. Lett.* **85** (1985) 219.
148. R.P. Gupta, *Phys. Rev.* **B22** (1980) 5900.
149. F. Dworschak, R. Lennartz and H Wollenberger, *J. Phys. F: Metal Phys.* **5** (1975) 400.
150. F. Dworschak, Th. Monsau and H Wollenberger, *J. Phys. F: Metal Phys.* **6** (1976) 1207.
151. M.L. Swanson and F. Manry, *Canad. J. Phys.* **53** (1975) 1117.
152. L.E. Murr, *"Interfacial Phenomena in Metals and Alloys"*, Addison-Welsley, London, 1975, p. 142.
153. J.D.H. Donnay and H. M. Ondik (eds.), *"Crystal Data - Determinative Tables"*, Third Edition, Volume II, Published jointly by the U.S. Department of Commerce, National Bureau of Standards, and the Joint Committee on Powder Diffraction Standards, USA, 1973, pp. C1-C374.

154. P. Marshall, "*Austenitic Stainless Steels - Microstructure and Mechanical Properties*", Elsevier Applied Science Publishers, London, 1984, p. 36.
155. M.C. Inman and H.R. Tipler, *Metall. Rev.* **8** (1963) 105.
156. E.A. Brandes and G.B. Brook (eds.), "*Smithells Metals Reference Book*", Seventh Edition, Butterworth-Heinemann, Oxford, 1992, p. 15-2.
157. M. Neklyudov and V. N. Voyevodin, *J. Nucl. Mater.* **212-215** (1994) 39.
158. E.D. Hondros and M.P. Seah, *Int. Metals Rev.* **22** (1977) 262.
159. C.A. English, S.M. Murphy and J.M. Perks, *J. Chem. Soc. Faraday Trans.* **86** (1990) 1263.
160. L.E. Rehn, *J. Nucl. Mater.* **174** (1990) 144.
161. V. Naundorf, M-P. Macht and H. Wollenberger, *J. Nucl. Mater.* **186** (1992) 227.
162. H. Trinkaus, V. Naundorf, B.N. Singh and C.H. Woo, *J. Nucl. Mater.* **210** (1994) 244.
163. C.H. Woo and B.N. Singh, *Phil. Mag.* **A65** (1992) 889.
164. A.V. Nikolaeva, Yu.A. Nikolaev and A.M. Kryukov, *J. Nucl. Mater.* **218** (1994) 85.
165. N. Q. Lam, A. Kumar and H. Wiedersich, in *Effects of Radiation on Materials: 11th Inter Cof.*, ASTM STP 782, H. R. Brager and J. S. Perrin, Eds., American Society of Testing and Materials, Philadelphia, 1982, p. 985.
166. S.M. Kim and W.J.L. Buyers, *J. Phys. J. Phys. F: Metal Phys.* **8** (1978) L103.
167. R.W. Cahn and P. Haasen (eds.), "*Physical Metallurgy*" Third Edition (North-Holland, Amsterdam, 1983) p. 1189.

168. M. Kiritani, H. Takata, K. Moriyama and F. Euchii Fujita, *Phil. Mag.* **A40** (1979) 779.
169. R. Bullough, M. R. Hayns and M. H. Wood, *J. Nucl. Mater.* **90** (1980) 44.
170. D. Hull and D J. Bacon, "*Introduction to Dislocations*", 3rd Edition (Pergamon, Oxford, 1984) p. 79.
171. T. Qgura, *Trans. Jan. Inst. Met.* **22(2)** (1981) 109.
172. E. A. Little and L. P. Stoter, in *Effects of Radiation on Materials: 11th Inter. Conf. ASTM STA 782*, H. R. Brader and J. S. Perrin, Eds., American Society of Testing and Materials, Philadelphia, 1982, p. 207.
173. D.I.R. Norris, C. Baker, C. Taylor and J.M. Titchmarsh, in *Effects of Radiation on Materials: 15th Inter. Symposium, ASTM STP 1125*, R. E. Stoller, A. S. Kumar and D. S. Gelles, Eds., American Society of Testing and Materials, Philadelphia, 1992, p. 603.
174. B. A. Loomis and D. L. Smith, in *Effects of Radiation on Materials: 15th Inter. Symposium, ASTM STP 1125*, R. E. Stoller, A. S. Kumar and D. S. Gelles, Eds., American Society of Testing and Materials, Philadelphia, 1992, p. 885.
175. T. Hashimoto and N. Shigenaka, *J. Nucl. Mater.* **189**(1992)161.
176. R. A. Mulford, C. J. McMahon Jr., D. P. Pope and H. C. Feng, *Metall. Trans.* **7A** (1976) 1183.
177. Yuan Zhexi, Song Shenhua, R.G. Faulkner and Xu Tingdong, *Acta Metall. Mater.* **42** (1994) 127.
178. J.M. Titchmarsh, C.M. Shepherd and I.A. Vatter, *Harwell Research Report*, AERE-R12317, 1987.
179. V.G. Microscopes: *The HB501 and V.G. Microscopes Product News*.

180. D.B. Williams, "*Practical Analytical Electron Microscopy in Materials Science*", Electron Optics Publishing Group, Florida, 1984, p. 7.
181. L. Reimer, "*Transmission electron microscopy: physics of image formation and microanalysis*", Springer-Verlag, 1989.
182. I.A. Vatter and J.M. Titchmarsh, *Ultramicroscopy* **28** (1989) 236.
183. K. Rektorys, "*Survey of Applicable Mathematics*", Iliffe Books Ltd, London, 1969, p. 1264.
184. Vorlicek and P.E.J. Flewitt, *Acta Metall. Mater.* **42** (1994) 3309.
185. M.S. Laws and P.J. Goodhew, *Acta Metall. Mater.* **39** (1991) 1525.
186. R.G. Faulkner, T.S. Morgan and E.A. Little, X-Ray Spectrometry, **23** (1994) 195.
187. D.B. Williams, "*Practical Analytical Electron Microscopy in Materials Science*", Electron Optics Pub. Co., Florida, 1984, p. 83.
188. J.I. Goldstein, J.L. Costley, G.W. Lorimer and S.J.B. Reed, In *SEM 1977*, ed. O. Johari, IITRI, Chicago, p. 315.
189. N.L. Peterson, *Int. Met. Rev.* **28** (1983) 65.
190. E.A. Brandes and G.B. Brook (eds.), "*Smithells Metals Reference Book*", Seventh Edition (Butterworth-Heinemann, Oxford, 1992) p. 13-83.
191. P. Doig and P.E.J. Flewitt, *Metall. Trans.* **18A** (1987) 399.
192. P.E.J. Flewitt, Private communication.
193. L.C. Lim and T. Watanabe, *Acta Metall.* **38** (1990) 2507.
194. C.J. McMahon and V. Vitek, *Acta Metall.* **27** (1979) 507.
195. L.S. Shvindlerman and R.G. Faulkner, To be published, 1995.

